

**Dynamics of Coherent and Incoherent
Excitations in Driven $\text{YBa}_2\text{Cu}_3\text{O}_{6.48}$**

Dissertation

Zur Erlangung des Doktorgrades an der Fakultät für Mathematik,
Informatik und Naturwissenschaften

Fachbereich Physik
der Universität Hamburg

Vorgelegt von
Ting-Han Chou

Hamburg

2024

Gutachter/innen der Dissertation:

Prof. Dr. Andrea Cavalleri

Prof. Dr. Henning Moritz

Zusammensetzung der Prüfungskommission:

Prof. Dr. Andrea Cavalleri

Prof. Dr. Henning Moritz

Prof. Dr. Michael A. Rübhausen

Prof. Dr. Tim Wehling

Prof. Dr. Ludwig Mathey

Vorsitzende/r der Prüfungskommission:

Prof. Dr. Ludwig Mathey

Datum der Disputation:

10.02.2025

Vorsitzender des Fach-Promotionsausschusses PHYSIK:

Prof. Dr. Wolfgang J. Parak

Leiter des Fachbereichs PHYSIK:

Prof. Dr. Markus Drescher

Dekan der Fakultät MIN:

Prof. Dr.-Ing. Norbert Ritter

Declaration on oath

I hereby declare and affirm that this doctoral dissertation is my own work and that I have not used any aids and sources other than those indicated.

If electronic resources based on generative artificial intelligence (gAI) were used in the course of writing this dissertation, I confirm that my own work was the main and value-adding contribution and that complete documentation of all resources used is available in accordance with good scientific practice. I am responsible for any erroneous or distorted content, incorrect references, violations of data protection and copyright law or plagiarism that may have been generated by the gAI.

04-11-2024

Date

Ting Han Chou

Signature of doctoral candidate

Abstract

Ultrashort optical pulses, particularly in the mid-infrared spectral range, have become powerful tools for the non-thermal control of electronic and magnetic phases in strongly correlated materials. A notable example is light-induced superconductivity in unconventional superconductors far above their equilibrium critical temperatures. In the bilayer cuprate $\text{YBa}_2\text{Cu}_3\text{O}_{6+x}$, the resonant excitation of apical oxygen phonons has been shown to induce superconducting-like optical properties even up to room temperature. Extensive studies aimed to identify the microscopic mechanisms behind this phenomenon, revealing that the coherently driven phonons transiently distort the crystal structure to favor the superconducting state. Additionally, these phonons couple nonlinearly to superfluid tunneling excitations between the stacked layers of this material, thereby enhancing superconductivity in $\text{YBa}_2\text{Cu}_3\text{O}_{6+x}$. However, the transient superconducting state is short-lived, persisting only for a few picoseconds, which limits its potential for future applications.

Upon the optical excitation, incoherent energy dissipation generates hot carriers, such as uncondensed quasiparticles and phonons, which ultimately raise the temperature of the system. The interaction between the coherent "cold" superfluid and the incoherent "hot" excitations is a key factor in determining the lifetime of the superconducting state. This thesis aims to characterize the temperature dynamics of quasiparticles and phonons in optically driven $\text{YBa}_2\text{Cu}_3\text{O}_{6+x}$. To achieve this goal, I developed a time-resolved spontaneous Raman scattering spectroscopy experiment to probe the increase in phonon temperatures following the mid-infrared optical excitation. By measuring the Stokes and anti-Stokes Raman scattering intensities of

a "spectator" phonon mode, a phonon temperature increase from 100 K to 240 K was observed. These numbers were compared with the transient temperatures of incoherent quasiparticles, estimated via time-domain terahertz spectroscopy. Remarkably, similar temperature dynamics were found for phonons and quasiparticles, suggesting that both play comparable roles in shortening the lifetime of the transient superconducting state. These findings provide quantitative insights into the nature of the optically driven state and may guide towards potential strategies for optimizing this phenomenon.

Zusammenfassung

Ultrakurze Lichtpulse, insbesondere im mittleren Infrarot-Spektralbereich, haben sich zu mächtigen Werkzeugen für die nicht-thermische Kontrolle von elektronischen und magnetischen Phasen in stark korrelierten Materialien entwickelt. Ein bemerkenswertes Beispiel ist die durch Licht induzierte Supraleitung in unkonventionellen Supraleitern weit über ihren kritischen Temperaturen im thermischen Gleichgewicht. In der Bi-Lagen Kupratverbindung $\text{YBa}_2\text{Cu}_3\text{O}_{6+x}$ zeigt die resonante Anregung von apikalen Sauerstoffphononen, dass supraleitungsähnliche optische Eigenschaften bis zur Raumtemperatur induziert werden können. Mehrere Studien haben versucht, die mikroskopischen Mechanismen hinter diesem Phänomen zu identifizieren, wobei gezeigt wurde, dass die kohärent getriebenen Phononen die Kristallstruktur transient verzerren, um den supraleitenden Zustand zu favorisieren. Darüber hinaus koppeln diese Phononen in einer nichtlinearen Wechselwirkung zu Anregung, die mit dem Tunneln von supraleitenden Cooper-Paaren zwischen den Lagen dieses Materials verbunden sind, wodurch die Supraleitung in $\text{YBa}_2\text{Cu}_3\text{O}_{6+x}$ verstärkt wird. Allerdings ist der transient supraleitende Zustand kurzlebig und besteht nur für einige Pikosekunden, was seine potenziellen Anwendungen begrenzt.

Bei der optischen Anregung generieren inkohärente Dissipationsprozesse heiße Ladungsträger, wie nicht-supraleitende Quasiteilchen, und Phononen, die letztendlich die Temperatur des Systems erhöhen. Die Wechselwirkung zwischen dem kohärenten "kalten" Suprafluid und den inkohärenten "heißen" Anregungen ist ein wichtiger Faktor bei der Bestimmung der Lebensdauer des supraleitenden Zustands. Diese Dissertation zielt darauf ab, die Temperaturdynamik von Quasiteilchen und Phononen

in optisch getriebenen $\text{YBa}_2\text{Cu}_3\text{O}_{6+x}$ zu charakterisieren. Um dieses Ziel zu erreichen, entwickelte ich ein Experiment für die zeitabhängige spontane Raman-Streuungsspektroskopie, um die Zunahme der Phonontemperaturen, die nach der mittleren Infrarot-optischen Anregung folgen, zu untersuchen. Durch Messung der Stokes- und Anti-Stokes-Raman-Streuungsinensitäten eines "Beobachter"-Phonons wurde eine Zunahme der Phonontemperatur von 100 K auf 240 K beobachtet. Dieses Ergebnis wurden mit dem Temperaturanstieg inkohärenter Quasiteilchen verglichen, der über zeitabhängige Terahertz-Spektroskopie Messungen abgeschätzt wurde. Erstaunlicherweise wurden ähnliche Temperaturdynamiken für Phononen und Quasiteilchen gefunden, was darauf hindeutet, dass beide eine vergleichbare Rolle in der Limitierung der Lebensdauer des transienten supraleitenden Zustands spielen. Diese Ergebnisse bieten quantitative Einblicke in die Natur des optisch getriebenen Zustands und weisen auf potenzielle Strategien für die Optimierung dieses Phänomens hin.

Contents

1	Introduction	7
2	Cuprate superconductors	11
2.1	Conventional superconductors	11
2.2	High- T_c cuprate superconductors	14
2.3	Equilibrium optical properties in $\text{YBa}_2\text{Cu}_3\text{O}_{6+x}$	17
3	Light-induced superconductivity in $\text{YBa}_2\text{Cu}_3\text{O}_{6+x}$	24
3.1	Reconstructing the transient optical properties	25
3.2	Light-induced optical properties above T_c	28
3.3	Pump frequency resonances	31
3.4	Two-fluid dynamics	34
4	Coherent couplings in optically-driven $\text{YBa}_2\text{Cu}_3\text{O}_{6.48}$	39
4.1	Coherent phonon-phonon coupling	40
4.1.1	Nonlinear phononics: cubic order coupling	40
4.1.2	Time-resolved reflectivity measurements	44
4.1.3	Transient lattice displacements in $\text{YBa}_2\text{Cu}_3\text{O}_{6.48}$	47
4.2	Coherent phonon-plasmon coupling	51
4.2.1	Modelling the phonon-plasmon coupling in $\text{YBa}_2\text{Cu}_3\text{O}_{6.48}$	51
4.2.2	Time-resolved second harmonic generation	53

4.2.3	Parametric amplification of Josephson plasmons	55
5	Incoherent couplings in optically-driven $\text{YBa}_2\text{Cu}_3\text{O}_{6.48}$	60
5.1	Dissipative response of hot quasiparticles	61
5.2	Spectator mode of hot incoherent phonons	63
5.3	Time-resolved Raman thermometry	66
5.3.1	Theory of Raman scattering	66
5.3.2	Experimental setup	71
5.4	Dynamics of hot incoherent phonons	74
5.4.1	Experimental results and data analysis	74
5.4.2	Extrapolated zero-fluence phonon temperatures	78
5.5	Comparison of phonons, quasiparticles, and superfluid responses . . .	84
6	Summary and outlook	88
7	Appendix	91

Chapter 1

Introduction

Strongly correlated materials are a class of materials that exhibit unusual electronic and magnetic properties, such as metal-insulator transitions, colossal magnetoresistance, and high-temperature superconductivity. In these materials, the interplay between various degrees of freedom, including charge, lattice, spin, and orbital, lead to a rich diversity of phases. Controlling the phases and properties of these materials has become an important research field in condensed matter physics due to the potential technological applications and the rich underlying physics.

The easiest method of controlling the phase of a material is by changing its temperature. When a material is heated beyond its critical temperature, it undergoes a phase transition from an ordered to a disordered state. For example, in ferromagnetic systems, heating above the Curie temperature disrupts the alignment of magnetic moments, causing a transition to a paramagnetic phase. In such transitions, the system generally experiences an increase in the symmetry.

Non-thermal methods for controlling the phases of materials involve tuning the electronic, magnetic, or structural properties without uniformly heating the entire system. This type of control can be achieved by tuning the chemical doping or applying static external stimuli such as pressure or magnetic fields. Recently, ultrashort laser pulses have become a powerful tool for the non-thermal control of

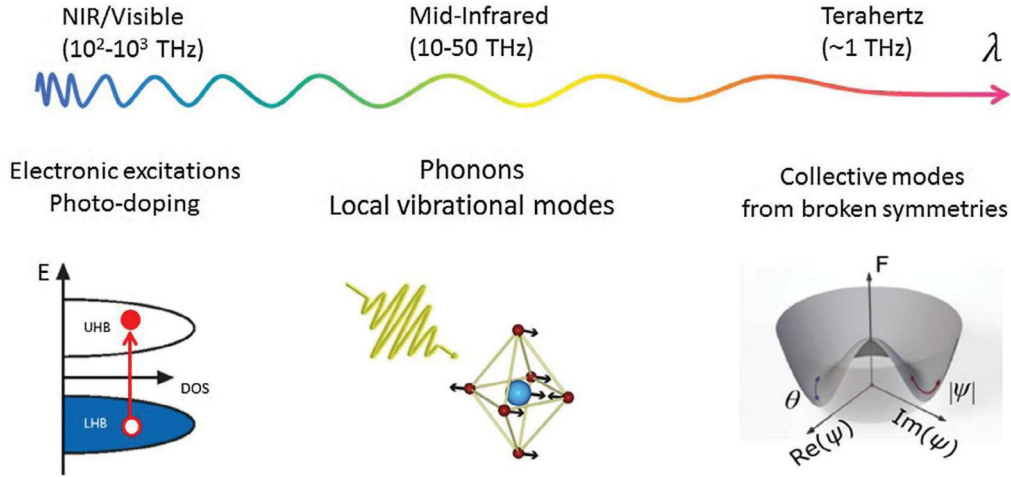


Figure 1.1: The electromagnetic spectrum of light with the corresponding fundamental excitations in solids. The electronic excitation occurs mainly in near-IR and visible frequency range, while the excitations of phonons and collective modes of broken symmetry are achieved at mid-IR and THz frequencies. (LHB = lower Hubbard band, UHB = upper Hubbard band.) This figure is reprinted from Ref. [1].

phase transitions. A key advantage of light is the possibility to generate ultrashort pulses down to the femtosecond range, which allows one to drive the material into a different phase or even a hidden phase that is not accessible in equilibrium on ultrafast timescales.

Another important benefit of controlling the electronic and magnetic phases of these complex materials with light is the ability to selectively excite different degrees of freedom. By tuning the light frequency, one can drive a specific mode and investigate how this driven mode couples with other excitations of the material, potentially to drive the phase transition. Figure 1.1 shows the electromagnetic spectrum of light, together with the corresponding fundamental excitations in solids. Excitations of electronic transitions, lattice vibrations, and collective modes of broken symmetry occur at frequencies in near-infrared/visible, mid-infrared (IR), and terahertz (THz) ranges, respectively.

Initially, near-IR and visible pulses have been widely used to manipulate the phases of complex materials. Light at these frequencies typically has high absorption in materials due to the excitation of electronic transitions. In some cases, this results in significant heating of the entire system, causing phase transitions primarily driven

by thermal effects. Additionally, such carrier absorption readily induces phenomena like demagnetization or collapse of charge-ordered states [2–7]. These processes lead to an increase in the symmetry of the system, similar to conventional thermal control.

In contrast, manipulating the phase transitions using mid-IR pulses offers a distinct advantage of reduced heating. These light fields resonantly drive lattice vibrations, or phonons, with minimal energy deposition, i.e. less heating, into the system. These coherently driven phonons oscillate at large amplitude and couple nonlinearly to other vibrational modes, leading to a transient change in crystal structure that breaks the crystal symmetry [8–10]. Potentially, the non-equilibrium lattice structure drives a transition to an ordered phase. Moreover, the coherently driven phonons can couple to other lower-energy collective modes associated with broken symmetries, such as magnetic and superconducting fluctuations. Recent examples of such non-thermal phase control are para-to-ferroelectric transitions, stabilization of ferromagnetism, and light-induced superconductivity [11–14].

Interestingly, in these examples, the materials are driven from high-temperature disordered phases into ordered phases that can only be achieved at low temperature in equilibrium. Hence, these phenomena can be described as an effective “phase cooling” induced by a coherent phonon drive, which temporarily stabilizes the ordered states such as superconductivity or ferromagnetism. Meanwhile, despite the lower heating effect of mid-IR excitation, the incoherent energy dissipation still gives rise to an overall temperature rise in the material. This incoherent heating generally works against the formation of the ordered state as it tends to increase the symmetry and favor the disordered state. Therefore, one can expect a competition between the coherent cooling, which promotes the ordered state, and incoherent heating, which disrupts it.

In this thesis, I focus on light-induced superconductivity in the high-temperature superconductor $\text{YBa}_2\text{Cu}_3\text{O}_{6+x}$ [15–26]. Recent work has shown that coherent excitation of the apical oxygen phonons drives this material into a state with superconducting-

like optical properties at temperatures far above the equilibrium critical temperature, even at room temperature. The lifetime of the coherent superconducting state persists only for a few picoseconds, potentially limited by heating of incoherent carriers such as quasiparticles and phonons. The temperature dynamics of incoherent quasiparticles and phonons will be carefully studied here, with emphasis on the heating of incoherent phonons, which has never been studied before. The gained insight can help to understand energy transfer processes in optically driven $\text{YBa}_2\text{Cu}_3\text{O}_{6+x}$ and how incoherent carriers affect the coherent superconducting state.

The thesis is structured as follows: Chapter 2 introduces the history of superconductivity from conventional superconductors to high-temperature superconductors, as well as equilibrium optical properties in $\text{YBa}_2\text{Cu}_3\text{O}_{6+x}$. Chapter 3 shows that resonant phonon driving leads to superconducting-like optical properties in time-resolved THz spectroscopy measurements. Properties of light-induced superconductivity including temperature dependence, doping dependence, pump frequency resonance, and decoherence time will be summarized. Chapter 4 introduces coherent couplings in optically driven $\text{YBa}_2\text{Cu}_3\text{O}_{6+x}$. Cubic phononic couplings between the driven phonons and Raman phonons result in a new crystal structure that favor the superconductivity. Furthermore, the driven phonons directly couple to inter-layer supercurrent via three-mode mixing process, enhancing the superconductivity. Chapter 5 investigates the incoherent dynamics in optically driven $\text{YBa}_2\text{Cu}_3\text{O}_{6+x}$. The temperatures of hot quasiparticles are determined from the time-resolved THz spectroscopy, while the temperatures of hot phonons are obtained by time-resolved Raman thermometry. Basic theory of Raman scattering, experiment setup, data analysis, results, and discussion will be summarized. Chapter 6 shows conclusion of this thesis and possible future outlook.

Chapter 2

Cuprate superconductors

In this chapter, I will provide foundational knowledge about the material studied in this thesis, the high-temperature superconductor $\text{YBa}_2\text{Cu}_3\text{O}_{6+x}$. In the first section, a brief introduction of conventional superconductors, the BCS theory, and order parameter will be given. Next, I will focus on high temperature cuprate superconductors, discussing their crystal structure and phase diagram. Finally, I will describe the equilibrium optical properties of $\text{YBa}_2\text{Cu}_3\text{O}_{6+x}$. The two-fluid model and Josephson effect will be used to identify the signatures of superconductivity.

2.1 Conventional superconductors

Superconductivity is a phenomenon observed in certain materials when they are cooled to very low temperatures. At these temperatures, the materials exhibit two distinctive physical properties: 1) the electrical resistivity drops to zero, resulting in dissipationless electrical transport, and 2) the material completely expels static magnetic fields, also known as the Meissner effect (see Fig. 2.1). This phenomenon was first discovered in mercury at liquid helium temperature of about 4 Kelvin by Heike Kamerlingh Onnes in 1911. Since then, numerous materials have been found to exhibit superconductivity upon cooling below a critical temperature, denoted as T_c . Still today, research continues to push the boundary of T_c , aiming for the

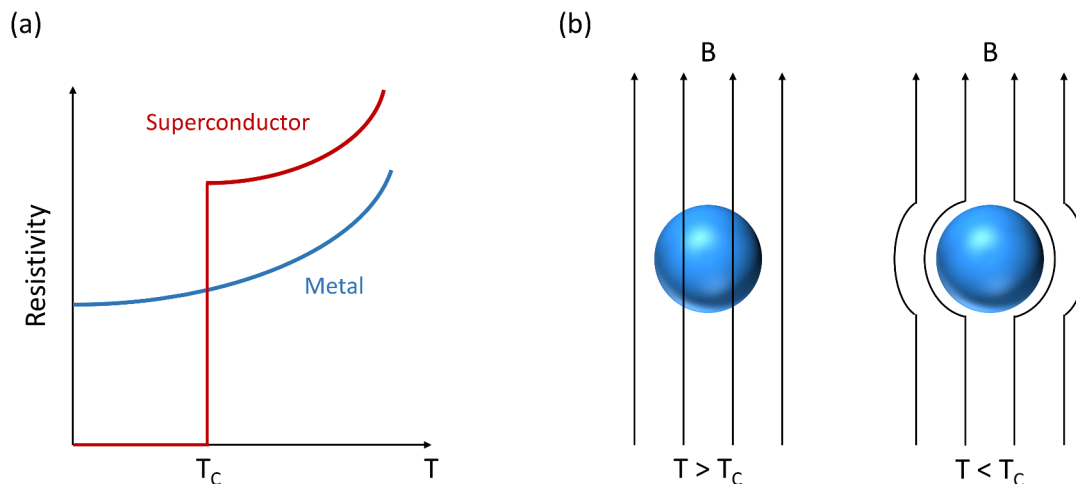


Figure 2.1: (a) The electric resistivity as a function of temperature for a superconductor (red) and a metal (blue). (b) Schematic of the expulsion of a static magnetic field B , known as Meissner effect.

achievement of a room temperature superconductor.

BCS theory

Conventional superconductors are the materials that exhibit superconductivity, a phenomenon described by the Bardeen-Cooper-Schrieffer (BCS) theory, proposed in 1957 [27]. According to BCS theory, as a metal is cooled down, thermal fluctuations of the crystal lattice are suppressed and the periodic atomic arrangement becomes more stationary. When an electron moves through this stationary lattice, it distorts the surrounding ions and creates a region of higher positive charge. This positively-charged region attracts another electron, leading to the formation of an electron pair known as a Cooper pair (see Fig. 2.2), which behaves like a boson rather than a single-electron fermion. The superconductivity is a macroscopic effect resulting from condensation of the Cooper pairs.

When Cooper pairs condense, an energy gap, conventionally labeled as 2Δ , opens near the Fermi surface. The magnitude of this gap is determined by the phonon-mediated binding energy of the Cooper pairs. At the temperature below T_c , the thermal energy of the lattice is smaller than the energy gap. Thus, the Cooper

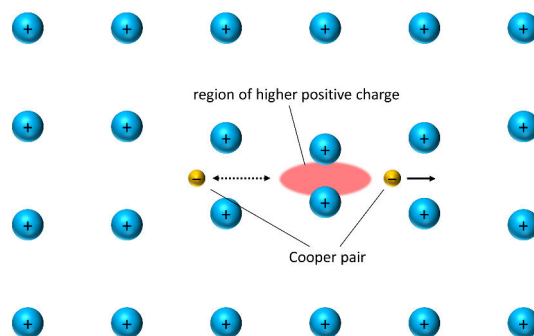


Figure 2.2: Schematic of the formation of a Cooper pair via phonon-mediated interaction.

pairs can move through the lattice without any scattering. As the temperature increases above T_c , the thermal energy of the lattice becomes large enough to break the Cooper pairs and destroy the superconducting order. The BCS theory predicts the relations among the superconducting gap 2Δ , the critical temperature T_c , and the electron-phonon coupling strength λ [27]:

$$2\Delta \approx 3.5k_B T_c \quad (2.1)$$

$$k_B T_c \approx 1.13\hbar\omega_0 e^{-\frac{1}{\lambda}} \quad (2.2)$$

where k_B is the Boltzmann constant and ω_0 is the phonon frequency. In experiments, the isotope effect on the critical temperature supports that the phonon interaction involves the pairing mechanism. A heavier isotopic mass (M) gives a lower phonon frequency and, according to Eq. (2.2), leads to a lower T_c . This relation can be expressed as $T_c \propto M^{-\alpha}$ with α equals to 0.5. However, these phonon-mediated superconductors generally have a low T_c . The highest recorded T_c for a phonon-mediated superconductor is 39 K found in MgB_2 [28].

Order parameter

The concept of order parameter in superconductivity was introduced by Ginzburg and Landau in 1950 to describe the superconducting phase transition phenomenologically. The order parameter represents the macroscopic quantum wavefunction of the superconducting state and can be written as a complex number $\Psi(r) = |\Psi(r)|e^{i\theta(r)}$.

The magnitude of order parameter $|\Psi(r)|^2$ corresponds to the density of Cooper pairs in the material. Below T_c , the magnitude of order parameter becomes non-zero, indicating the presence of Cooper pairs in superconducting state. Above T_c , the material returns to the normal state and the order parameter drops to zero. The phase of the order parameter $\theta(r)$ represents the quantum mechanical phase of Cooper pairs. The spatial variation of the phase is related to the supercurrent flow within the superconductor.

Additionally, the order parameter is connected to the superconducting energy gap. In conventional BCS superconductors, the order parameter exhibits s-wave symmetry, meaning the gap is isotropic. In contrast, for the unconventional superconductor such as high- T_c cuprates, the order parameter can show more complicated symmetries such as d-wave. The gap varies depending on the momentum directions.

2.2 High- T_c cuprate superconductors

Unconventional superconductors are materials that exhibit anomalously high T_c and cannot be described by the BCS theory. In these superconductors, Cooper pairs are not bound by phonon exchange but by other, still debated pairing mechanisms. In 1986, Bednorz and Müller discovered superconductivity in the ceramic compound $\text{La}_{2-x}\text{Ba}_x\text{CuO}_4$ with a T_c of 35 K [29], marking the first observation of a material with a T_c exceeding 30 K. Shortly after, similar compounds such as $\text{YBa}_2\text{Cu}_3\text{O}_{6+x}$ and $\text{Bi}_2\text{Sr}_2\text{CaCu}_2\text{O}_{8+x}$ were discovered, exhibiting even higher values of T_c up to nearly 100 K [30]. These copper oxide compounds, known as cuprates, opened a new path for high T_c superconductors. To date, the highest T_c under the ambient pressure is achieved in $\text{HgBa}_2\text{Ca}_2\text{Cu}_3\text{O}_{8+x}$, which reaches a T_c up to 133 K [31].

All the cuprate superconductors have a similar crystal structure, in which quasi two-dimensional CuO_2 layers, separated by insulating charge reservoir layers, are stacked along the crystal c-axis. The CuO_2 layers determine the electric and magnetic properties of cuprate materials. Different types of cuprates can have one or

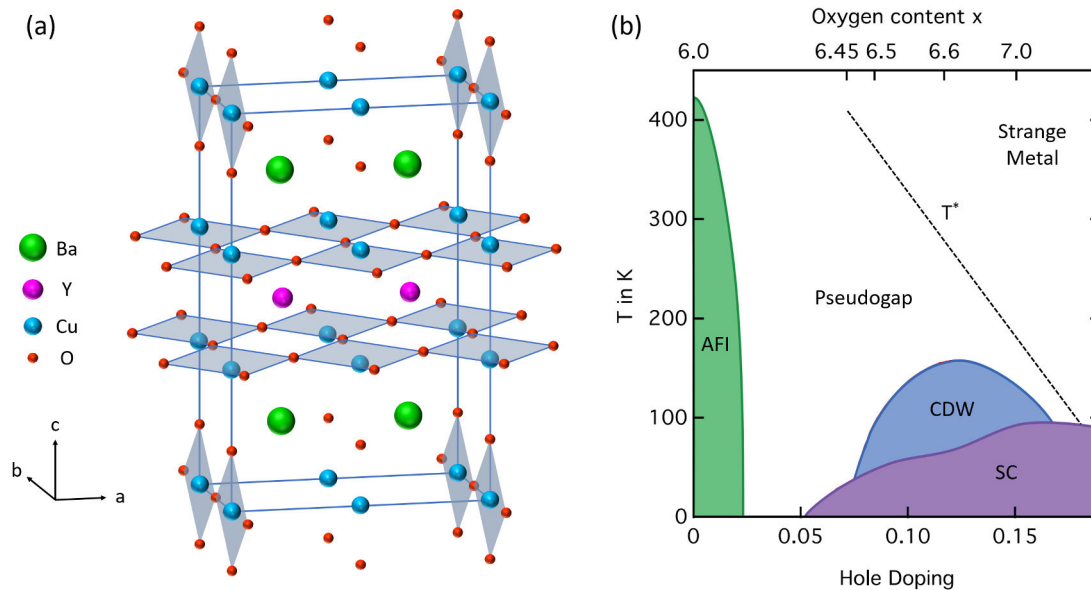


Figure 2.3: (a) Crystal structure of orthorhombic $\text{YBa}_2\text{Cu}_3\text{O}_{6.5}$ (b) Phase diagram of $\text{YBa}_2\text{Cu}_3\text{O}_{6+x}$. AFI, CDW, and SC refer to the antiferromagnetic insulating, charge-density-wave, and superconducting phase, respectively. Part of this figure is adapted from Ref. [32]

more CuO_2 layers in the unit cell of the crystal lattice. Figure 2.3a illustrates the crystal structure of a bilayer cuprate, $\text{YBa}_2\text{Cu}_3\text{O}_{6+x}$. The unit cell consists of two CuO_2 layers that form a bilayer by sandwiching a thin insulating layer composed of Y atoms. These bilayers are further separated by a thicker insulating layer made up of Ba atoms and Cu-O chains. By doping a certain amount of oxygen atoms into the thick insulating layers, one can increase the hole doping in the CuO_2 layer and control the electronic and magnetic properties of $\text{YBa}_2\text{Cu}_3\text{O}_{6+x}$. The corresponding phase diagram is depicted in Fig. 2.3b. In this thesis, we mainly study the sample with oxygen content 6.48. The superconducting transition temperature T_c is around 50 K.

Antiferromagnetic insulator

The undoped parent compound $\text{YBa}_2\text{Cu}_3\text{O}_6$ is an insulator with a long-range antiferromagnetic order. In the CuO_2 planes, the copper ions Cu^{2+} have a $3d^9$ configuration. The highest energy orbitals $3d_{x^2-y^2}$ are half-filled and oriented towards

the $2p_{x,y}$ orbitals of the four adjacent oxygen ions O^{2-} . Although the band theory predicts the half-filled orbitals to result in metallic behavior, the strong Coulomb interactions localize the electrons and prevent the hopping between the Cu sites. The hybridization of Cu $3d_{x^2-y^2}$ and O $2p_{x,y}$ orbitals causes the $YBa_2Cu_3O_6$ to be a charge transfer insulator with the energy gap of around 2 eV (the energy required to excite an electron from $3d^9, 2p^6$ to $3d^{10}, 2p^5$). The superexchange interaction between these localized electrons results in an antiparallel alignment of neighboring spins. As shown in Fig. 2.3b, such antiferromagnetic order exists all the way up to 400 K and can be disrupted by 2% hole doping, which makes the system become metallic.

Superconductivity

The superconducting phase emerges at the sufficiently low temperatures and hole doping levels above 5%. The highest superconducting transition temperature T_c is almost 100 K for the compound with an oxygen content of 6.9. The electrons with the energies close to Fermi level condense into Cooper pairs and form long range phase coherence. Although the Cooper pairs are confined to the CuO_2 planes, the phase difference of order parameters leads to a tunneling current flowing across the insulating layers along the c -axis to another CuO_2 planes. This phenomenon is known as the Josephson effect. The tunneling supercurrent leads to oscillations, generating what are called Josephson plasma waves. These plasma oscillations occur at natural frequencies in the THz range.

Charge density wave

A charge density wave (CDW) is a periodic modulation of the conduction electron density. Recently, several x-ray scattering experiments have observed CDW order in the $YBa_2Cu_3O_{6+x}$ phase diagram [33,34]. The CDW phase locates on top of the superconducting dome in a broad range around a hole doping of around $1/8^{\text{th}}$ (0.125%).

The superconducting dome is slightly suppressed at these doping levels, suggesting that CDW and superconductivity are competing orders in this compound. This has been corroborated by further studies, where by applying an external magnetic field below T_c , the superconductivity is destroyed and the CDW order enhanced [35, 36].

Pseudogap

The pseudogap phase is observed in the underdoped region at the temperature above T_c and up to a temperature that is often denoted as T^* . This phase is characterized by anomalous electronic properties, where a partial gap opens in the electron density of states near the Fermi level. Recent research has found that the symmetry of the pseudogap is very similar to that of the superconducting gap. This may suggest that in the pseudogap phase, the Cooper pairs are already formed but only exhibit short-range coherence [37–40]. Phase fluctuations prevent the material from becoming a superconductor. The relation between the pseudogap and superconductivity is still under debate.

Strange metal

The strange metal phase occurs in the higher-doping region, to the right side of the pseudogap in the phase diagram. This phase is characterized by its unconventional transport properties, which cannot be explained by Fermi liquid theory. For example, the electric resistivity is anomalously high and scales linearly with temperature, deviating from Fermi-liquid behavior [41, 42]. As the hole doping increases further, the compound eventually transforms into a normal metal phase.

2.3 Equilibrium optical properties in $\text{YBa}_2\text{Cu}_3\text{O}_{6+x}$

In this thesis, we aim to investigate the superconducting phase transition in $\text{YBa}_2\text{Cu}_3\text{O}_{6+x}$ induced by ultrashort optical pulses. On such short timescales (a few picoseconds),

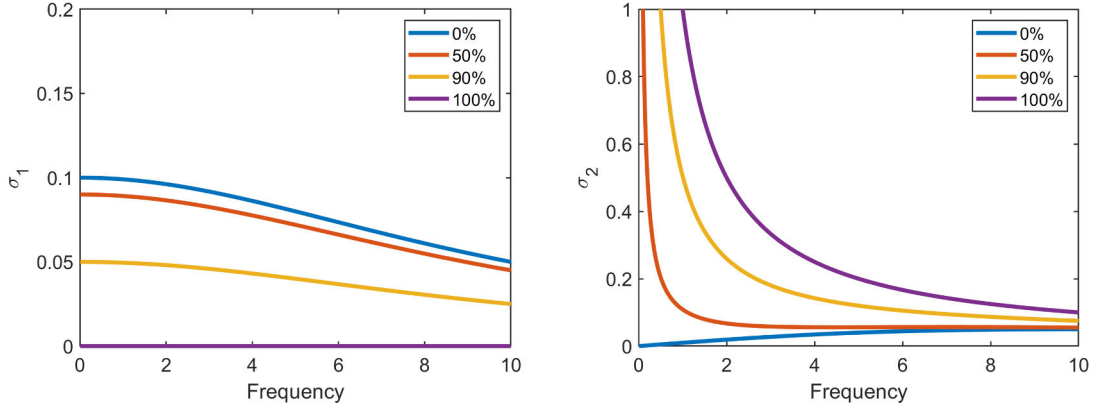


Figure 2.4: The real part and imaginary part of optical conductivity calculated from the two-fluid model. The labeled percentage is the ratio of the superfluid density to the total density, hence blue lines correspond to a metal and purple lines to a superconductor.

it becomes challenging to directly measure conventional superconducting properties like zero electrical resistance or the Meissner effect. As an alternative, we utilize time-resolved THz spectroscopy, which allows us to probe the optical properties in the THz frequency range. The key advantage of THz spectroscopy is that a single-cycle THz pulse has a duration of approximately 1 ps, making it ideal for studying ultrafast dynamics. Additionally, THz frequencies correspond to the energy scales of Cooper pairs and quasiparticles, providing direct sensitivity to the superconducting transition. In this Section, I will derive the optical properties of a superconductor and introduce the equilibrium optical properties in $\text{YBa}_2\text{Cu}_3\text{O}_{6+x}$.

Two-fluid model

For a superconductor at a finite temperature below the transition temperature $0 < T < T_c$, some electrons are bound together and condense into Cooper pairs, while the rest of electrons remain uncondensed and behave as "normal" electrons. In other words, the dissipationless superconducting carriers (superfluid) coexist with the uncondensed quasiparticles (normal fluid). The optical properties of such a system (in the frequency range below superconducting gap 2Δ) can usually be described by "two-fluid model".

We begin with the Drude model to derive the optical conductivity in a normal

metal. When an oscillating electric field is applied to a metal, the drift velocity v of electrons can be derived by Newton's law

$$F = m^* \frac{dv}{dt} = eE - \gamma m^* v \quad (2.3)$$

where m^* is the effective mass, γ is the scattering rate, and $E = E_0 e^{i\omega t}$ is the applied electric field with the oscillating frequency ω . Solving Eq. (2.3) through Fourier analysis, we get

$$v(\omega) = \frac{e}{m^*} \frac{E}{\gamma - i\omega} \quad (2.4)$$

Considering that the metal has an electron density n , the current density J is then given by

$$J = nev = \sigma E \quad (2.5)$$

By substituting Eq. (2.4) into Eq. (2.5), the complex optical conductivity σ can be expressed as

$$\sigma(\omega) = \frac{ne^2}{m^*} \frac{1}{\gamma - i\omega} \quad (2.6)$$

Here, we label the real and imaginary part of the optical conductivity as $\sigma_1(\omega)$ and $\sigma_2(\omega)$, respectively. This Drude response appears as a peak at zero frequency with the bandwidth given by γ in the $\sigma_1(\omega)$ spectrum, and a broad peak at the frequency γ in the $\sigma_2(\omega)$ spectrum. If we consider an overdamped Drude response ($\gamma \gg \omega$), both the $\sigma_1(\omega)$ and $\sigma_2(\omega)$ exhibit a featureless spectrum. Next, we derive the Drude response of the superconducting carriers by taking a limit of a vanishing scattering rate $\gamma \rightarrow 0$. Now, Eq. (2.6) becomes

$$\sigma(\omega) = \frac{ne^2}{m^*} \left(\frac{\pi}{2} \delta(\omega = 0) + \frac{i}{\omega} \right) \quad (2.7)$$

All the spectral weights in $\sigma_1(\omega)$ vanish and condense into a δ peak at zero frequency, while $\sigma_2(\omega)$ presents a $1/\omega$ divergence. The δ peak at zero frequency in $\sigma_1(\omega)$ reflects that the system has infinity conductivity (zero resistance) to a DC field. For other low-frequency fields, $\sigma_1(\omega)$ becomes zero as their energy are too low to break Cooper pairs and thus cannot produce dissipative responses. The $1/\omega$ divergence

in $\sigma_2(\omega)$ can be understood from Kramers-Kronig relation, which connects the real and imaginary parts of conductivity. Whenever there is a δ peak in $\sigma_1(\omega)$, there must be a corresponding divergence in $\sigma_2(\omega)$.

The two-fluid model combines the two contributions given by Eq. (2.6) and Eq. (2.7). We define the densities of normal fluid and superfluid as n_n and n_s , respectively. The total optical conductivity is

$$\sigma(\omega) = \frac{n_s e^2}{m^*} \left(\frac{\pi}{2} \delta(\omega = 0) + \frac{i}{\omega} \right) + \frac{n_n e^2}{m^*} \frac{1}{\gamma - i\omega} \quad (2.8)$$

For an equilibrium superconductor, $n_n + n_s$ should remain constant. The only variable parameter is the percentage of superfluid to total fluid $\frac{n_s}{n_s + n_n}$. Figure 2.4 shows the calculated $\sigma_1(\omega)$ and $\sigma_2(\omega)$ using Eq. (2.8) with $\frac{n_s e^2}{m^*} + \frac{n_n e^2}{m^*} = 1$ and $\gamma = 10$. The percentage of superfluid to total fluid $\frac{n_s}{n_s + n_n}$ is set at 100%, 90%, 50%, and 0%. In the real part of the optical conductivity $\sigma_1(\omega)$, the superfluid only contributes a δ peak at zero frequency, which is not detectable in THz spectroscopy experiments because the THz frequencies are too high to observe the DC response. Therefore, the normal fluid density can be determined by the amplitude of spectral components at other non-zero frequencies. On the other hand, the superfluid density can be extracted by fitting the proportionality constant of $1/\omega$ dependence in the imaginary part of the optical conductivity $\sigma_2(\omega)$. In summary, when cooling a metal to a superconductor, we will observe a reduction in $\sigma_1(\omega)$ spectral weight and a $1/\omega$ divergence in $\sigma_2(\omega)$.

THz-frequency c-axis optical properties

Doped $\text{YBa}_2\text{Cu}_3\text{O}_{6+x}$ exhibits significant anisotropy in its electric and optical properties depending on the direction. Along the ab-plane, $\text{YBa}_2\text{Cu}_3\text{O}_{6+x}$ is metallic and electrons can move relatively freely within the CuO_2 planes, leading to a high in-plane conductivity. However, along the c-axis, $\text{YBa}_2\text{Cu}_3\text{O}_{6+x}$ behaves more like a poor metal or a semiconductor. The electron hopping between CuO_2 planes is limited by insulating charge reservoir layers, resulting in a much lower conductivity

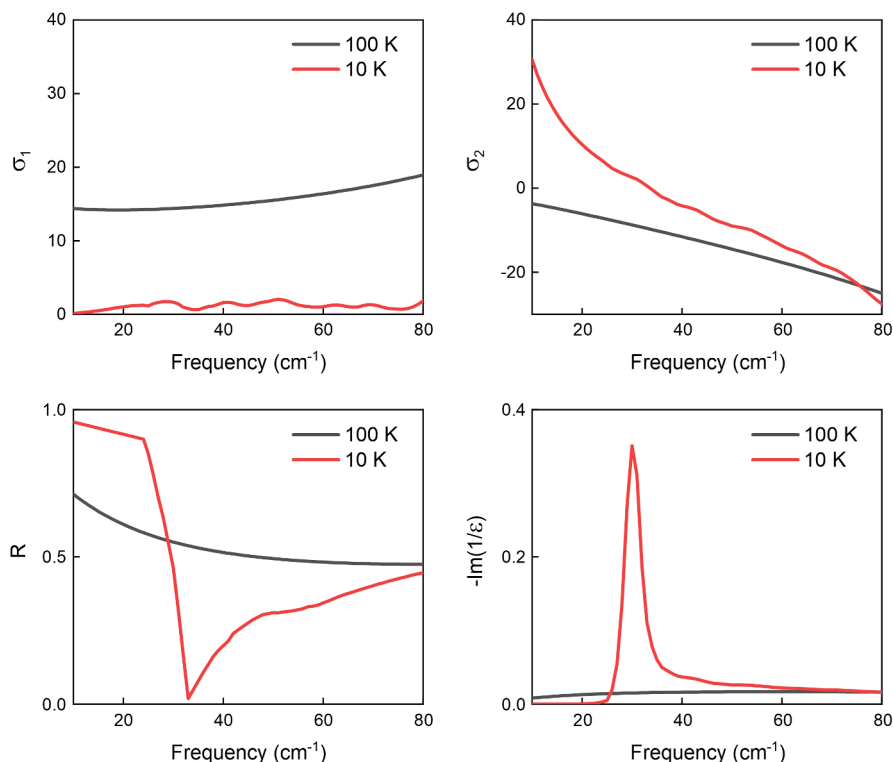


Figure 2.5: The *c*-axis THz-frequency optical properties in the equilibrium superconducting (10 K, red) and normal (100 K, gray) state of $\text{YBa}_2\text{Cu}_3\text{O}_{6.5}$. (a, b) The real and imaginary parts of optical conductivity $\sigma_1(\omega)$ and $\sigma_2(\omega)$, (c) the reflectivity $R(\omega)$, and (d) the energy loss function $-\text{Im}(1/\epsilon(\omega))$.

compared to the *ab*-plane.

Here, we utilized the *c*-axis THz optical conductivity to investigate the superconducting transition in $\text{YBa}_2\text{Cu}_3\text{O}_{6.5}$. One advantage of probing along the *c*-axis is the significantly higher scattering rate of the normal fluid compared to the *ab*-plane. In the two-fluid model, as discussed earlier, the normal fluid is assumed to be highly damped. In the frequency range below the scattering rate, the optical conductivity is nearly constant and frequency-independent. This behavior makes it easier to distinguish between the featureless normal fluid and the $1/\omega$ divergent superfluid responses.

Another benefit of probing along the *c*-axis is the distinct feature in THz optical properties associated with the Josephson effect. When an external light field, particularly in the THz range, interacts with the $\text{YBa}_2\text{Cu}_3\text{O}_{6.5}$, it couples with the interlayer supercurrent (Josephson plasma) to form a quasiparticle called the Joseph-

son plasma polaritons (JPP). This coupling is a hallmark of superconductivity in cuprates. The JPP can be observed as a plasma edge in the reflectivity spectrum and a peak in the energy loss function.

Figure 2.5 shows the equilibrium c-axis optical properties in $\text{YBa}_2\text{Cu}_3\text{O}_{6.5}$ at superconducting state 10 K and normal state 100 K. In the normal state ($T > T_c$), the real part of the optical conductivity $\sigma_1(\omega)$ exhibits a featureless spectrum at a finite value, which descends from the Drude response of quasiparticles at frequencies below the scattering rate ($\omega \ll \gamma$). The amplitude of $\sigma_1(\omega)$ reflects the population of thermally activated quasiparticles. Upon cooling into the superconducting state ($T < T_c$), the $\sigma_1(\omega)$ spectral weight is reduced, and a divergent $1/\omega$ response in the $\sigma_2(\omega)$ appears, indicating the onset of dissipationless transport.

In addition to the optical conductivity, in the superconducting state, $\text{YBa}_2\text{Cu}_3\text{O}_{6.5}$ displays distinct signatures of JPP, including a sharp edge in the reflectivity spectrum $R(\omega)$ and a peak in the energy loss function $-\text{Im}(1/\epsilon(\omega))$ at the frequency of 30 cm^{-1} . This frequency corresponds to the natural frequency of inter-bilayer JPP mode at the zero momentum.

In the bilayer cuprate $\text{YBa}_2\text{Cu}_3\text{O}_{6.5}$, two longitudinal Josephson plasma polariton (JPP) modes can be identified. As shown in Fig. 2.6a, at zero momentum, the lower-frequency mode arises primarily from supercurrent flow within the bilayers, while the higher-frequency mode is associated with supercurrent tunneling between bilayers. In Fig. 2.6b, the plasma edges in the reflectivity spectrum $R(\omega)$ and the corresponding peaks in the energy loss function $-\text{Im}(1/\epsilon(\omega))$ are observed at 30 and 475 cm^{-1} , representing the natural frequencies of the interbilayer and intrabilayer JPP modes at zero momentum. At finite momentum, these JPP modes involve supercurrent flow not only along the c-axis but also within the ab-plane. The dispersion of these JPP modes can be determined by the inductive responses of the CuO_2 planes (more details will be shown in Section 4.2).

So far, I have examined the equilibrium optical properties of $\text{YBa}_2\text{Cu}_3\text{O}_{6.5}$, focusing on its distinct THz signatures. These features will serve as key indicators in

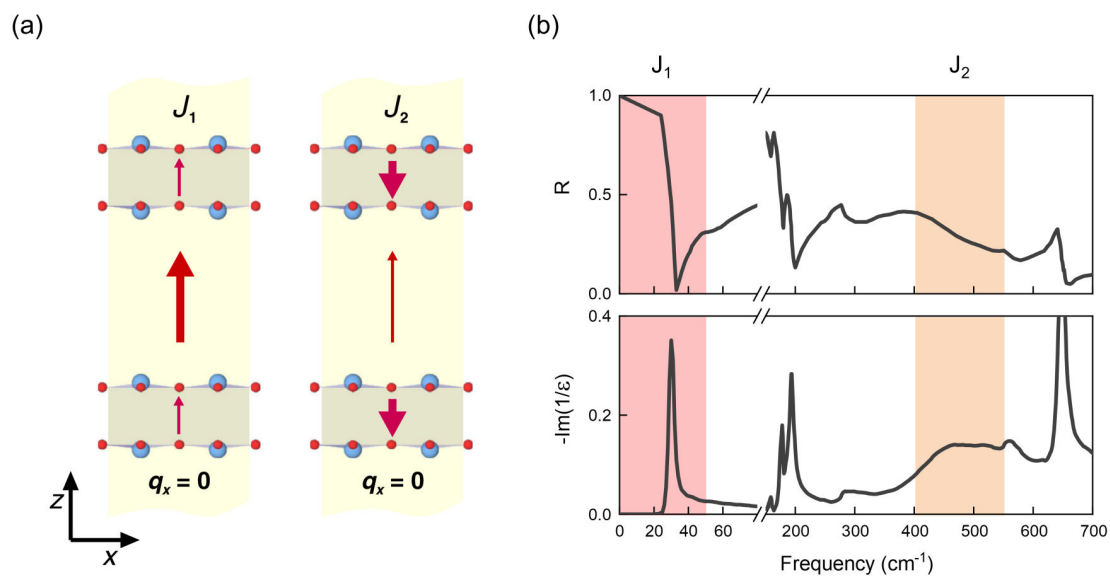


Figure 2.6: (a) The structure of YBa₂Cu₃O_{6.5} can be viewed as two Josephson junctions in series, which gives rise to two longitudinal JPP modes (J_1 , J_2). Arrows indicate the direction of the supercurrent. (b) Equilibrium c-axis optical properties. The two longitudinal JPP modes appear as two peaks at 30 and 475 cm⁻¹ in the energy loss function and two edges in the reflectivity. Part of this figure is reprinted from the Ref. [22].

the following chapters to explore whether the material undergoes a superconducting phase transition when exposed to optical excitation.

Chapter 3

Light-induced superconductivity in $\text{YBa}_2\text{Cu}_3\text{O}_{6+x}$

Light-induced superconductivity in $\text{YBa}_2\text{Cu}_3\text{O}_{6+x}$ refers to the phenomenon where the material exhibits superconducting-like optical properties at temperatures well above its critical temperature T_c when driven by intense optical pulses. This concept was inspired by earlier high-pressure studies [43–45], which found that the position of the apical oxygen atom—located above or below the CuO_2 planes—strongly influences the T_c in $\text{YBa}_2\text{Cu}_3\text{O}_{6+x}$. Building on these insights, recent researches employed mid-IR optical pulses to resonantly drive the apical oxygen phonon modes into the nonlinear regime, resulting in superconducting-like features in the THz-frequency optical conductivity along the c-axis [15–17, 21, 23]. These findings suggest the possibility of inducing a superconducting response all the way up to room temperature.

In this chapter, I will report a series of time-resolved THz spectroscopy experiments, where these features have been observed. The properties of light-induced superconductivity in $\text{YBa}_2\text{Cu}_3\text{O}_{6+x}$ including doping-dependence, temperature-dependence, pump frequency resonance, and decoherence time will be introduced.

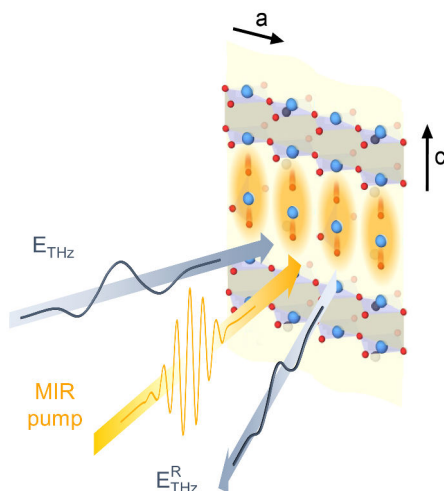


Figure 3.1: (a) Schematic of time-resolved THz spectroscopy. The mid-IR pump pulse (yellow) resonantly drives c -axis apical oxygen infrared phonons in $\text{YBa}_2\text{Cu}_3\text{O}_{6+x}$. Single-cycle THz probe pulses (slate gray) were reflected from the sample and detected by phase-sensitive electro-optic sampling.

3.1 Reconstructing the transient optical properties

In this Section, I will introduce the experimental method and the reconstruction model used to characterize the transient optical properties of $\text{YBa}_2\text{Cu}_3\text{O}_{6+x}$ induced by mid-IR excitation. Time-resolved THz spectroscopy is employed to probe both the amplitude and phase of the THz radiation from the sample, as illustrated in Fig. 3.1. The excitation pulses were tuned to resonantly drive two apical oxygen infrared phonon modes with natural frequencies of 17 and 20 THz. Single-cycle THz probe pulses, with spectral components ranging from 10 cm^{-1} to 80 cm^{-1} , were shone onto the sample. The reflected THz probe pulses were then detected using phase-sensitive electro-optic sampling.

However, the measured THz spectra cannot fully represent the transient optical properties of $\text{YBa}_2\text{Cu}_3\text{O}_{6+x}$ due to the mismatch in penetration depths between the pump and probe pulses. The THz probe pulse penetrates deeper into the sample than the mid-IR pump pulse, leading to a discrepancy between the detected volume and excited volume. To account for this, a reconstruction model is necessary to ac-

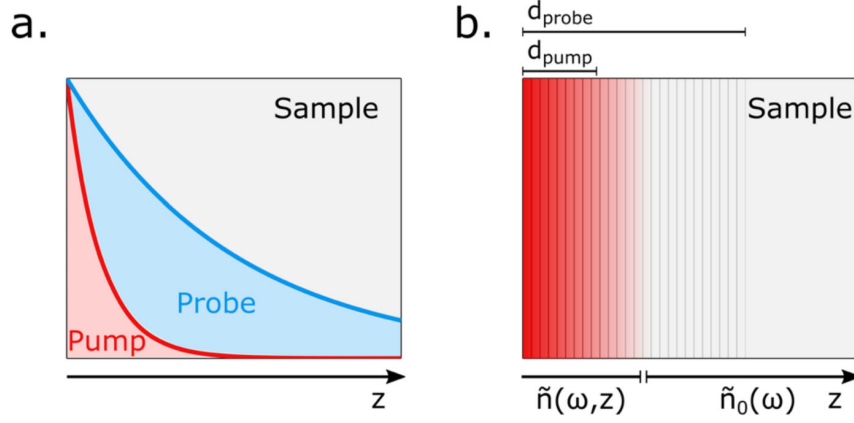


Figure 3.2: (a) Schematics of pump-probe penetration depth mismatch. (b) Multi-layer model with exponential decay used to calculate the pump-induced changes in the complex refractive index $\tilde{n}(\omega, \tau)$ for each pump-probe delay τ . The transition from red to background (gray) represents the decaying pump-induced changes in $\tilde{n}(\omega, z)$. This figure is reprinted from Ref. [46]

curately retrieve the transient optical properties from the THz probe measurements. The detailed procedure of this reconstruction process is shown as follows.

In the time-resolved THz reflectivity experiments, we can measure the THz electric field reflected from the equilibrium sample \tilde{E}_R and the change in reflected THz electric field induced by the pump excitation $\Delta\tilde{E}_R$. The change in complex reflection coefficient $\Delta\tilde{r}$ can be extracted by the following equation

$$\frac{\Delta\tilde{E}_R}{\tilde{E}_R} = \frac{\Delta\tilde{r}}{\tilde{r}_0} \quad (3.1)$$

where \tilde{r}_0 is the equilibrium complex reflection coefficient. In $\text{YBa}_2\text{Cu}_3\text{O}_{6+x}$, the penetration depth of mid-IR pump pulse ($0.7 \mu\text{m}$) is significantly smaller than that of the THz probe pulse ($5\text{--}10 \mu\text{m}$). The penetration depth is defined as

$$d(\omega) = \frac{c}{2\omega} \frac{1}{\text{Im}[\tilde{n}_0(\omega)]} \quad (3.2)$$

where $\tilde{n}_0(\omega)$ is the equilibrium complex refractive index in the bulk. Due to the penetration depth mismatch, the pump effect in the probe volume is inhomogeneous. This needs to be considered in order to extract the transient optical properties at the sample surface.

Figure 3.2 illustrates the schematics of penetration depth mismatch and the multi-layer model. The sample is modeled as a stack of thin layers. For the layers close to the surface (within the pump volume), the non-equilibrium refractive index is $\tilde{n}(\omega, z) = \tilde{n}_0(\omega) + \Delta\tilde{n}(\omega, z)$, while for the other unperturbed layers, the refractive index is the same as in the bulk $\tilde{n}_0(\omega)$. The reflection coefficient change of this multi-layer system can be written as a function of the refractive index change $\Delta\tilde{r}[\Delta\tilde{n}(\omega, z)]$.

Here, our aim is to reconstruct the refractive index change at the sample surface $\Delta\tilde{n}(\omega, z = 0)$, where the pump effect is the strongest. To this end, we need to assume a relation between the $\Delta\tilde{n}(\omega, z)$ and the $\Delta\tilde{n}(\omega, z = 0)$. Once this relation is formed, the reflection coefficient change $\Delta\tilde{r}[\Delta\tilde{n}(\omega, z)]$ can be written as $\Delta\tilde{r}[\Delta\tilde{n}(\omega, z = 0)]$. By substituting this expression into Eq. (3.1), we can connect the refractive index change at the surface $\Delta\tilde{n}(\omega, z = 0)$ to the experimentally measured electric field change $\Delta\tilde{E}_R/\tilde{E}_R$.

Now we will introduce the reconstructed optical properties based on the two different model. When the pump pulse penetrates into sample, the intensity decays exponentially with the penetration depth

$$I(\omega, z) = I(\omega, z = 0)e^{-z/d(\omega)} \quad (3.3)$$

For the first model, we assume the refractive index change scales linearly with the pump intensity $\Delta n \propto I$. This assumption was adopted for all the transient optical properties in $\text{YBa}_2\text{Cu}_3\text{O}_{6+x}$ reported in previous works [15–17, 21, 23]. We can derive the relation of depth-dependent refractive index change as

$$\Delta\tilde{n}(\omega, z) = \Delta\tilde{n}(\omega, z = 0)e^{-z/d(\omega)} \quad (3.4)$$

The second model assume that refractive index change scales linearly with the electric field rather than intensity. The linear dependence to intensity becomes a square root dependence $\Delta n \propto \sqrt{I}$, and the relation is then derived as

$$\Delta\tilde{n}(\omega, z) = \Delta\tilde{n}(\omega, z = 0)e^{-z/2d(\omega)} \quad (3.5)$$

This model was recently adopted to reconstruct the transient optical properties in optically-excited K_3C_{60} [46–48].

With the assumptions of Eq. (3.4) and Eq. (3.5), the Eq. (3.1) can be rewritten as the following form

$$\frac{\Delta\tilde{E}_R(\omega)}{\tilde{E}_R(\omega)} = \frac{\Delta\tilde{r} [\Delta\tilde{n}(\omega, z = 0)]}{\tilde{r}_0(\omega)} \quad (3.6)$$

For each probe frequency ω , the reflection coefficient change in the multi-layer system $\Delta\tilde{r}$ is calculated using transfer matrix method. The refractive index change at the surface $\Delta\tilde{n}(\omega, z = 0)$ can be extracted by numerically minimizing the quantity of

$$\left| \frac{\Delta\tilde{E}_R(\omega)}{\tilde{E}_R(\omega)} - \frac{\Delta\tilde{r} [\Delta\tilde{n}(\omega, z = 0)]}{\tilde{r}_0(\omega)} \right| \quad (3.7)$$

Once the $\Delta\tilde{n}(\omega, z = 0)$ is obtained, the non-equilibrium refractive index at sample surface is known by $\tilde{n}(\omega, z = 0) = \tilde{n}_0(\omega) + \Delta\tilde{n}(\omega, z = 0)$ and all other optical properties such as optical conductivity $\tilde{\sigma}(\omega, z = 0)$ can be calculated. All THz spectra reported in the following sections have been reconstructed with the linear dependence model $\Delta n \propto I$. In the last part of this chapter, I will discuss how these two models, linear dependence and square root dependence, affect the reconstructed THz spectra.

3.2 Light-induced optical properties above T_c

As discussed in Section 2.3, the THz-frequency optical responses across the equilibrium superconducting transition are characterized in the frequency-resolved optical conductivity by a reduction of spectral weight in $\sigma_1(\omega)$ and a divergent $1/\omega$ response in $\sigma_2(\omega)$. For the cuprates along the c-axis, the Josephson plasma resonance appears at the frequency where the real part of the dielectric permittivity crosses zero: $\epsilon_1(\omega) = 0$. This results in a peak in the energy loss function $-Im(1/\epsilon(\omega))$ and a plasma edge in the reflectivity spectrum $R(\omega)$.

Here, I will report the experiments presented in the Ref. [15] by S. Kaiser et al. Time-resolved THz reflectivity measurements were conducted upon mid-

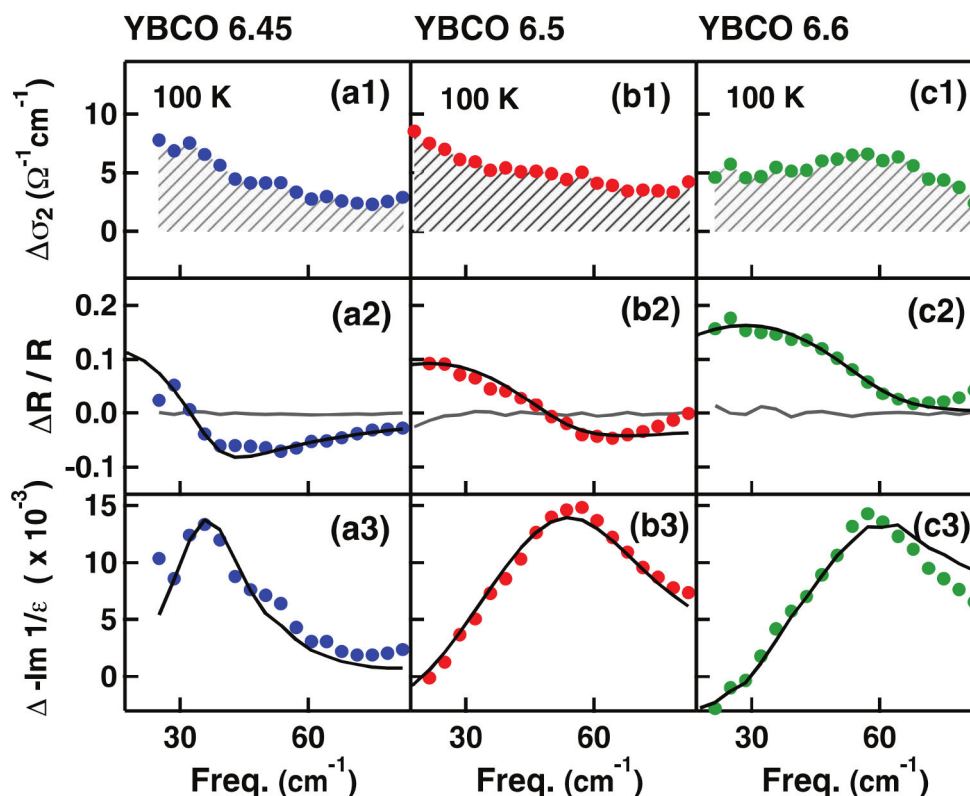


Figure 3.3: Doping-dependent transient optical properties of (a) $\text{YBa}_2\text{Cu}_3\text{O}_{6.45}$, (b) $\text{YBa}_2\text{Cu}_3\text{O}_{6.5}$, and (c) $\text{YBa}_2\text{Cu}_3\text{O}_{6.6}$, 0.6 ps time delay after excitation (dots) at 100 K and high temperature. (a1)–(c1) Dots: Light-induced changes in the imaginary part of optical conductivity $\sigma_2(\omega)$. (a2)–(c2) Dots: Light-induced changes in reflectivity. Black line: Effective medium fit. Gray line: Changes in reflectivity measured at negative time delays. (a3)–(c3) Dots: Light-induced changes in the energy loss function. Black line: Effective medium fit. This figure is reprinted from Ref. [15].

IR excitation on three different underdoped compounds, namely $\text{YBa}_2\text{Cu}_3\text{O}_{6.45}$, $\text{YBa}_2\text{Cu}_3\text{O}_{6.5}$, and $\text{YBa}_2\text{Cu}_3\text{O}_{6.6}$. Broadband mid-IR excitation pulses, with a full width at half maximum of 8 THz and centered at 20 THz, were used to resonantly drive the two apical oxygen infrared phonons. The light-induced changes in the optical properties are summarized in Fig. 3.3. All different doped samples exhibited superconducting-like optical properties including an increase in $\sigma_2(\omega)$ spectral weight, a plasma edge in reflectivity, and a peak in loss function. This suggests that the mid-IR excitation stimulates the inter-bilayer Josephson coupling and induces a transient superconducting state in these compounds at the temperature of 100 K, far above T_c .

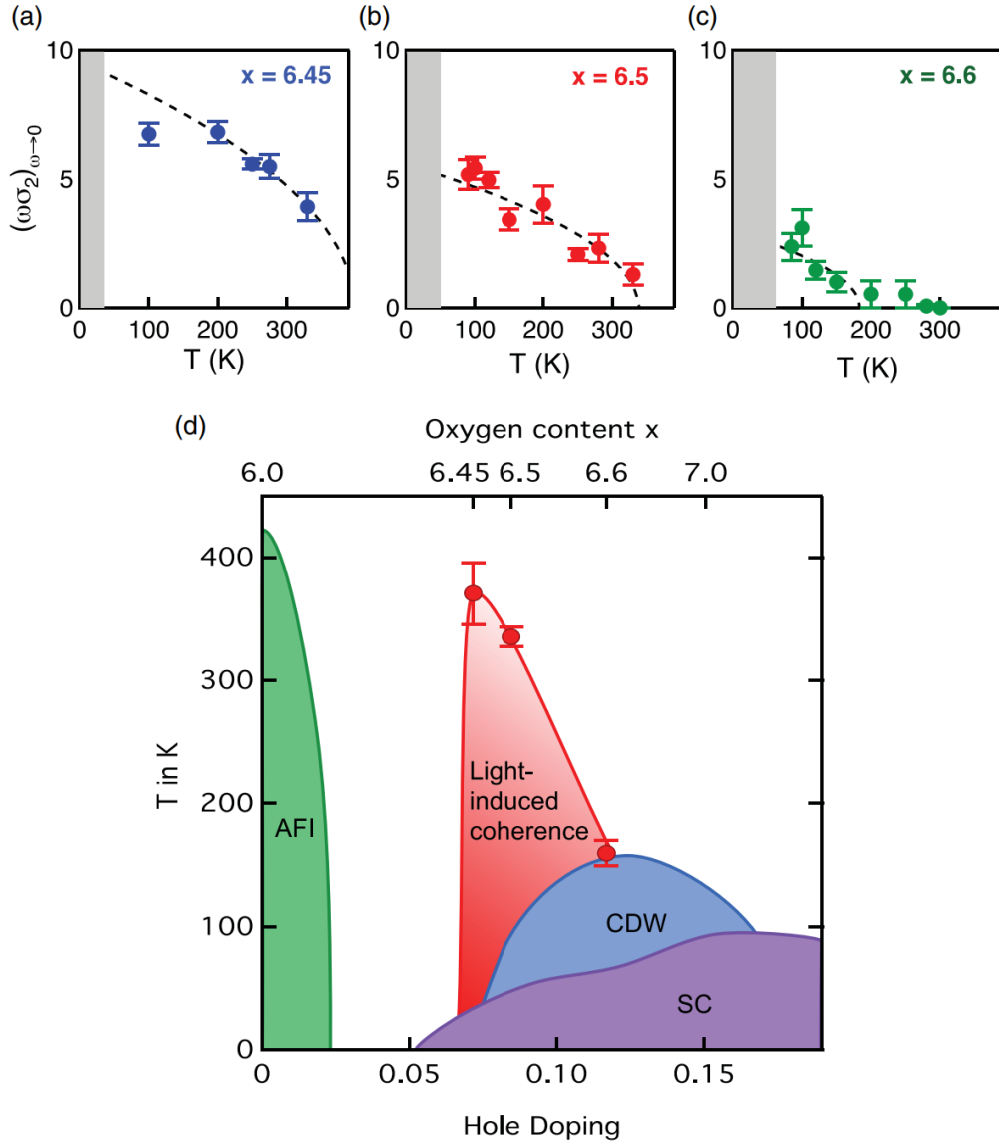


Figure 3.4: Strength of the light-induced inter-bilayer coupling measured in (a) $\text{YBa}_2\text{Cu}_3\text{O}_{6.45}$, (b) $\text{YBa}_2\text{Cu}_3\text{O}_{6.5}$, and (c) $\text{YBa}_2\text{Cu}_3\text{O}_{6.6}$ at 1 ps pump-probe time delay as a function of base temperature and quantified by the zero-frequency extrapolation of the enhancement in imaginary conductivity $\sigma_2(\omega)$. Gray shaded regions refer to the equilibrium superconducting state. (d) Phase diagram of $\text{YBa}_2\text{Cu}_3\text{O}_{6+x}$. AFI, CDW, and SC refer to the equilibrium antiferromagnetic insulating, charge-density-wave, and superconducting phase, respectively. The red circles, estimated from the data in (a)–(c), delimit the region where signatures of possible light-induced superconductivity were measured. This figure is reprinted from Ref. [32]

The same experiments were repeated at higher based temperatures. Figure 3.4a–3.4c show the temperature-dependent light-induced superfluid density, defined by the figure of merit $\lim_{\omega \rightarrow 0} \omega \sigma_2(\omega)$. These temperature-dependences were fitted with an empirical mean field law proportional to $\sqrt{1 - T/T'}$. The fitted T' , a temperature scale for the vanishing of the transient superfluid density, were found to be 370 K, 325 K, and 160 K for the samples $\text{YBa}_2\text{Cu}_3\text{O}_{6.45}$, $\text{YBa}_2\text{Cu}_3\text{O}_{6.5}$, and $\text{YBa}_2\text{Cu}_3\text{O}_{6.6}$, respectively. Figure 3.4d depicts a phase diagram including light-induced superconducting states. Strikingly, the trend of the T' is similar to the pseudo-gap transition temperatures T^* . Previous studies have indicated that pre-formed Cooper pairs without phase coherence exist in the pseudo-gap phase [37–40]. These experimental observations may suggest that excitation of apical oxygen phonons stabilizes the phase fluctuation of the pre-formed Cooper pairs, leading to a transient superconductor at high temperatures. More details of how the driven apical oxygen phonons couple to Josephson plasma polaritons (interlayer superfluid tunneling) will be discussed later in Section 4.2.

3.3 Pump frequency resonances

So far, we have introduced how the broadband 20-THz excitation induces a transient superconducting state in $\text{YBa}_2\text{Cu}_3\text{O}_{6.5}$. Does this phenomenon relate only to the apical oxygen phonons, or could excitations of other infrared phonons or charge transfers also couple to the superconducting state? The frequency-dependent photo-susceptibility of this effect remains unclear at this stage. To address this question, B. Liu et al. conducted time-resolved THz reflectivity experiments using a widely tunable high-intensity laser source to excite the sample across large range of the optical spectrum (3–750 THz) [21, 49, 50].

Figure 3.5a shows the frequency spectra of the THz probe pulses and four different narrowband far-IR pump pulses used in these experiments with the latter tuned to 4.2, 10.1, 16.4, and 19.2 THz to selectively drive different c-axis in-

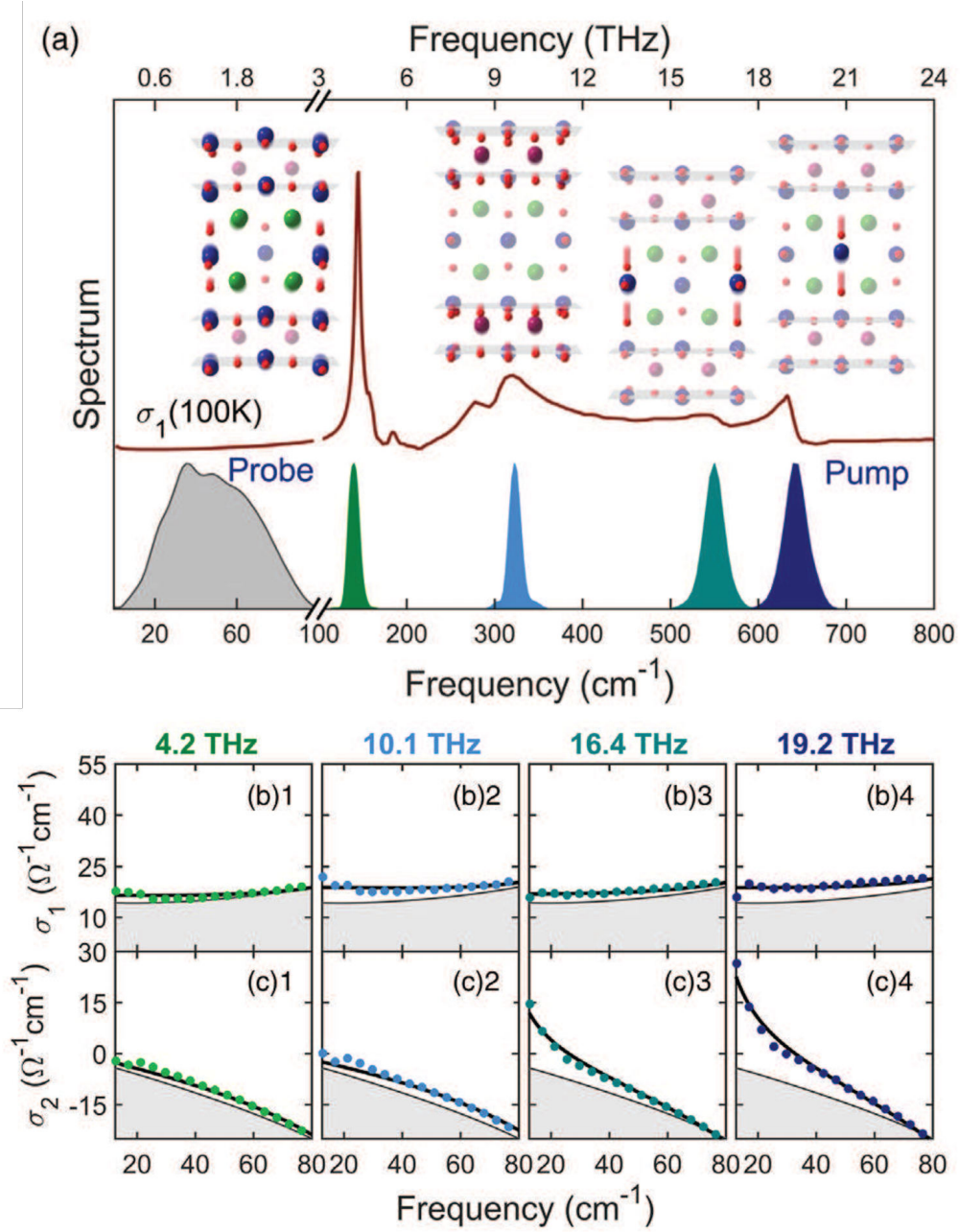


Figure 3.5: Transient THz-frequency optical properties induced by mode selective phonon excitations at the temperature above T_c . (a) The real part of optical conductivity $\sigma_1(\omega)$ of equilibrium $\text{YBa}_2\text{Cu}_3\text{O}_{6.5}$ at 100 K (red line). The frequency spectra of the THz probe (gray) and different narrow-band pump pulses are shown. The pumps are tuned to the resonant frequencies of four different infrared phonons at 4.2, 10.1, 16.4, and 19.2 THz. Inset: Schematic of the atomic motions of each infrared mode. (b),(c) Complex optical conductivity $\sigma_1(\omega) + i\sigma_2(\omega)$ measured at equilibrium (gray lines) and at $t = 0.5$ ps time delay (colored circles). The black solid lines are fits to the transient spectra performed with either a simple Drude-Lorentz model for normal conductors [(b)1, (b)2, (c)1, (c)2] or a model describing the response of a Josephson plasmon [(b)3, (b)4, (c)3, (c)4]. This figure is reprinted from Ref. [21]

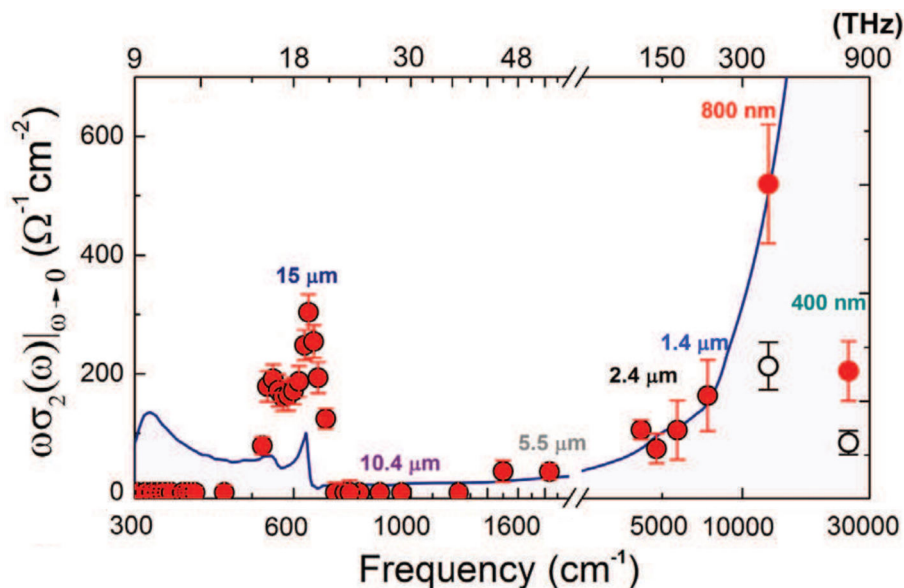


Figure 3.6: Pump frequency dependence of the transient superconducting-like response, determined from the figure of merit $\lim_{\omega \rightarrow 0} \omega \sigma_2(\omega)$ (red circles). The equilibrium real part of optical conductivity $\sigma_1(\omega)$ is shown as a blue line. This figure is adapted from Ref. [21]

frared phonons in $\text{YBa}_2\text{Cu}_3\text{O}_{6.5}$. The narrowband pump enables excitation of lower-frequency phonons at 4.2 and 10.1 THz, as well as individually driving two apical oxygen phonons at 16.4 and 19.2 THz, which could not be separated using the previous broadband 20-THz pump. The transient optical conductivity induced by mode selective phonon excitation are shown in Figs. 3.5b and 3.5c.

As discussed in Section 2.3, the two-fluid model shows that the $\sigma_1(\omega)$ can be entirely attributed to the normal fluid (quasiparticle), while the superfluid contribution appears as a $1/\omega$ divergence in $\sigma_2(\omega)$ spectrum. From the data, the excitation of all the four infrared phonons induced an increase in $\sigma_1(\omega)$, meaning the heating of quasiparticles. However, the superconducting-like response, corresponding to a $1/\omega$ divergence in $\sigma_2(\omega)$, was induced only when the two apical oxygen phonons were driven.

The same experiments were extended to multiple pump frequencies throughout the near-IR and visible light spectra. Figure 3.6 shows the pump frequency dependence of the light-induced superfluid density $\lim_{\omega \rightarrow 0} \omega \sigma_2(\omega)$ in the range from 3 to 750 THz. At the lower-frequency range (3–42 THz), no superconducting signature

is observed at the driving frequencies away from the resonance of apical oxygen phonons. When the pump pulses are tuned to higher-frequency range close to the onset of the charge transfer excitations, the superconducting-like response emerges and the strengths of superfluid follow the optical absorption, depicted as equilibrium $\sigma_1(\omega)$. Here, the authors defined a "photo-susceptibility" of the light-induced state by the normalized quantity of $\lim_{\omega \rightarrow 0} \omega_{probe} \sigma_2(\omega_{probe}) / \sigma_1(\omega_{pump})$. Driving the apical oxygen phonons is the most efficient way to induced the transient superconducting state.

A short conclusion of this work is that light-induced superconductivity in $\text{YBa}_2\text{Cu}_3\text{O}_{6.5}$ is resonant with the natural frequencies of apical oxygen phonons. This resonance suggests that light-induced superconductivity is a coherent effect, where the coherently driven phonons either indirectly or directly enhance superconductivity. For instance, the driven phonons could induce a transient crystal structure that promotes superconductivity or directly couple to the superfluid, strengthening the superconductivity. In Chapter 4, I will explore the microscopic mechanisms of how the driven apical oxygen phonons coherently couple with both the crystal structure and interlayer superfluid tunneling.

3.4 Two-fluid dynamics

In this Section, I will introduce a recent study by A. Ribak et al. [23] focusing on the light-induced dynamics of the uncondensed quasiparticles and the decoherence time of superconducting state, providing first insight into incoherent dynamics that take place in parallel to the light-induced coherent superconducting state.

So far, all the THz reflectivity experiments reported [15, 21] utilized excitation pulses of duration shorter than 600 fs. The resulting transient superconducting state never persists longer than 1 ps after the optical excitation. A. Ribak et al. conducted the THz reflectivity experiments on $\text{YBa}_2\text{Cu}_3\text{O}_{6.48}$ with the same broadband 20-THz pump pulses, but stretched in time to multiple picoseconds, to investigate whether a

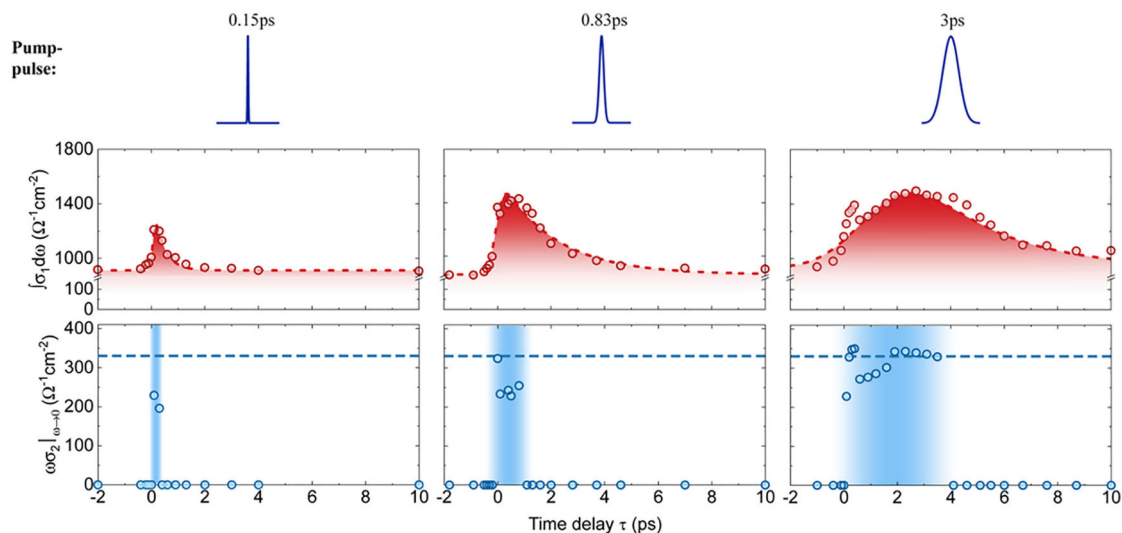


Figure 3.7: Dynamical evolution of the transient spectral weight, $\int_{20\text{cm}^{-1}}^{75\text{cm}^{-1}} \sigma_1(\omega) d\omega$ and the coherent superconducting-like response, $\lim_{\omega \rightarrow 0} \omega \sigma_2(\omega)$, as a function of pump-probe time delay. The peak fields of different pump pulses are set at 2.2 MV/cm. The red dashed lines are fits with a finite rise time and an exponential decay. The blue horizontal lines indicate the equilibrium value of the superfluid density at 10 K. The blue shaded areas represent the time delay window for which coherent superfluid response is detected. This figure is adapted from Ref. [23]

sustained phonon drive could extend the lifetime of the superconducting state. This idea was inspired by another example of light-induced superconductivity in K_3C_{60} , where the long-pulse optical excitation can extend the lifetime of the transient state from a few picoseconds to tens of nanoseconds [13, 51].

The excitation pulses used in these experiments have varying time durations from 150 fs to 4 ps, while maintaining the same spectral content. Figure 3.7 displays the dynamical evolution of the $\sigma_1(\omega)$ spectral weight and the superfluid response $\lim_{\omega \rightarrow 0} \omega \sigma_2(\omega)$ under for pump pulse durations of 0.15, 0.6 and 3.0 picoseconds. Although the superconducting state indeed persists longer when subjected to the sustained phonon drive, its lifetime is nearly equal to the duration of the pump pulses. This suggests that the superconducting-like response only appears while the system is driven and rapidly decays once the drive is off. On the other hand, the $\sigma_1(\omega)$ spectral weight increases in all of the different excitation conditions. The lifetime of these photo-excited quasiparticles clearly exceeds the pump duration by

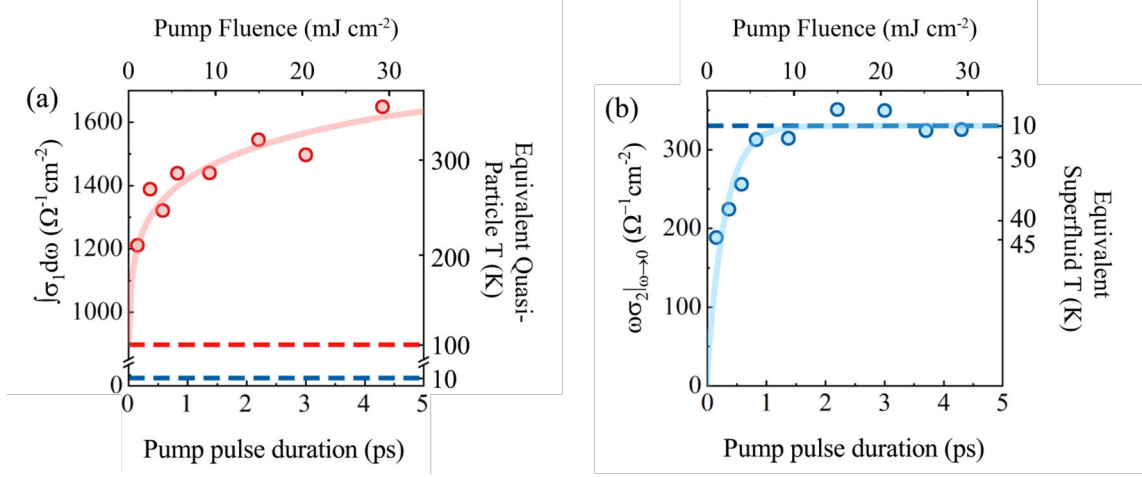


Figure 3.8: (a) The integrated spectral weight and (b) the superconducting-like response, measured at the peak signal strength, as a function of pump duration. The peak field of different pump pulses is a constant and the top horizontal axis indicates the corresponding pump fluence. The red and blue dashed lines in (a) represent the value of integrated spectral weight in equilibrium at 100 K and 10 K, respectively. The blue dashed line in (b) refers to the superfluid density in equilibrium at 10 K. Equivalent temperatures of two fluids are reported on the right axes. This figure is adapted from Ref. [23]

a few picoseconds.

Here, the authors extract "equivalent temperatures" for both superfluid and quasiparticles. These temperatures represent the populations of superfluid or quasiparticles under non-equilibrium conditions as if they were in equilibrium at specific temperatures. In other words, these temperatures allow us to describe how the populations deviate from equilibrium, offering a simplified way to compare non-equilibrium behavior with what would be expected under thermalized conditions. They first calculated the integrated spectral weight $\int_{20\text{cm}^{-1}}^{75\text{cm}^{-1}} \sigma_1(\omega) d\omega$ in transient $\sigma_1(\omega)$ spectra. This value, which can be extracted for every pump probe time delay, is compared with the one in the equilibrium $\sigma_1(\omega)$ spectrum at different temperatures to determine the transient behavior of the temperature of the quasiparticles. The same method is applied to extract the temperature of the superfluid, using the value of $\lim_{\omega \rightarrow 0} \omega \sigma_2(\omega)$. Figure 3.8 shows the peak temperatures of the two fluids as a function of the pump pulse duration. In the driven superconducting state, the quasiparticles increase in temperature to nearly 300 K. As the pump duration

lengthens while keeping the peak electric field a constant, the peak temperature of the quasiparticles rises correspondingly. In contrast, as the pump pulse duration reaches about 1 picosecond, the light-induced superfluid density saturates at the equilibrium value observed at 10 K. This may suggest that the phonon drive synchronizes pre-existing Cooper pairs that are without phase coherence above T_c before the arrival of the excitation pulse, rather than creating new Cooper pairs.

In summary, the lifetime of the transient superconducting state can be extended but never persists longer than the pump pulse duration. We suspect that once the drive is off, the induced superfluid is affected by incoherent carriers, including quasiparticles and phonons, causing it to decay rapidly. Therefore, understanding the dynamics of these incoherent carriers is crucial, and this topic will be discussed later in Chapter 5.

Model comparison of transient optical conductivity

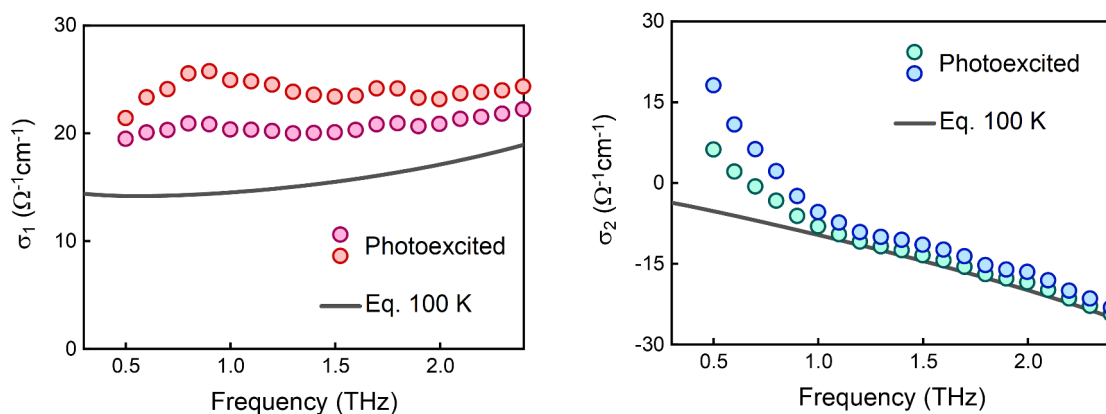


Figure 3.9: C-axis complex optical conductivity $\sigma_1(\omega)$, $\sigma_2(\omega)$ of $\text{YBa}_2\text{Cu}_3\text{O}_{6.48}$. The gray line and colored circles represent the equilibrium and photoinduced $\sigma_1(\omega)$, $\sigma_2(\omega)$ at $T = 100$ K, respectively. The latter was calculated from the data of Ref. [23] with two different models, one based on a linear dependence (red, blue) and another one based on a square root dependence (purple, green) of the photoinduced response on the pump fluence [47, 48]. This figure is adapted from Ref. [24]

Here, I highlight a dataset from Ref. [23] showing the transient THz-frequency optical conductivity in $\text{YBa}_2\text{Cu}_3\text{O}_{6.48}$ induced by 0.83 ps mid-IR excitation, as illustrated in Fig. 3.9. Using the reconstruction procedure described in Section 3.1,

we applied two models: one based on the linear dependence $\Delta n \propto I$ (red, blue) and the second one based on the square root dependence $\Delta n \propto \sqrt{I}$ (purple, green). Both models reveal an increase in $\sigma_1(\omega)$ and a $1/\omega$ divergence in $\sigma_2(\omega)$, indicative of quasiparticle heating and a superconducting-like response. However, the amplitude of the spectral weight changes in both $\sigma_1(\omega)$ and $\sigma_2(\omega)$ differs between the models. The linear model gives larger changes compared to the square root model. Although the two models show identical phenomenological description, they produce quantitatively different results when determining the equivalent temperatures of quasiparticles and superfluid. This dataset will be used to compare with the Raman data presented in Chapter 5.

Chapter 4

Coherent couplings in optically-driven $\text{YBa}_2\text{Cu}_3\text{O}_{6.48}$

The resonant excitation of apical oxygen infrared phonons in $\text{YBa}_2\text{Cu}_3\text{O}_{6.48}$ has been shown to induce superconducting-like features in the THz frequency optical conductivity, suggesting a possible light-induced superconductivity up to room temperature [15–17,21,23]. In this chapter, I will introduce possible microscopic mechanisms underlying this effect, based on a series of time-resolved experiments that unraveled the coherent coupling between the resonantly driven apical oxygen phonons and other coherent modes in the systems, such as optical phonons and Josephson plasmon polaritons [18,19,22].

In Section 4.1, I will discuss the coherent coupling between the driven phonons and low-frequency Raman phonons, which gives rise to a transient lattice displacement and a new non-equilibrium crystal structure. A theory of cubic-order nonlinear phononic coupling and the detection method of time-resolved reflectivity measurements will be introduced. In Section 4.2, the coherent coupling between the driven apical oxygen phonons and Josephson plasmon polaritons will be discussed. Time-resolved second harmonic generation (SHG) measurements revealed a parametric amplification process of a low-frequency electronic mode, Josephson

plasmon, which were proposed to stimulate the superconducting state in optically driven $\text{YBa}_2\text{Cu}_3\text{O}_{6.48}$.

4.1 Coherent phonon-phonon coupling

4.1.1 Nonlinear phononics: cubic order coupling

Nonlinear phononics exploits intense laser pulses in the mid-IR and THz frequency range to resonantly drive infrared-active optical phonons to large amplitudes, beyond the harmonic approximation. The anharmonicities of crystal lattices then allow for nonlinear interactions between lattice vibrations to induce transient structural deformations along one or multiple phonon coordinates and, potentially, to drive the material into a non-equilibrium electronic and magnetic phase [8–14, 52–55]. To describe how the driven infrared phonons couple to the other phonon modes through nonlinear phononic couplings, we first express the potential energy of the crystal lattice as

$$V_{lattice} = \frac{1}{2}\omega_{IR}^2 Q_{IR}^2 + \sum_i \frac{1}{2}\omega_i^2 Q_i^2 - Z^* Q_{IR} E + V_{anh} \quad (4.1)$$

where ω is the natural frequency and Q is normal coordinate of any phonon mode. The first and second terms represent the harmonic contributions of the lattice potential for the driven infrared mode and other coupled modes, respectively. The third term is the external potential describing the interaction between the infrared phonon and the applied electric field E of a resonantly tuned light pulse, where Z^* is the effective charge of the infrared mode. The last term V_{anh} includes all the anharmonic contributions of the lattice potential. When we drive the infrared-active mode Q_{IR} to large amplitude, the anharmonic lattice potential can be expressed as

$$\begin{aligned} V_{anh} = & \sum_{j>2} a_j Q_{IR}^j + \sum_i (a_{12} Q_{IR} Q_i^2 + a_{21} Q_{IR}^2 Q_i) \\ & + \sum_i (a_{22} Q_{IR}^2 Q_i^2 + a_{13} Q_{IR} Q_i^3 + a_{31} Q_{IR}^3 Q_i) + \dots \end{aligned} \quad (4.2)$$

The first summation denotes high-order harmonics of the driven infrared mode. The second and third summations describe cubic-order and quartic-order coupling between the driven infrared mode and the coupled modes.

Here, we focus on the cubic-order coupling and restrict the discussion to centrosymmetric crystals like $\text{YBa}_2\text{Cu}_3\text{O}_{6.48}$. The anharmonic lattice potential V_{anh} must obey the symmetry of the material. Since the infrared-active mode has odd parity, the first cubic-order coupling term, $a_{12}Q_{IR}Q_i^2$, is always symmetry-odd and hence zero in a centrosymmetric crystals. The second cubic-order coupling term, $a_{21}Q_{IR}^2Q_i$, will be a non-zero value only if the coupled modes Q_i are even-parity Raman-active modes. Therefore, if we consider the cubic coupling between an infrared-active mode and a Raman-active mode, the anharmonic lattice potential can be simplified as $V_{anh} = a_{21}Q_{IR}^2Q_R$. The lattice potential energy becomes

$$V_{lattice} = \frac{1}{2}\omega_{IR}^2Q_{IR}^2 + \frac{1}{2}\omega_R^2Q_R^2 - Z^*Q_{IR}E + a_{21}Q_{IR}^2Q_R \quad (4.3)$$

Next, we derive the dynamics of the infrared mode and Raman mode. The equation of motion for any phonon mode in the crystal is

$$\frac{\partial^2 Q}{\partial t^2} + \Gamma \frac{\partial Q}{\partial t} + \omega^2 Q = F \quad (4.4)$$

where Γ is a phenomenological damping constant and F is the driving force to this phonon mode. The infrared-active mode Q_{IR} can directly couple to the light field as its oscillatory motion changes the dipole moment. Hence, the force term of Q_{IR} can be written as

$$F_{IR} = Z^*E(t) - \frac{\partial V_{anh}}{\partial Q_{IR}} = Z^*E(t) - 2a_{21}Q_{IR} \quad (4.5)$$

The electric field of laser pulse is $E(t) = A(t)e^{i\omega_{IR}t}$, which oscillates at frequency ω_{IR} under the Gaussian envelop $A(t)$. The Raman-active mode Q_R only modulates the lattice polarizability, hence does not couple to light directly, equivalent to a zero effective charge Z^* of the Raman mode. The force term of Q_R then becomes

$$F_R = -\frac{\partial V_{anh}}{\partial Q_R} = -a_{21}Q_{IR}^2 \quad (4.6)$$

We note that the Raman mode can also be driven by light indirectly via an impulsive force proportional to $E(t)^2$. However, this effect is negligible when the excitation light field is resonant with the infrared phonon mode Q_{IR} .

Substituting the force terms into Eq. (4.4), we can derive the equations of motion for the driven infrared mode and the coupled Raman mode

$$\frac{\partial^2 Q_{IR}}{\partial t^2} + \Gamma_{IR} \frac{\partial Q_{IR}}{\partial t} + \omega_{IR}^2 Q_{IR} = Z^* E(t) - 2a_{21} Q_R \quad (4.7)$$

and

$$\frac{\partial^2 Q_R}{\partial t^2} + \Gamma_R \frac{\partial Q_R}{\partial t} + \omega_R^2 Q_R = -a_{21} Q_{IR}^2 \quad (4.8)$$

By solving Eq. (4.7) and Eq. (4.8), the typical time evolution of these two phonon modes are illustrated in Fig. 4.1. Here, we consider the 20-THz center frequency infrared-active mode, driven by a Gaussian electric field pulse with time duration of 200 fs FWHM, which couples to a 4-THz center frequency Raman mode through the cubic coupling term $a_{21} Q_{IR}^2 Q_R$.

The dominant drive of the infrared mode Q_{IR} is the laser pulse ($Z^* E \gg 2a_{21} Q_R$) and, after optical excitation, it decays with the phonon lifetime $\tau_{IR} = 1/\Gamma_{IR}$. Note that the time average of the Q_{IR} amplitude is zero, meaning that there is no net structural displacement along the infrared mode coordinate. In contrast, the Raman mode Q_R is driven by a directional force proportional to Q_{IR}^2 and undergoes a rectified displacement following the envelop of the force. If the rise time of Q_{IR}^2 is shorter than the period of the Raman mode, this mode will oscillate at its natural frequency and decay with its lifetime $\tau_R = 1/\Gamma_R$. Importantly, the time-averaging of Q_R motion is non-zero, implying that the cubic phononic coupling induces a net structural displacement along the Raman mode coordinate. In a real crystal, the driven infrared mode can couple to multiple Raman modes and the overall displacement due to the phononic coupling will lead to a structural deformation that breaks the crystal symmetry. Potentially, this effect may drive the crystal into a non-equilibrium electronic or magnetic phase [8–14, 52–55].

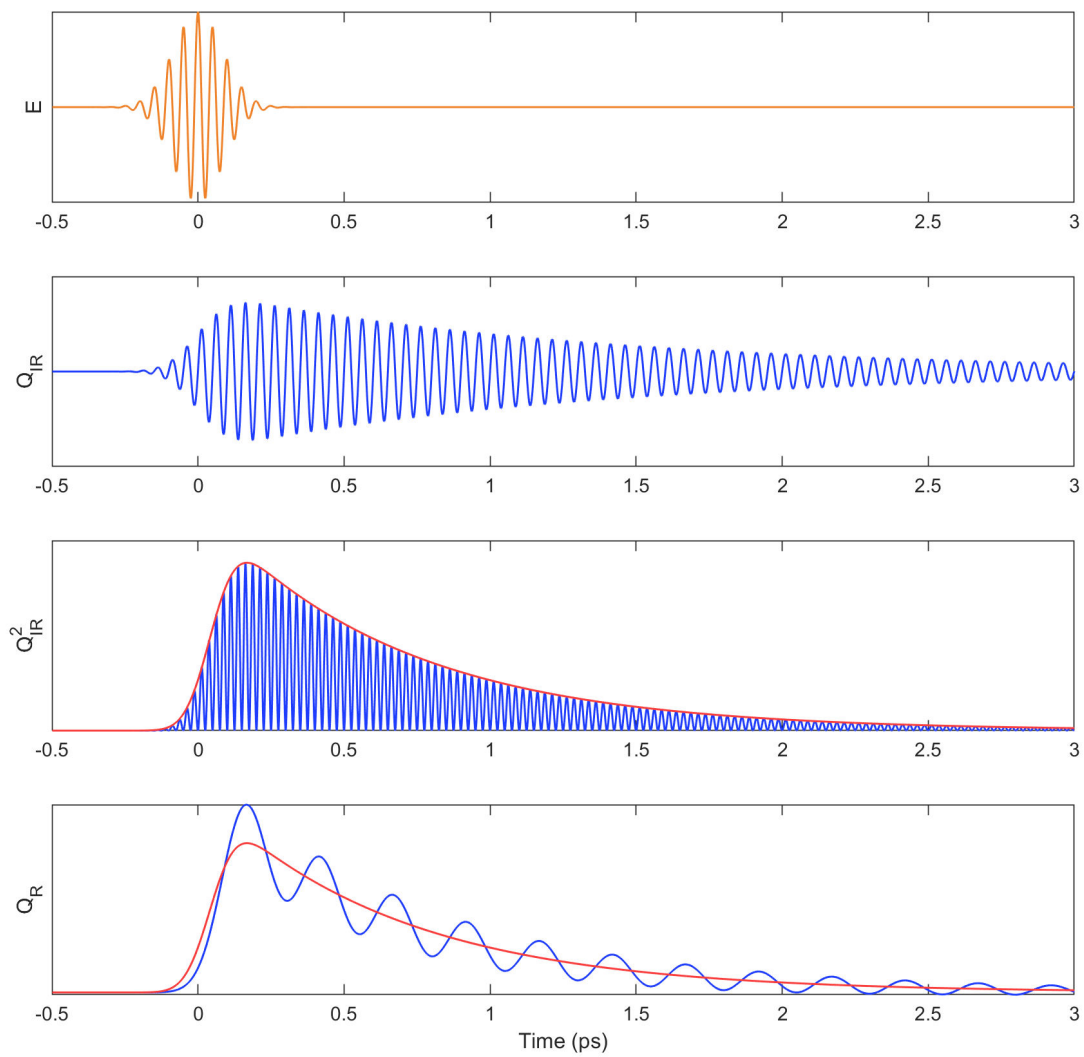


Figure 4.1: The time evolution of Gaussian electric field (yellow), driven infrared phonon Q_{IR} , directional force Q_{IR}^2 , and the coupled Raman phonon Q_R . Blue lines represent the motion of phonon modes and red line is the envelop of the force.

4.1.2 Time-resolved reflectivity measurements

The nonlinearly coupled Raman modes can be detected by measurements of the ultrafast time-resolved reflectivity. This technique relies on the use of two ultrafast laser pulses: *pump* and *probe*. The pump pulse is used to excite the materials into a higher-energy state. The probe pulse allow us to track the time evolution of optical properties by varying the time delay between pump and probe pulses. When the pump pulse drives coherent collective modes in a solid system, these modes modulate the optical constants of the solid, manifesting as coherent oscillations in the optical detection of the probe pulses. These coherent collective modes can be categorized into two types: even modes (such as Raman phonons) and odd modes (such as infrared phonons), each requiring different types of probe detection methods [19,22]. In this Section, I will focus on detecting the coherent even modes.

The theory of detecting coherent Raman phonons in the time-resolved reflectivity measurements has been discussed for example in Ref. [56]. This paper mainly discussed impulsive stimulated Raman scattering, which involves the application of an ultrashort pulse of electric field in the visible or near-infrared to impulsively drive the Raman mode. In this case, the equation of motion for the Raman mode is derived as

$$\frac{\partial^2 Q_R}{\partial t^2} + \Gamma_R \frac{\partial Q_R}{\partial t} + \omega_R^2 Q_R = \frac{1}{2} \frac{\partial \chi^{(1)}}{\partial Q_R} E_p^2 \quad (4.9)$$

where E_p is the electric field of pump pulse, $\chi^{(1)}$ is the linear susceptibility of the crystal, and $\frac{\partial \chi^{(1)}}{\partial Q_R}$ is the Raman scattering coefficient. This equation is analogous to cubic phononic coupling Eq. (4.8). The only difference is that the driving force is proportional to E^2 rather than Q^2 . In our case of mid-IR excitation, the driving force on the Raman mode consists of both E^2 and Q^2 components, with the Q^2 being much larger than E^2 . Although the mechanisms of pump driving differs, the probe detection method is the same as impulsive stimulated Raman scattering.

When the electric field of the incident probe pulse E_i interacts with the crystal,

the induced polarization can be expressed as

$$P = \chi^{(1)} E_i + \frac{\partial \chi^{(1)}}{\partial Q_R} Q_R E_i + \dots \quad (4.10)$$

The first term is the linear response and the second term describes the Raman scattering process, where the Raman mode Q_R modulates linear susceptibility $\chi^{(1)}$.

The nonlinear wave equation for this process reads

$$\frac{\partial^2 E}{\partial z^2} + \frac{n^2}{c^2} \frac{\partial^2 E}{\partial t^2} = \frac{4\pi}{c^2} \frac{\partial \chi^{(1)}}{\partial Q_R} \frac{\partial^2 (Q_R E_i)}{\partial t^2} \quad (4.11)$$

where E is the electric field of the emerging probe pulse (the electric field reflected from the sample). This expression is based on the assumption that the incident probe field E_i is not depleted during the interaction, and the dispersion on refractive index n can be ignored as the spectral changes to the emerging probe field E is a small frequency shift. According to Ref. [56], the general solution to Eq. (4.11), using the boundary condition $E(t = 0, z = 0) = E_i(t = 0, z = 0)$, is

$$E(z, t) = E_i(t) - \frac{2\pi z}{cn} \frac{\partial \chi^{(1)}}{\partial Q_R} \frac{\partial}{\partial t} [Q_R(t + \Delta t) E_i(t)] \quad (4.12)$$

Here, we define $t = 0$ as the time when the probe pulse strikes the crystal, and the pump pulse arrives earlier than probe pulse by a time delay Δt . The motion of the Raman mode driven by the pump pulse is

$$Q_R(t + \Delta t) = Q_{R0} \sin(\omega_R(t + \Delta t)) \quad (4.13)$$

We then substitute Eq. (4.13) into Eq. (4.12) and conduct Fourier transformation on Eq. (4.12) to obtain the spectral content of the emerging probe field E . We get

$$E(z, \omega) e^{-in\omega z/c} = E_i(\omega) + B\omega [e^{i\omega_R \Delta t} E_i(\omega + \omega_R) - e^{-i\omega_R \Delta t} E_i(\omega - \omega_R)] \quad (4.14)$$

where $B = \frac{\pi Q_{R0} l}{cn} \frac{\partial \chi^{(1)}}{\partial Q_R}$, and l is the coherent length of pump and probe pulses. This equation reveals that the emerging probe field comprises three spectral components: the original field with the frequency ω and two shifted fields with the frequencies $\omega + \omega_R$ and $\omega - \omega_R$, corresponding to Anti-Stokes and Stokes Raman scatterings. If

the time duration of probe pulse is longer than twice the period of the Raman mode, the spectrum of the emerging probe pulse becomes three distinct and separated peaks at ω , $\omega + \omega_R$, and $\omega - \omega_R$. The original field and the shifted field do not affect each other. In contrast, if the probe pulse is shorter than twice the period of the Raman mode, the spectrum becomes three broadband peaks and three fields are spectrally overlapped. This results in an interference among the original field and the shifted fields. The interference depends on the pump and probe time delay Δt .

Finally, we calculate the intensity spectrum $I(\omega) = |E(\omega)|^2$ from the Eq. (4.14). We get

$$\begin{aligned}
 I(\omega, \Delta t) = & E_i(\omega)^2 + 2B\omega \cos(\omega_R \Delta t) E_i(\omega) [E_i(\omega + \omega_R) - E_i(\omega - \omega_R)] \\
 & - 2B^2\omega^2 \cos(2\omega_R \Delta t) E_i(\omega + \omega_R) E_i(\omega - \omega_R) + B^2\omega^2 [E_i(\omega + \omega_R)^2 + E_i(\omega - \omega_R)^2]
 \end{aligned} \tag{4.15}$$

The first term is the intensity of the original field. Most of the incident probe pulse intensity is transmitted through or reflected by the material, unaffected by the interaction. The second term represents the interference of the original field and the two shifted fields, also known as *heterodyne* component. This leads to a coherent oscillation at the frequency of ω_R in time domain. The third term is called *homodyne* component. The interference between two shifted fields results in an oscillation with the frequency $2\omega_R$. The fourth term is the intensity of two shifted fields. The last two terms with the coefficient $B^2\omega^2$ are negligible as the factor $B\omega$ is much smaller than 1.

To obtain the time delay dependent probe intensity $I(\Delta t)$, one needs to integrate Eq. (4.15) across all the frequency components, which yields

$$I(\Delta t) = \int I(\omega, \Delta t) d\omega = I_{probe} + \cos(\omega_R \Delta t) I_{hetero} + \cos(2\omega_R \Delta t) I_{homo} \tag{4.16}$$

where I_{probe} includes the intensities of the original field and the shifted fields, I_{hetero} and I_{homo} represents the intensities of heterodyne and homodyne components, respectively. The probe intensity change is dominated by the heterodyne component

($I_{hetero} \gg I_{homo}$), which shows a coherent oscillation with time delay Δt at the Raman phonon frequency ω_R .

Therefore, the time delay dependent probe intensity changes is dominated by the *heterodyne* component, which gives a coherent oscillation with one time of Raman phonon frequency. In the actual experiments, the incoherent dynamics induces a slowly varying background and the coherent oscillation appears on top of it.

4.1.3 Transient lattice displacements in $\text{YBa}_2\text{Cu}_3\text{O}_{6.48}$

In Section 4.1.1, we showed that the driven infrared phonons can coherently couple to a number of Raman phonons via cubic-order coupling, which gives rise to a directional displacement and a coherent oscillation for each Raman modes. Section 4.1.2 established an experimental method to detect which Raman modes involve this coupling. Based on the above-mentioned theory and experiment, previous works have investigated the coherent phonon-phonon coupling in $\text{YBa}_2\text{Cu}_3\text{O}_{6.48}$ and discuss how a transient crystal structure could potentially result in the light-induced superconducting state [18, 19, 22].

Figure 4.2 depicts the time-resolved reflectivity measurements on the optically driven $\text{YBa}_2\text{Cu}_3\text{O}_{6.48}$. The pump pulse of 200-fs duration and mid-IR frequency resonantly drives the 20-THz and 17-THz infrared-active apical oxygen phonons. The probe pulse of 30-fs duration and 800-nm wavelength was used to record the pump-induced reflectivity changes ΔR . These data were reproduced from Ref. [22] Fig. 1b. The ΔR signal experiences a prompt drop at time zero, followed by an exponential recovery back to the original signal strength. On top of this slowly varying background, an oscillatory response was observed indicating the coupled coherent Raman phonons. Figure 4.3 shows the background-subtracted ΔR and the corresponding Fourier spectrum. We can see a strong peak at 3.7 THz, two small peaks at 4.6 and 5.1 THz, and possibly a hidden peak at around 2.8 THz. This 2.8 THz peak was reported in another time-resolved reflectivity measurements

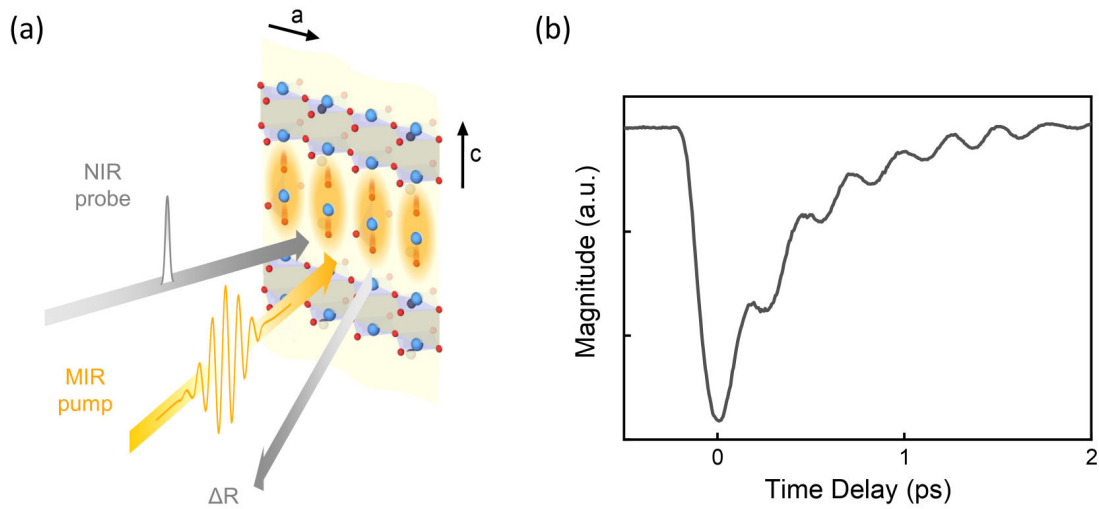


Figure 4.2: (a) Schematic of time-resolved optical reflectivity spectroscopy. The mid-IR pump pulse (yellow) resonantly drives infrared-active c-axis apical oxygen phonons in $\text{YBa}_2\text{Cu}_3\text{O}_{6.48}$. Near-infrared probe pulses (gray) were detected in reflection geometry. Gray arrow represents reflectivity changes at the fundamental frequency (ΔR). (b) ΔR (gray) shows an oscillatory response appearing on top of a slowly varying background. These data were reproduced from Ref. [22] Fig. 1b.

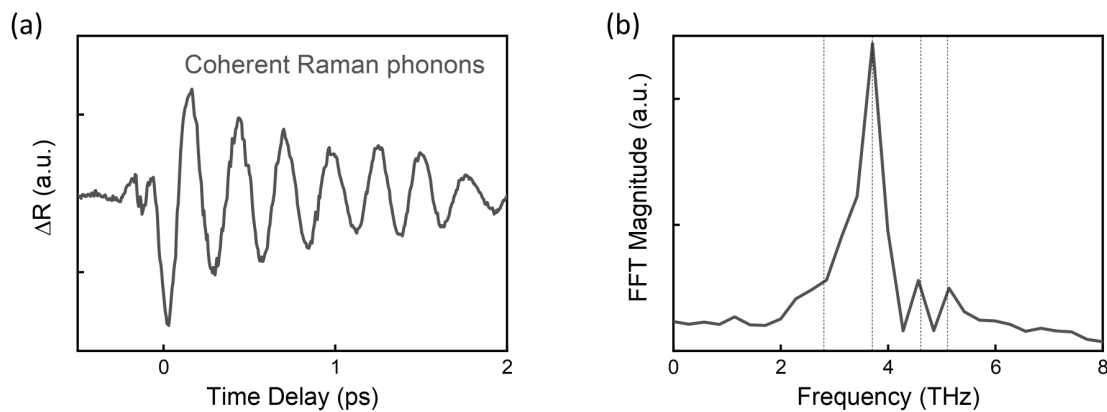


Figure 4.3: (a) The ΔR data after subtraction of a slowly varying background. The oscillatory response represents the coupled coherent Raman phonons. (b) The Fourier spectrum of the ΔR data. The dash lines indicate the natural frequencies of Raman phonons.

(see Ref. [19]). These peaks can be assigned to different c -axis A_g Raman modes in ortho-II ordered $\text{YBa}_2\text{Cu}_3\text{O}_{6+x}$ [18, 57, 58]. According to density functional theory (DFT) predictions, more Raman modes can be driven by the infrared modes due to the cubic phononic coupling [19]. However, these modes were likely undetected in time-resolved reflectivity measurements because their higher frequencies result in oscillation periods shorter than the rise time of Q_{IR}^2 force.

While the time-resolved reflectivity measurements reveal which Raman modes are driven and oscillate, they do not provide information about whether these Raman modes undergo atomic displacements. To address this, R. Mankowsky et al. studied the lattice dynamics in optically-driven $\text{YBa}_2\text{Cu}_3\text{O}_{6.48}$ using femtosecond hard X-ray diffraction [18]. This technique allows for the direct probing of real-time atomic position changes, enabling the investigation of the lattice displacements driven by the cubic phononic couplings. Figure 4.4b depicts the changes in diffracted intensities of the $(-2 -1 1)$ and the $(-2 0 4)$ Bragg peaks. Both peaks exhibit a prompt rise followed by an exponential decay was observed in both Bragg peaks, indicating that the lattice is indeed displaced by the optical driving. The temporal profile of the lattice displacement matches with the timescale of the light-induced superconducting state, suggesting a possible connection between these two effects.

In Ref. [18], they combined DFT calculation and fits to the all the measured Bragg diffraction peaks to reconstruct transient crystal structure in $\text{YBa}_2\text{Cu}_3\text{O}_{6.48}$. As shown in Figure 4.4a, three key structural changes emerge in this new crystal configuration: 1) In the CuO_2 planes, the buckling of O-Cu-O bonds is enhanced. 2) The distance between apical oxygen atoms O(4) and the copper atoms Cu(2) in the CuO_2 planes is reduced by 1% (see Fig. 4.4c). 3) The distance of intra-bilayer increases and the distance of inter-bilayer decreases. To connect these structural changes with the light-induced superconductivity, a DFT calculation based on this new crystal structure predicted that the atomic motions modulate the density of states of Cu-O chains and CuO_2 planes. This induces charge transfer processes from the planes to the chains, effectively increasing hole doping in the CuO_2 planes

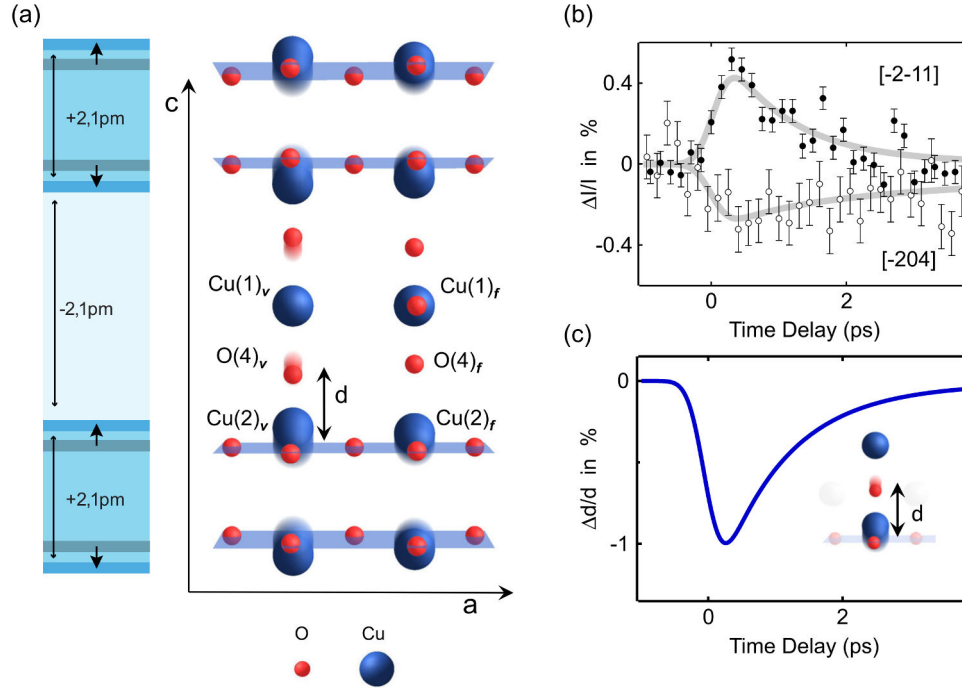


Figure 4.4: (a) Transient crystal structure of $\text{YBa}_2\text{Cu}_3\text{O}_{6.48}$, showing the apical oxygen atoms $\text{O}(4)$ and the copper atoms $\text{Cu}(2)$ in the CuO_2 planes. The distance between the $\text{O}(4)$ and $\text{Cu}(2)$ decreases after photoexcitation. (b) Time evolution of x-ray diffraction intensity changes recorded at two different Bragg reflections. (c) Time evolution of the distance changes between $\text{O}(4)$ and $\text{Cu}(2)$. This figure is reprinted from Ref. [20]

[18,20]. Such a self-doping effect has been previously linked to temperature-driven superconducting transition in equilibrium $\text{YBa}_2\text{Cu}_3\text{O}_{6.48}$ and it could potentially explain the formation of superconducting phase [18].

In conclusion, the coherent third-order phonon-phonon coupling in $\text{YBa}_2\text{Cu}_3\text{O}_{6.48}$ induces a transient crystal structure, which potentially favors superconductivity. However, the phonon-phonon coupling is an indirect effect to superconductivity and may not fully explain the observation of light-induced superconductivity in $\text{YBa}_2\text{Cu}_3\text{O}_{6.48}$ at room temperature. A more probable scenario is that the driven phonons directly couple to the superfluid. In the next Section, I will discuss more recent experiments on the coherent coupling between the driven phonons and the Josephson plasmon polaritons (JPP), which lead to an alternative mechanism for the light-induced superconducting state in the bilayer cuprate.

4.2 Coherent phonon-plasmon coupling

4.2.1 Modelling the phonon-plasmon coupling in $\text{YBa}_2\text{Cu}_3\text{O}_{6.48}$

References [22, 59] have proposed a three-mode mixing model to describe the coherent phonon-plasmon coupling in the optically driven $\text{YBa}_2\text{Cu}_3\text{O}_{6.48}$. This model describes a nonlinear parametric interaction between the driven phonon and a pair of inter-bilayer and intra-bilayer JPPs. The potential energy of this system including the driven phonon and two JPPs can be expressed as

$$V = \frac{1}{2}\omega_{IR}^2 Q_{IR}^2 + Z^* Q_{IR} E + \omega_{J_1}(q_x)^2 J_{1,q_x} J_{1,-q_x} + \omega_{J_2}(q_x)^2 J_{2,q_x} J_{2,-q_x} + V_{ph-pl} \quad (4.17)$$

The first and second terms describe the harmonic potential of the driven phonon and its coupling to light field. The third and fourth terms denote the harmonic potential of inter- and intra-bilayer JPPs, where J_1 and J_2 are the corresponding current coordinates. q_x is the finite in-plane momentum and $\omega_{J_1, J_2}(q_x)$ represents the in-plane dispersion of JPPs. The dispersion curves are depicted in Figs. 4.5a and 4.5b.

The interaction potential of phonon and plasmon is given by

$$V_{ph-pl} = \alpha q_x^2 Q_{IR} (J_{1,q_x} J_{2,-q_x} + J_{2,q_x} J_{1,-q_x}) \quad (4.18)$$

where α is the phonon-plasmon coupling coefficient. The vibrations of the apical oxygen phonons modulate the superfluid densities in a bilayer structure in an anti-symmetric manner between the two CuO_2 planes. This oscillatory effect leads to an alternating increase and decrease in the kinetic energy of neighboring planes. The modulation of in-plane kinetic energy perturbs the gradient of the phase of the superconducting order parameter in the planes. As a result, the Josephson tunneling current becomes dependent on the in-plane spatial coordinate.

According to Eq. (4.17), the equations of motion for the two JPPs are written as

$$\frac{\partial^2 J_1}{\partial t^2} + \Gamma_{J_1} \frac{\partial J_1}{\partial t} + \omega_{J_1}(q_{x_1})^2 J_1 = -\alpha q_{x_1}^2 Q_{IR} J_2 \quad (4.19)$$

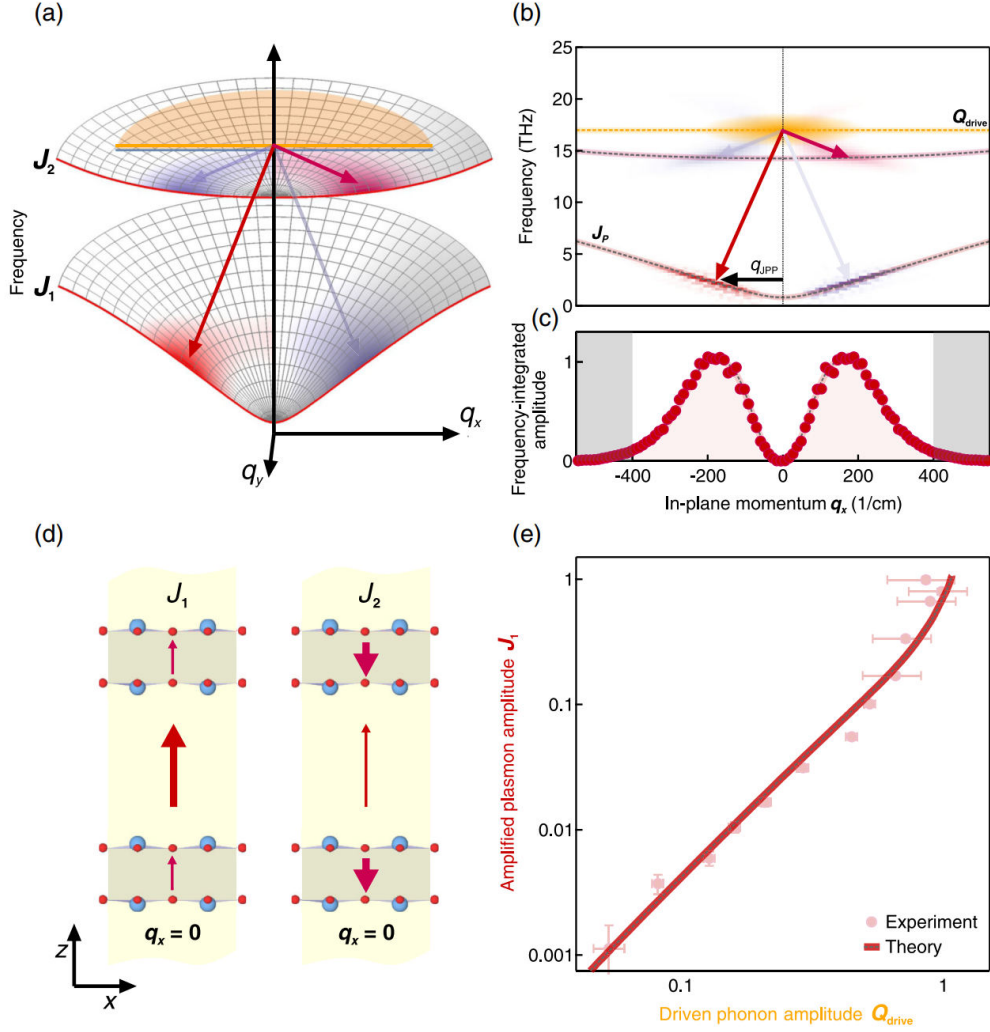


Figure 4.5: (a) Dispersion of the interbilayer (J_1) and intrabilayer (J_2) JPP modes along the in-plane momenta q_x and q_y in $\text{YBa}_2\text{Cu}_3\text{O}_{6.48}$. The red lines are a cut through the $q_y = 0$ plane. The apical oxygen phonon mode at 17 THz (yellow) does not disperse along either direction. The three-mode mixing process is sketched as red and blue arrows and results from a numerical simulation in response to the resonant drive of the apical oxygen phonon at $q = 0$ are shaded in the same colors. The response vanishes along q_y , parallel to the light propagation direction. (b) Detailed insight into the simulation results along q_x for $q_y = 0$. The driven phonon with zero momentum excites a pair of JPPs, J_1 and J_2 , with opposite wave vectors q_{JPP} and frequencies that add up to the phonon frequency. The two processes for mirrored momentum transfer are shown as red and blue arrows, respectively. (c) Amplitude of the JPPs obtained integrating along the vertical frequency axis of (b). The amplitude is zero for $q_x = 0$, and peaks at $q_x = 200$ cm $^{-1}$. (d) Sketch of the two JPPs at $q = 0$, with the supercurrents oscillating in phase (J_1) or out of phase (J_2) for the low- and high-frequency mode, respectively. The thicknesses of the arrows indicate the supercurrent strengths within and between the bilayers. (e) Simulated excitation strength dependence (dashed line) of the low-frequency 2.5-THz oscillations, together with the experimental data (dots). This figure is reprinted from Ref. [22].

$$\frac{\partial^2 J_2}{\partial t^2} + \Gamma_{J_2} \frac{\partial J_2}{\partial t} + \omega_{J_2} (q_{x_2})^2 J_2 = -\alpha q_{x_2}^2 Q_{IR} J_1 \quad (4.20)$$

These equations predict a three-mode mixing process between the apical oxygen phonon and inter- and intra-bilayer JPPs at finite momenta. The driving force is proportional to the square of the JPP momentum q_x^2 , which means the driven phonon couples most effectively with supercurrents at finite in-plane wave vectors. The two involved JPPs must satisfy the energy conservation condition $\omega_{J_1} + \omega_{J_2} = \omega_{IR}$ and their momenta must be equal and opposite $q_{x_1} = -q_{x_2}$. Figure 4.5b illustrates a frequency-momentum diagram showing the pathway of phonon-plasmon coupling, where the 17-THz driven phonon couples to the 2.5-THz lower JPP and 14.5-THz upper JPP with in-plane momenta of $\pm 200 \text{ cm}^{-1}$.

This model also predicts that as the strength of the driven phonon increases, the coupled JPPs will be exponentially amplified. Figure 4.5e plots the relation between amplitudes of the JPPs the driven phonon, highlighting this exponential scaling. The entire process is referred to as the parametric amplification of JPPs driven by the apical oxygen phonon. To investigate the dynamics of the coupled JPPs, which are symmetry-odd modes, time-resolved second harmonic generation experiments were conducted on optically driven $\text{YBa}_2\text{Cu}_3\text{O}_{6.48}$.

4.2.2 Time-resolved second harmonic generation

Symmetry-odd collective modes break the inversion symmetry of the crystal twice in one oscillating period. Besides the infrared-active phonons discussed above, Josephson plasmons are also symmetry-odd. Here, we introduce the probing technique of time-resolved second harmonic generation to detect the coherent oscillations of such modes.

We start with a brief introduction of nonlinear optics. When an intense optical short pulse is applied to a crystal, the induced polarization can be derived as a power series of the electric field

$$P = \chi^{(1)} E + \chi^{(2)} E^2 + \chi^{(3)} E^3 + \dots \quad (4.21)$$

where the first term corresponds to linear optics, and the last two terms describe the nonlinear contribution to the polarization which does not scale linearly with the electric field. The $\chi^{(2)}$ and $\chi^{(3)}$ are the second- and third-order susceptibilities.

The second-order nonlinear optics $P^{(2)} = \chi^{(2)}E^2$ describes the interaction of two electric fields, $E(\omega_1)$ and $E(\omega_2)$, with the material. The induced second-order polarization $P^{(2)}$ contains the mixing frequencies $\omega_1 \pm \omega_2$ and emits a new light field at these frequencies. Second harmonic generation (SHG) is a special case of this process, where two identical fields $E(\omega)$ interact with material, generating a frequency-doubled field $E(2\omega)$. In experiments, we can send an 800 nm probe pulse to the sample and detect the reflected probe pulse only in the 400 nm wavelength range. Importantly, this second-order nonlinear process is only allowed in media with broken inversion symmetry. For centrosymmetric materials like $\text{YBa}_2\text{Cu}_3\text{O}_{6.48}$, the second-order susceptibility $\chi^{(2)}$ is zero under the electric dipole approximation.

In contrast, the third-order nonlinear process $P^{(3)} = \chi^{(3)}E^3$ describes the interaction of three electric fields with the materials. The resulting photon is emitted at the mixing frequency of the three input fields. Unlike the second-order process, the third-order process is allowed in all kinds of materials, regardless of symmetry.

Next, we introduce the Hyper-Raman scattering which allows one to detect symmetry odd collective modes in a material. While Raman scattering is a process, in which phonon modes modulate the linear susceptibility $\chi^{(1)}$, Hyper-Raman scattering involves phonon modes that modulate the second-order susceptibility $\chi^{(2)}$. In general, all the infrared-active phonons are Hyper-Raman-active. We can expand the second-order nonlinear polarization into a Taylor series with respect to the coordinate of an infrared-active mode Q_{IR} . The Eq. (4.10) then reads

$$P = \chi^{(2)}E_i^2 + \frac{\partial\chi^{(2)}}{\partial Q_{IR}}Q_{IR}E_i^2 + \dots \quad (4.22)$$

where the first term is the static SHG of a material, and the second term is the Hyper-Raman scattering, which radiates the frequency-shifted SHG fields at $2\omega \pm \omega_{IR}$. It is important to note that in centrosymmetric media Hyper-Raman scattering is still

allowed even if the static SHG is forbidden.

To derive the time delay dependent SHG intensity for detecting coherent infrared phonons (or odd modes), we follow the same procedure presented in Section 4.1.2. By rewriting Eq. (4.16), the intensity of the emerging SHG probe field can be expressed as

$$I(\Delta t) = I_{SHG} + \cos(\omega_{IR}\Delta t)I_{hetero} + \cos(2\omega_{IR}\Delta t)I_{homo} \quad (4.23)$$

where I_{SHG} includes the intensity of the static SHG field $E_i(2\omega)$ and the two shifted SHG fields $E_i(2\omega \pm \omega_{IR})$, I_{hetero} results from the spectral overlap between $E_i(2\omega)$ and $E_i(2\omega \pm \omega_{IR})$, and I_{homo} represents the spectral overlap between $E_i(2\omega + \omega_{IR})$ and $E_i(2\omega - \omega_{IR})$.

If the sample crystal is centrosymmetric, the static SHG field vanishes $E_i(2\omega) = 0$, meaning that I_{SHG} only consists of the intensities of $E_i(2\omega \pm \omega_{IR})$ and the heterodyne component vanishes $I_{hetero} = 0$. The measurements only detect the homodyne component, in which the measured coherent oscillation show up at twice the natural frequencies of the infrared-active mode. In order to enable the heterodyne detection, interference with the static SHG field $E_i(2\omega)$ is required and the coherent mode oscillations modulate the detected I_{SHG} with one time of the natural mode frequency. If there is no static SHG field from the sample, the heterodyne interference can be realized by an externally applied source of SHG, referred to as the local oscillator.

4.2.3 Parametric amplification of Josephson plasmons

Time-resolved THz reflectivity measurements have revealed transient superconducting-like features in optically driven $\text{YBa}_2\text{Cu}_3\text{O}_{6.48}$. The $1/\omega$ divergence in $\sigma_2(\omega)$ indicates the presence of superfluid, and the THz reflectivity displays a plasma edge caused by the interlayer supercurrent tunneling [15–17, 21, 23]. The underlying physics of light-induced superconductivity was investigated through time-resolved SHG experiments, studying the coherent couplings between driven phonons and JPPs [22]. Figure 4.6 depicts the experimental setup. A mid-IR pump pulse resonantly drives

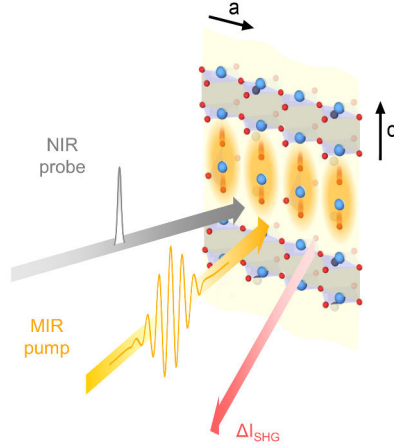


Figure 4.6: Schematic of time-resolved optical reflectivity spectroscopy. The mid-IR pump pulse (yellow) resonantly drives infrared-active c-axis apical oxygen phonons in $\text{YBa}_2\text{Cu}_3\text{O}_{6.48}$. Near-infrared probe pulses (gray) were detected in reflection geometry. Red arrow represents intensity changes at the second harmonic frequency (ΔI_{SHG}).

the 20-THz and 17-THz infrared phonons. A 800-nm probe pulse is directed to the $\text{YBa}_2\text{Cu}_3\text{O}_{6.48}$ samples, and the reflected probe pulse is filtered, isolating the 400-nm SHG signals ΔI_{SHG} .

Representative SHG data taken at the pump field strength of 0.3, 0.5, and 7 MV/cm are shown in Figs. 4.7a–4.7f, respectively. The oscillatory responses include contributions from all the driven and coupled coherent odd modes. In the Fourier spectrum of the low excitation field measurements as shown in Fig. 4.7b, two resonantly driven apical oxygen infrared phonons at 17 and 20 THz were observed. As the excitation field increases a peak at 2.5 THz emerges in the Fourier spectra (Figs. 4.7d and 4.7f) and was nonlinearly amplified. The amplitude of the 2.5 THz peak for 7 MV/cm pump field is nearly 100 times greater than the peak amplitude for 500 kV/cm pump field. A similar trend was also observed in $\text{YBa}_2\text{Cu}_3\text{O}_{6.65}$, where the low-frequency mode oscillates at 2.8 THz instead.

Additional resonances appear in the Fourier spectrum for the highest excitation field (Fig. 4.7f), which include two amplified phonon modes at 8.6 and 10.5 THz, along with a broad peak centered at 14.5 THz. According to the model discussed in Section 4.2.1, the 2.5 THz and 14.5 THz modes correspond to inter- and intra-

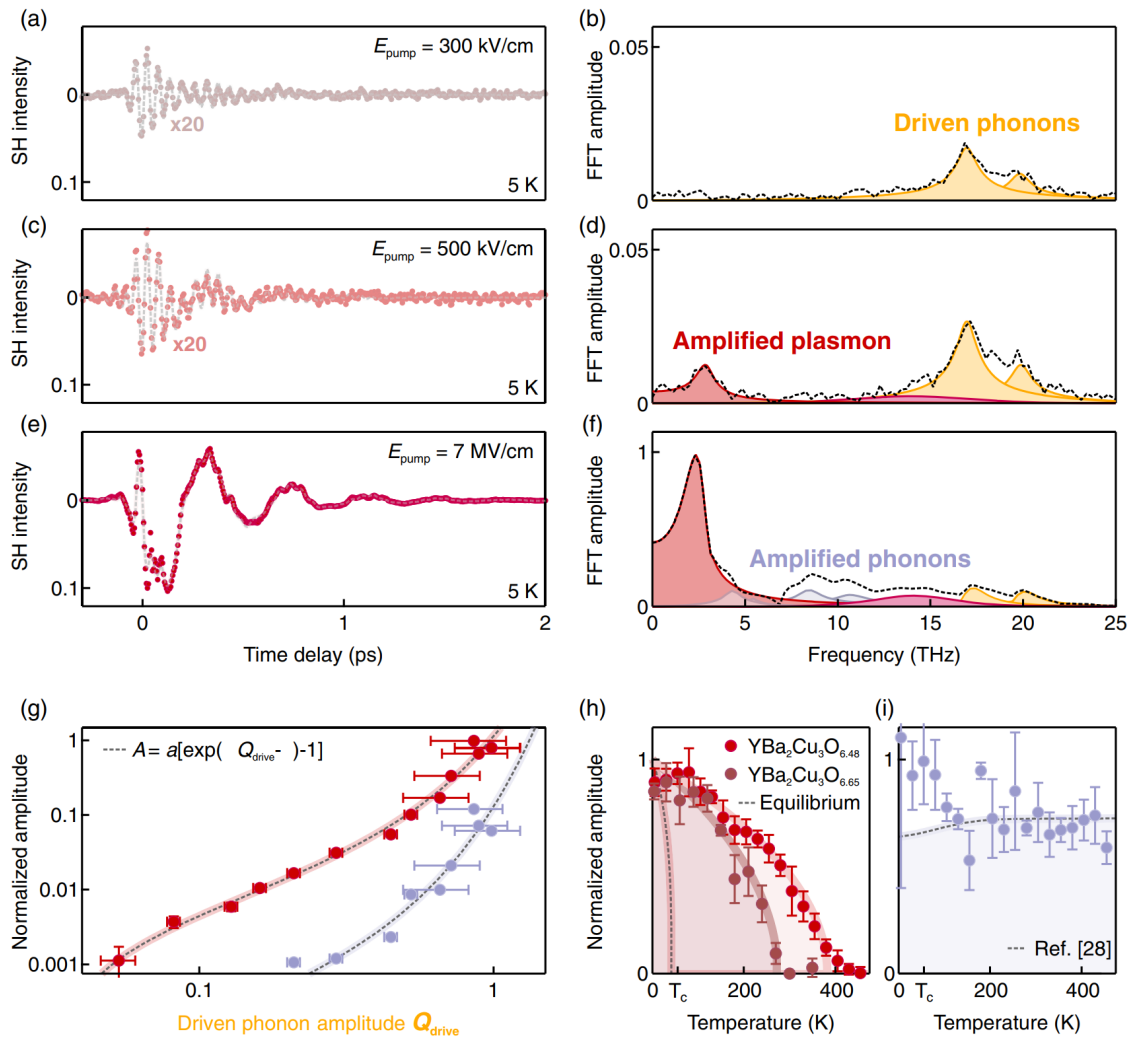


Figure 4.7: (a)-(f) Coherent SH signal at the excitation field of $E = 0.3, 0.5,$ and 7 MV/cm and the corresponding Fourier spectra at $T = 5$ K. The high-frequency oscillations at 17 and 20 THz (yellow peaks) are coherent apical oxygen vibrations, resonantly driven by the excitation pulse. The peaks at $\nu_1 = 2.5$ THz and $\nu_2 = 14.5$ THz (red and magenta) are ascribed to coherent oscillations of Josephson plasma waves. Additional peaks (gray) are dominated by those at 8.6 and 10.5 THz and label additional phonons nonlinearly coupled to the resonantly driven lattice modes. (g) Measured amplitude of the low-frequency JPP J_1 and the amplified phonon $Q_{\text{amplified}}$ plotted as a function of the driven phonon amplitude Q_{drive} . The dashed line is an exponential fit $A(Q_{\text{drive}}) = a(e^{\alpha Q_{\text{drive}}^{-\beta}} - 1)$ to the data, where α is the gain factor and $\beta > 0$ is the amplification threshold. (h) Full temperature dependence of the JPP peaks for $\text{YBa}_2\text{Cu}_3\text{O}_{6.48}$ (red) and $\text{YBa}_2\text{Cu}_3\text{O}_{6.65}$ (dark red). The lines are fits to the data $\propto \sqrt{1 - T/T'}$, yielding $T' = 380$ K for $\text{YBa}_2\text{Cu}_3\text{O}_{6.48}$ and $T' = 280$ K for $\text{YBa}_2\text{Cu}_3\text{O}_{6.65}$. The dashed line is the temperature dependence of the equilibrium low-frequency Josephson plasma resonance in $\text{YBa}_2\text{Cu}_3\text{O}_{6.48}$, which disappears at T_c . (i) Temperature dependence of the amplitude of the nonlinearly coupled phonons at 8.5 and 10 THz. Their temperature dependence from equilibrium infrared measurements in $\text{YBa}_2\text{Cu}_3\text{O}_{6.48}$ is shown as a dashed line. The data in (h) and (i) were recorded at an excitation peak field of 7 MV/cm. This figure is reprinted from Ref. [22].

bilayer JPP modes at finite in-plane momentum, respectively. To investigate how the driven phonon nonlinearly amplifies the JPPs, we used the amplitude of the 17 THz mode as the driven phonon $Q_{drive} \propto \Delta I_{SHG}(t)_{\omega=17THz}$, and the amplitude of 2.5 THz mode as lower JPP $J_1 \propto \Delta I_{SHG}(t)_{\omega=2.5THz}$. Figure 4.7g depicts the amplitude relation between the driven phonon and lower JPP, showing that the low JPP was amplified by at least three orders of magnitude as the driven phonon increased by a factor of 10. The exponential growth matches the theoretical prediction from Section 4.2.1.

Figure 4.7h shows the temperature dependence of the lower JPP mode for the two distinct doping level of $YBa_2Cu_3O_{6.48}$. Remarkably, the lower JPP mode persists beyond at the superconducting transition temperature T_c . The 2.5 THz mode in $YBa_2Cu_3O_{6.48}$ vanishes at 280 K, while the 2.8 THz mode in $YBa_2Cu_3O_{6.65}$ disappears at 380 K. These characteristic temperatures T' were determined by fitting the temperature dependence with a function proportional to $\sqrt{1 - T/T'}$. These values align closely with the corresponding pseudogap temperature T^* . This observation resembles the temperature dependence of Josephson plasma edge in the THz reflectivity measurements. It reinforces the hypothesis that driven phonons stabilize the phase fluctuation of pre-formed Cooper pairs, leading to transient superconductivity at high temperatures.

These experimental results support the three-mode mixing model, where the driven phonon couples directly to a pair of lower and upper JPPs at finite momentum. However, a more recent study using two-dimensional SHG spectroscopy on optically driven $YBa_2Cu_3O_{6.48}$ [26] further explored the origin of the 2.5 THz mode. This led to the proposal of a modified four-mode mixing model to more accurately describe the coherent phonon-plasmon coupling. Both studies (Refs. [22] and [26]) concluded that the amplified JPP is coherently driven by apical oxygen phonons, suggesting that light-induced superconductivity in $YBa_2Cu_3O_{6.48}$ is a coherent phenomenon.

In conclusion, this chapter discusses the all the coherent couplings in the optical

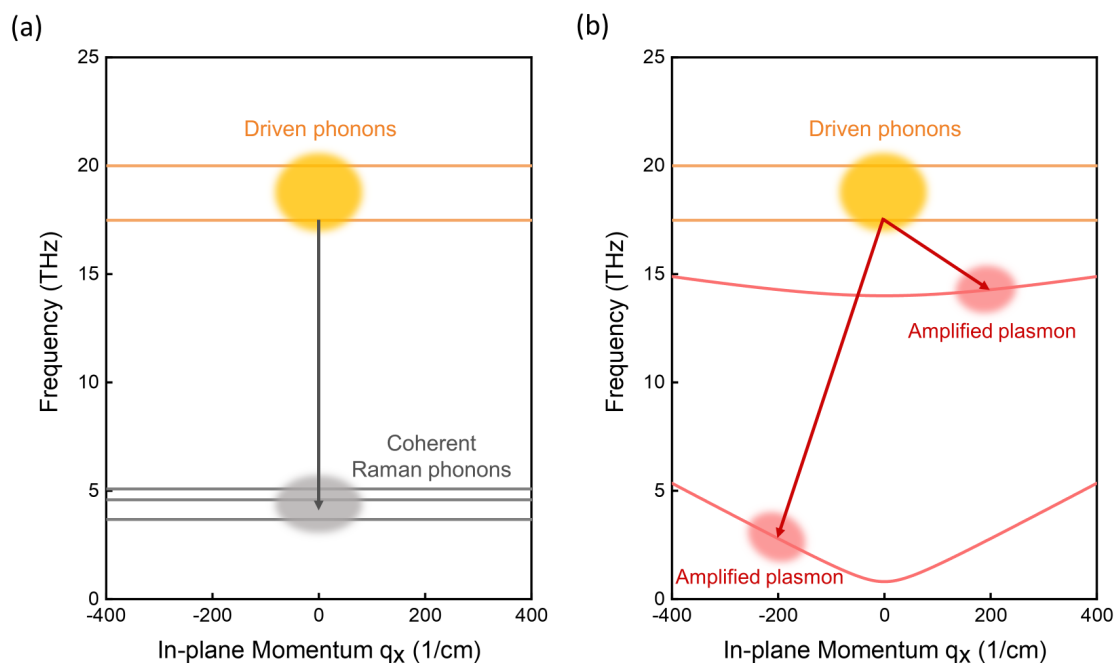


Figure 4.8: (a) Frequency-momentum diagram showing the dispersion curves of driven infrared phonons (orange) and Raman phonons (light gray). The dark gray arrow shows the coupling pathway of stimulated ionic Raman processes between the driven phonons and Raman phonons. (b) Frequency-momentum diagram showing the dispersion curves of driven infrared phonons (orange) and Josephson plasmons (light red). The dark red arrows indicate instead the three-mode mixing process between driven phonons and Josephson plasmons. This figure is adapted from Ref. [24]

driven $\text{YBa}_2\text{Cu}_3\text{O}_{6.48}$. Figure 4.8 summarizes the current understanding of these coherent couplings. The driven infrared phonons couple to a number of Raman phonons through the stimulated ionic Raman scattering, leading to a transient crystal structure that favours the superconductivity. Simultaneously, the driven infrared phonons directly couple to the Josephson plasmons through multi-mode mixing process, which enhance the superconducting coherence in $\text{YBa}_2\text{Cu}_3\text{O}_{6.48}$. In the next chapter, I will turn to the dynamics of incoherent carriers, including quasiparticles and phonons, that occurs in parallel to the coherent superfluid dynamics.

Chapter 5

Incoherent couplings in optically-driven $\text{YBa}_2\text{Cu}_3\text{O}_{6.48}$

In this chapter, I will discuss the incoherent energy transfer processes in optically driven $\text{YBa}_2\text{Cu}_3\text{O}_{6.48}$. Firstly, the mid-IR excitation pulses, tuned to be resonant with the apical oxygen phonons, not only drive them coherently but also excite charge carriers, which can transfer their excess energy to other modes of the system such as lower-energy phonons, spin, or plasma. Secondly, one expects that the coherently driven phonons will also decay into incoherent vibrational modes through spontaneous ionic Raman processes, which will raise the temperatures of different low-energy degrees of freedom. Figure 5.1a depicts the energy flow from the excitation to hot phonons in a frequency-momentum diagram, while Figure 5.1b depicts schematically the expected quasiparticle heating, represented by the corresponding electron density of states (eDOS) and population $n(E)$.

In the following Sections, I will describe how we could determine the transient quasiparticle temperatures from time-resolved THz reflectivity measurements, and measure the phonon temperatures from time-resolved Raman thermometry, which is the main focus of this thesis. These temperature changes provide quantitative information on the nature of the optically-driven superconducting state and its decay.

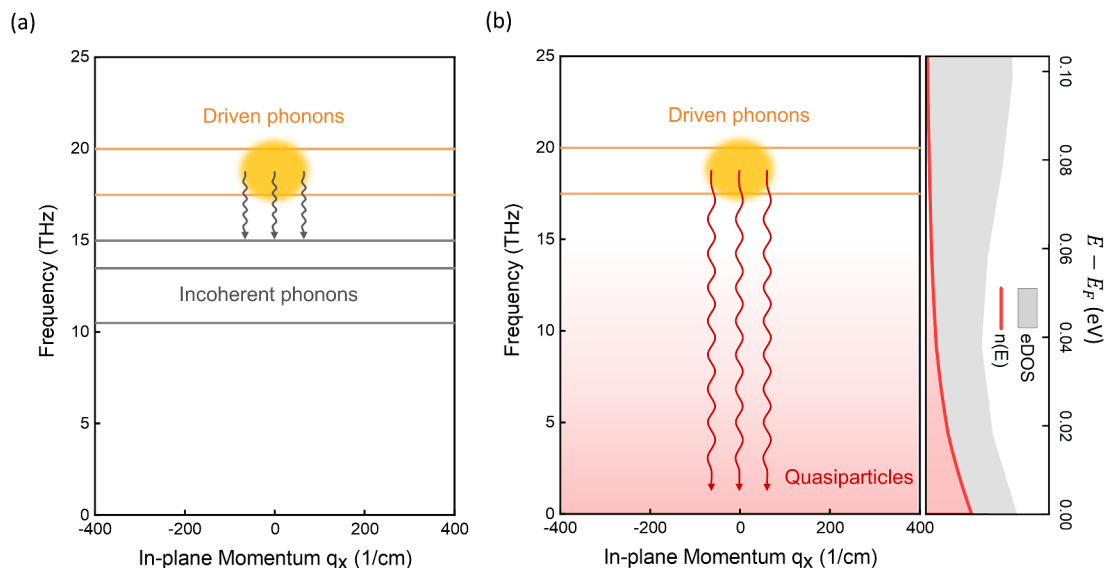


Figure 5.1: (a) Frequency-momentum diagram with the dispersion curves of resonantly driven infrared phonons (orange), and incoherent Raman phonons at 10.5, 13.5, and 15 THz (light gray). The wiggling arrows indicate the incoherent energy transfer to Raman phonons (dark gray) (b) Left panel: Frequency-momentum diagram with the dispersion curves of resonantly driven infrared phonons (orange). The red gradient background represents the electron distribution above the Fermi energy, which is set to zero frequency in this diagram. The wiggling arrows indicate the incoherent energy transfer to quasiparticles (dark red). Right panel: Electron density of state eDOS (gray) and population $n(E)$ (red). The former was obtained by ab-initio calculations, while the latter was calculated by multiplying the eDOS with a Fermi-Dirac distribution at $T = 100$ K. This figure is adapted from Ref. [24]

5.1 Dissipative response of hot quasiparticles

Along the crystal c -axis, $\text{YBa}_2\text{Cu}_3\text{O}_{6.48}$ in its normal state behaves like a semiconductor because carrier hopping across the CuO_2 planes is limited by the insulating layers. When the temperature increases, thermal excitation enhances the probability of interlayer tunneling, thus increasing the overall c -axis conductivity. This effect is revealed in the equilibrium spectra as shown in Fig. 5.2a, where the real part of the optical conductivity, $\sigma_1(\omega)$, increases as the temperature becomes higher.

As discussed in Section 2.3, the electronic contribution to the c -axis THz-frequency optical conductivity in $\text{YBa}_2\text{Cu}_3\text{O}_{6.48}$ can be modeled by an overdamped Drude re-

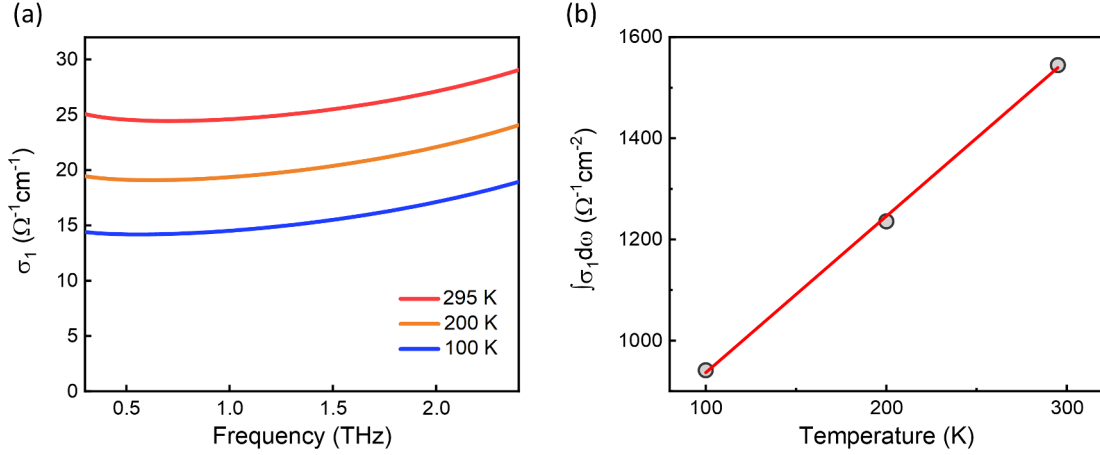


Figure 5.2: (a) Real part of the c-axis optical conductivity, $\sigma_1(\omega)$, of $\text{YBa}_2\text{Cu}_3\text{O}_{6.48}$ measured in equilibrium condition at the temperatures of 100, 200, and 295 K. (b) The relation of the integrated spectral weight $\int_{0.6\text{THz}}^{2.25\text{THz}} \sigma_1(\omega) d\omega$ to the temperature.

sponse for quasiparticles. The real part of optical conductivity is given by

$$\sigma_1(\omega) = \frac{n_n e^2}{m^*} \frac{\gamma}{\gamma^2 + \omega^2} \quad (5.1)$$

where n_n is the carrier density, m^* is the effective mass, and γ is the scattering rate. The latter typically takes values of several tens of THz and above, reflecting the incoherent and “overdamped” nature of the out-of-plane Drude response.

In the following we will use the integral of $\sigma_1(\omega)$ in a given frequency range, i.e. the optical spectral weight, to quantify the strength of quasiparticle tunneling across the Cu-O planes. One of the effects of optical excitation in our experiment is to promote interlayer tunneling of quasiparticles on ultrafast time scales, resulting in a transient increase in the real part of the c-axis optical conductivity. We describe this process as an effective temperature rise of the quasiparticles.

Here, we utilized the c-axis optical conductivity to estimate the transient temperature of the electronic subsystem when subjected to mid-IR excitation. We calculate the integral of $\sigma_1(\omega)$ between 0.6 and 2.25 THz, $\int_{0.6\text{THz}}^{2.25\text{THz}} \sigma_1(\omega) d\omega$, as a figure of merit. The integrated $\sigma_1(\omega)$ spectral weight in equilibrium exhibits a linear dependence to the temperature in the range of 100 to 300 K as depicted in Fig. 5.2b. This linear dependence will enable us to estimate the temperatures of the

quasiparticles. According to the data reported in Ref. [23], we tracked the transient $\sigma_1(\omega)$ conductivity spectra after the mid-IR excitation and calculated the integrated spectral weight, $\int_{0.6THz}^{2.25THz} \sigma_1(\omega) d\omega$, for each time delay. These values were converted to “equivalent temperatures” of the quasiparticles using the linear relation shown in Fig. 5.2b. This approach was possible because the frequency-dependent $\sigma_1(\omega)$ measured throughout the light-induced dynamics closely resembled the same quantity measured at equilibrium at different temperatures.

Figure 5.3 shows the time evolution of these transient spectral weights and the corresponding temperatures. The temperatures of quasiparticles increase from the base temperature 100 K to 300 or 200 K, depending on the linear model or square-root model used to extract the optical properties (see Section 3.1), and decay back to the equilibrium temperature in about 5-10 picoseconds. Although this estimate is by no means a precise measurement of the non-equilibrium quasiparticle temperature, it provides a useful point of reference.

5.2 Spectator mode of hot incoherent phonons

The energy from the excitation light pulse not only transfers to the electronic system but also to the lattice, generating hot incoherent phonons. Unlike coherent phonons, which oscillate with a synchronized phase, incoherent phonons have random phases and directions. “Hot” incoherent phonons refer to specific phonon modes that, upon photo-excitation, become overpopulated and exhibit higher occupation numbers than those expected in thermal equilibrium. As a result, these phonons have an effective temperature that is higher than the lattice temperature. When an mid-IR optical pulse drives $YBa_2Cu_3O_{6.48}$, it generates the coherent phonons and the hot quasiparticles. Both can transfer the energy to the incoherent phonons through spontaneous ionic Raman scattering and electron-phonon couplings, respectively. Finally, the hot incoherent phonons dissipate the energy throughout the lattice, leading to an overall increase in lattice temperature.

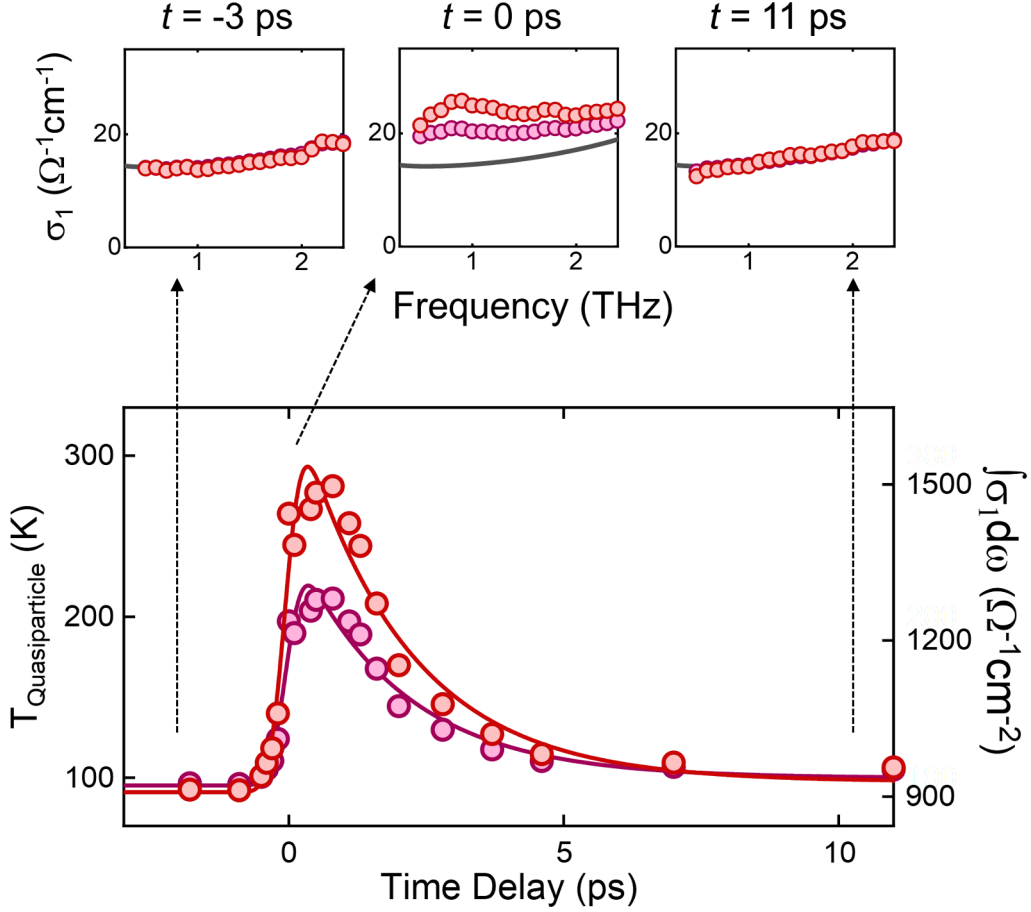


Figure 5.3: Top panel: Real part of the c -axis optical conductivity, $\sigma_1(\omega)$, of $\text{YBa}_2\text{Cu}_3\text{O}_{6.48}$ measured upon mid-IR excitation at time delays of $t = -3, 0,$ and $+11$ ps. In each panel, gray line and red circles represent the equilibrium and transient $\sigma_1(\omega)$ at $T = 100$ K, respectively. The latter was calculated from the data of Ref. [23] with two different models, one based on a linear dependence (red) and another one based on a square root dependence (purple) of the photoinduced response on the pump fluence [47,48]. Bottom panel: Equivalent quasi-particle temperature as a function of time delay (colored circles), determined from the integrated spectral weight $\int_{0.6\text{THz}}^{2.25\text{THz}} \sigma_1(\omega) d\omega$ (see right axis). Red and purple circles refer to the linear model and square root model, respectively, with the same color coding as top panel. Full lines are fits with an error function and an exponential decay. This figure is reprinted from Ref. [24]

While the dynamics of coherent phonons and hot quasiparticles have been discussed in Sections 4.1 and 5.1, respectively, the behavior of hot incoherent phonons has remained an open question in optically driven $\text{YBa}_2\text{Cu}_3\text{O}_{6.48}$. To investigate this phenomenon, we conducted spontaneous time-resolved Raman scattering experiments, which are able to directly probe phonon populations and determine the phonon temperatures. However, in our experiments, we can only measure the temperature of one Raman mode to represent the overall behavior of hot incoherent phonons, assuming that these phonons exhibit comparable peak temperatures and thermalization times.

Here, it is important to note that the increase in phonon temperature measured via spontaneous Raman scattering can in general arise not only from incoherent energy transfer processes but also from coherent phonon driving. If one Raman mode is coherently driven, for example through the cubic phononic coupling or impulsive stimulated Raman scattering, this will introduce additional phonon populations of this Raman mode. Therefore, to study the temperature of pure incoherent phonons, it is crucial to ensure that the Raman mode we measured is not influenced by coherent driving. This allows the mode to act as a 'spectator', reflecting the overall behavior of the hot incoherent phonons.

We follow the cubic phononic coupling described in Section 4.1.1 and solve Eq. (4.7) and Eq. (4.8) under two different conditions. The first case, depicted in Fig. 5.4a, shows the coupling between a 20 THz infrared phonon and a 5 THz Raman phonon. The Raman mode is displaced due to the directional force of $a_{21}Q_{IR}^2$ and undergoes coherent oscillation at its natural frequency ω_R . In another case, the same 20 THz infrared phonon couples to a 15 THz Raman phonon. As presented in Fig. 5.4b, the Raman mode is displaced following the envelope of Q_{IR}^2 and, however, no coherent oscillation is observed. This is because the coherent oscillation can only occur when the prompt rise of directional force is faster or comparable to the period of the Raman mode. The rise time of the Q_{IR}^2 force is determined by the time duration of the mid-IR excitation pulse and the damping rate of the driven infrared

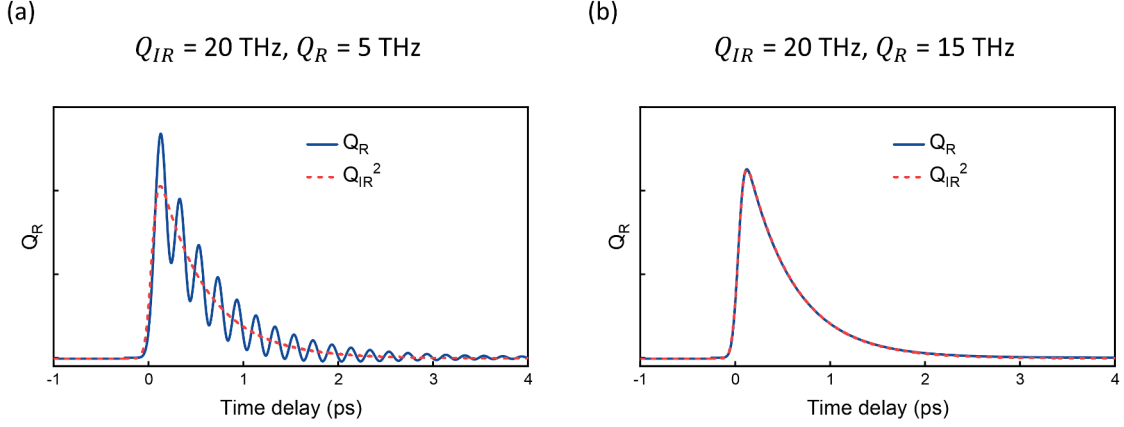


Figure 5.4: Simulation results of the dynamical response of Raman-active phonon modes Q_R . The infrared-active mode Q_{IR} is resonantly driven by a 150-fs Gaussian pulse. With cubic phononic coupling, a directional force of Q_{IR}^2 is exerted on the coupled Raman mode Q_R . Figure (a) illustrates the simulation result of 20 THz driven mode coupling to 5 THz Raman mode, while (b) depict the result of coupling to 15 THz Raman mode.

mode. Therefore, when considering a Raman mode as a spectator phonon mode, it is crucial to select one with a frequency high enough to prevent coherent excitation. In our experiments, the driven phonon in $\text{YBa}_2\text{Cu}_3\text{O}_{6.48}$ is the apical oxygen B_{1u} infrared phonon with the natural frequency of 20 THz. The measured spectator mode is the apical oxygen A_{1g} Raman phonon with the natural frequency of 15 THz. The atomic motion of this Raman mode is illustrated in Fig. 5.5. The motion of the A_{1g} mode differs from that of the B_{1u} mode: in the A_{1g} mode, two apical oxygen atoms oscillate along the c-axis of $\text{YBa}_2\text{Cu}_3\text{O}_{6.48}$ in opposite directions, while in the B_{1u} mode, two apical oxygen atoms oscillate with the same direction.

5.3 Time-resolved Raman thermometry

5.3.1 Theory of Raman scattering

When monochromatic light with energy $\hbar\omega_0$ interacts with a material, it undergoes various light scattering processes. Most of the photons are elastically scattered, maintaining the energy $\hbar\omega_0$ of the incident light. This phenomenon is known as Rayleigh scattering. However, a small fraction of the photons undergo an inelastic

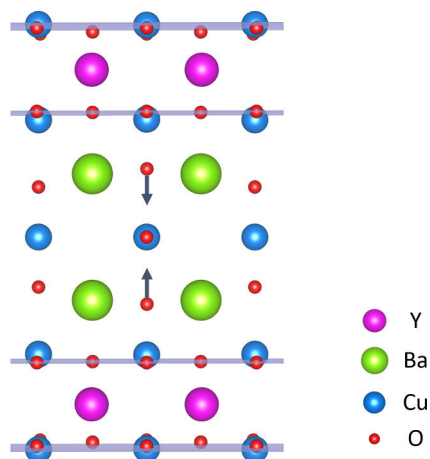


Figure 5.5: Schematic of atomic motion of 15-THz apical oxygen Raman mode in $\text{YBa}_2\text{Cu}_3\text{O}_{6.48}$.

scattering process called Raman scattering, where some energy $\hbar\omega_s$ of the incident light is transferred to or taken from an elementary excitation of the system, resulting in scattered photons with energy $\hbar\omega_0 \pm \hbar\omega_s$. For example, the energy shift $\hbar\omega_s$ corresponds to the energy of Raman-active phonons of the material.

Raman scattering can be classified into two types, Stokes and Anti-Stokes scatterings. In Stokes Raman scattering, the material is excited by the incident photon $\hbar\omega_0$ from the ground vibrational state to a higher-energy state (can be a virtual state or a real state), and returns down to the excited vibrational state by emitting a photon with lower energy $\hbar\omega_0 - \hbar\omega_s$. On the contrary, in Anti-Stokes Raman scattering, the energy transition starts from the excited vibrational state to a higher-energy state, and relaxes back to the ground vibrational state. Here, the incident photon gains the energy from the material and scatters at a higher energy $\hbar\omega_0 + \hbar\omega_s$. This process requires thermal population of the vibrational state at equilibrium. Figure 5.6 shows an energy level diagram of the two scattering processes. The intensities of Stokes and Anti-Stokes peaks are related to the phonon populations at the ground state and the first excited state. In thermal equilibrium, phonons in the ground state are higher populated than the first excited state. Hence, the Stokes peaks are much stronger than Anti-Stokes peaks and their intensity ratio depends on the

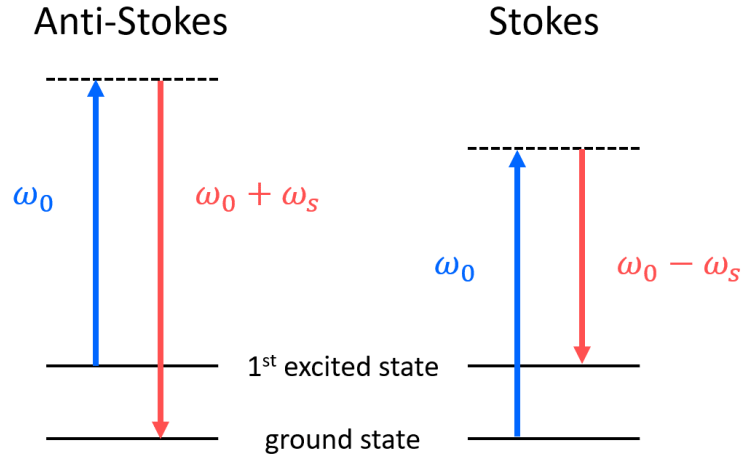


Figure 5.6: Energy level diagram of Anti-Stokes and Stokes Raman scattering processes.

temperature of the material.

In the following, we employ the classical theory of electromagnetic radiation to explain the light scattering processes. The electric field of incident light is

$$E = E_0 \cos(\omega_0 t) \quad (5.2)$$

where E_0 and ω_0 are the amplitude and the frequency of the incident electromagnetic wave. When the light interacts with the material, the induced polarization can be expressed as

$$P = \alpha E \quad (5.3)$$

where α is the polarizability tensor. The induced polarization will emit radiation, which is the scattered light. To derive the total power of the scattered light, we treat the polarization P as a Hertzian dipole oscillating at the frequency ω_0 . The time-averaged power of the radiation emitted by this Hertzian dipole can be expressed using Larmor's formula.

$$W = \frac{1}{6\pi\epsilon_0 c^3} \left| \frac{d^2 P}{dt^2} \right|^2 = \frac{\omega_0^4}{12\pi\epsilon_0 c^3} |\alpha_0|^2 E_0^2 \quad (5.4)$$

Here, we have considered that the time average of the cosine function is $\frac{1}{2}$. This expression indicates the total power of Rayleigh scattering under the assumption that the polarizability is a constant $\alpha = \alpha_0$. Now we consider the case where the

polarizability is modulated by a crystal lattice vibrations. To formalize this, we expand α into a Taylor series according to the displacement of the atoms along normal coordinate Q .

$$\alpha = \alpha_0 + \frac{\partial\alpha}{\partial Q}Q + \frac{1}{2}\frac{\partial^2\alpha}{\partial Q^2}Q^2 + \dots \quad (5.5)$$

Here we assume that the normal mode Q has a simple harmonic motion with a oscillating frequency ω_q .

$$Q = Q_0 \cos(\omega_q t) \quad (5.6)$$

The polarization of the system can be rewritten as

$$P = \alpha_0 E_0 \cos(\omega_0 t) + \frac{\partial\alpha}{\partial Q} Q_0 \cos(\omega_q t) E_0 \cos(\omega_0 t) + \dots \quad (5.7)$$

Using the trigonometric formula for the products of two cosine functions, we obtain

$$\begin{aligned} P &= \alpha_0 E_0 \cos(\omega_0 t) + \frac{1}{2} \frac{\partial\alpha}{\partial Q} Q_0 E_0 \cos[(\omega_0 - \omega_q)t] + \frac{1}{2} \frac{\partial\alpha}{\partial Q} Q_0 E_0 \cos[(\omega_0 + \omega_q)t] + \dots \\ &= P_{Rayleigh} + P_{Stokes} + P_{AntiStokes} + \dots \end{aligned} \quad (5.8)$$

The scattered light emitted from the oscillating polarization has three different frequency components ω_0 , $\omega_0 - \omega_q$, and $\omega_0 + \omega_q$, corresponding to Rayleigh scattering, Stokes Raman scattering, and Anti-Stokes Raman scattering, respectively. We again utilize Eq. (5.4) with the Stokes polarization P_{Stokes} to derive the power of the Stokes radiation.

$$W_S = \frac{1}{6\pi\epsilon_0 c^3} \left| \frac{d^2 P_{Stokes}}{dt^2} \right|^2 = \frac{(\omega_0 - \omega_q)^4}{48\pi\epsilon_0 c^3} \left(\frac{\partial\alpha}{\partial Q} \right)^2 Q_0^2 E_0^2 \quad (5.9)$$

For the Anti-Stokes radiation, the power is

$$W_{AS} = \frac{(\omega_0 + \omega_q)^4}{48\pi\epsilon_0 c^3} \left(\frac{\partial\alpha}{\partial Q} \right)^2 Q_0^2 E_0^2 \quad (5.10)$$

In the classical approach, the Stokes and Anti-Stokes have comparable scattering strengths, and their relation solely depends on the fourth power of the frequency. However, in the Raman experiments performed within this thesis, the intensity of

the Anti-Stokes signal is significantly smaller than that of the Stokes scattering. To accurately model this relation, a semi-classical approach is required [60–62].

We again consider the incident electric field $E_i = E_i \hat{e}_i$ at frequency ω_0 , which induces a dipole moment $P = \alpha E_i \hat{e}_i$ in the material. \hat{e}_i is the unit vector of the polarization of the incident light. We rewrite Eq. (5.4) in a general form. The total power of scattered light in all directions of space is then

$$W = \frac{\omega^4}{12\pi\epsilon_0 c^3} |\hat{e}_s \cdot P|^2 = \frac{\omega^4}{12\pi\epsilon_0 c^3} |\hat{e}_s \cdot \alpha \cdot \hat{e}_i|^2 E_i^2 \quad (5.11)$$

where \hat{e}_s is the unit vector of the polarization of scattered light. ω and α are variables depending on the type of scattering. To describe the Raman scattering process, the effect of the lattice vibration on the polarizability α is considered as demonstrated in Eq. (5.5). Here we express the displacement of the atom Q in the complex form.

$$Q = X e^{-i\omega_q t} + X^* e^{i\omega_q t} \quad (5.12)$$

The polarizability can again be expanded into a Taylor series according to X and X^*

$$\alpha = \alpha_0 + \frac{\partial\alpha}{\partial X} X e^{-i\omega_q t} + \frac{\partial\alpha}{\partial X^*} X^* e^{i\omega_q t} + \dots \quad (5.13)$$

By substituting Eq. (5.13) into Eq. (5.11), we obtain the total power of the Stokes radiation

$$W_S = \frac{(\omega_0 - \omega_q)^4}{12\pi\epsilon_0 c^3} \left| \hat{e}_s \cdot \frac{\partial\alpha}{\partial X} \cdot \hat{e}_i \right|^2 \langle X X^* \rangle E_i^2 \quad (5.14)$$

and the total power of the Anti-Stokes radiation.

$$W_{AS} = \frac{(\omega_0 + \omega_q)^4}{12\pi\epsilon_0 c^3} \left| \hat{e}_s \cdot \frac{\partial\alpha}{\partial X^*} \cdot \hat{e}_i \right|^2 \langle X^* X \rangle E_i^2 \quad (5.15)$$

To calculate the factors $\langle X X^* \rangle$ and $\langle X^* X \rangle$, we replace the displacement X and X^* by the creation and annihilation operators X and X^\dagger in quantum mechanics. Stokes Raman scattering involves creation of a quantum $\hbar\omega_q$ excitation in the material, hence the transition rate is proportional to $\langle X X^\dagger \rangle$. In contrast, Anti-Stokes Raman scattering is a process that annihilates a quantum $\hbar\omega_q$ excitation, meaning that

the transition rate is proportional to $\langle X^\dagger X \rangle$. Following the fluctuation-dissipation theory [60–62], we calculate these quantum mechanical factors to be

$$\langle X X^\dagger \rangle = \frac{\hbar}{2\omega_q} (n + 1) \quad (5.16)$$

$$\langle X^\dagger X \rangle = \frac{\hbar}{2\omega_q} (n) \quad (5.17)$$

where $n = \frac{1}{\exp(\hbar\omega_q/k_B T) - 1}$ is the occupation number of Bose-Einstein distribution. Substituting the quantum mechanical factors into Eq. (5.14) and Eq. (5.15), we obtain

$$W_S = \frac{\hbar(\omega_0 - \omega_q)^4}{24\omega_q\pi\epsilon_0 c^3} \left| \hat{e}_s \cdot \frac{\partial\alpha}{\partial X} \cdot \hat{e}_i \right|^2 (n + 1) E_i^2 \quad (5.18)$$

and

$$W_{AS} = \frac{\hbar(\omega_0 + \omega_q)^4}{24\omega_q\pi\epsilon_0 c^3} \left| \hat{e}_s \cdot \frac{\partial\alpha}{\partial X^*} \cdot \hat{e}_i \right|^2 (n) E_i^2. \quad (5.19)$$

If the frequency of incident light ω_0 is far away from the resonance of the material, the factor $|\hat{e}_s \cdot \frac{\partial\alpha}{\partial X} \cdot \hat{e}_i|$ is equal to $|\hat{e}_s \cdot \frac{\partial\alpha}{\partial X^*} \cdot \hat{e}_i|$. We can therefore obtain the relation between the intensities of Stokes and Anti-Stokes scatterings.

$$\frac{I_{AS}}{I_S} = \frac{(\omega_0 + \omega_q)^4}{(\omega_0 - \omega_q)^4} \frac{n}{n + 1} = \frac{(\omega_0 + \omega_q)^4}{(\omega_0 - \omega_q)^4} \exp\left(\frac{-\hbar\omega_q}{k_B T}\right) \quad (5.20)$$

The intensity ratio I_{AS}/I_S is experimentally detectable and can be used to determine the temperature of the material. In time-resolved experiments, we can measure the transient temperature of each Raman-active phonon mode [63–72]. Note that if one uses a photon counting detector instead of energy-based detector, the read-out signal strength is proportional to the total photon number rather than the total energy. Hence, this requires us to replace the quartic term to the cubic term [73]. Equation (5.20) becomes

$$\frac{I_{AS}}{I_S} = \frac{(\omega_0 + \omega_q)^3}{(\omega_0 - \omega_q)^3} \frac{n}{n + 1} = \frac{(\omega_0 + \omega_q)^3}{(\omega_0 - \omega_q)^3} \exp\left(\frac{-\hbar\omega_q}{k_B T}\right) \quad (5.21)$$

5.3.2 Experimental setup

Figure 5.7 depicts a schematic drawing of the time-resolved Raman thermometry setup used for the experiments presented here. A Ti:sapphire amplifier system delivering 100-fs pulses at 800-nm wavelength and 1-kHz repetition rate was used to

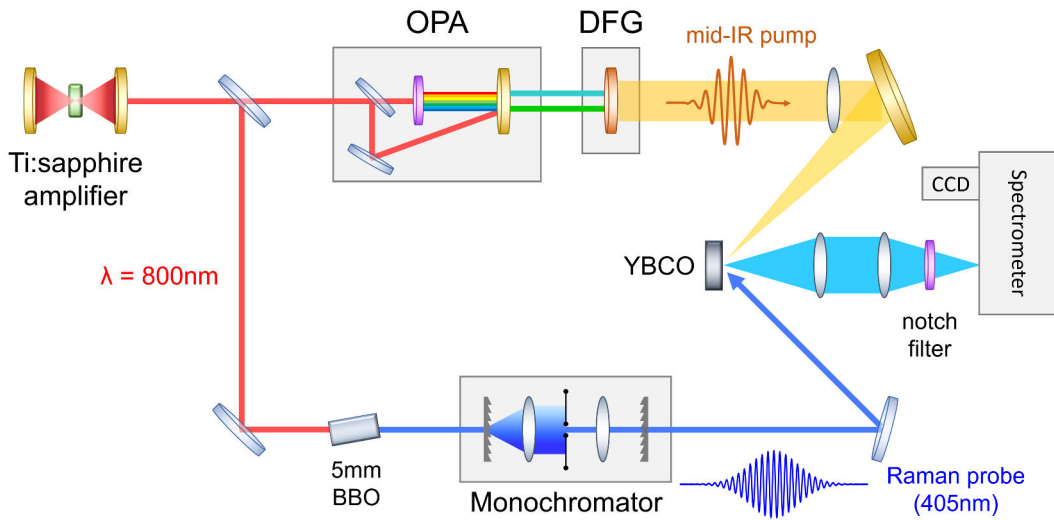


Figure 5.7: Schematic diagram of time-resolved Raman thermometry setup. This figure is reprinted from Ref. [24]

drive an optical parametric amplifier (OPA). The signal and idler outputs were directed into a 1 mm thick GaSe crystal to generate mid-IR pump pulses via difference frequency generation (DFG). The pump spectrum was centered at 20 THz with an 8-THz FWHM bandwidth to resonantly excite the two infrared-active c-axis polarized apical oxygen phonons of $\text{YBa}_2\text{Cu}_3\text{O}_{6.48}$ at 17.5 and 20 THz. The spectrum of the excitation pulses, measured via Fourier transform infrared spectroscopy (FTIR) is shown in Fig. 5.8. The pump pulses were focused onto the sample by a KBr lens, yielding an excitation fluence of 8 mJ/cm^2 . Note that the pump pulses were stretched by the dispersive effect of the KBr lens. A cross-correlation measurement between the mid-IR pump pulse and the 800-nm fundamental pulse, using sum frequency generation (SFG) in 10- μm thin LiNbO_3 (see Fig. 5.10a), yielded a 800 fs FWHM time duration. The time-resolved THz reflectivity measurements shown earlier in Figs. 3.9 and 5.3 were measured under the same excitation conditions.

For the Raman scattering experiment, 405-nm probe pulses were generated by second harmonic generation (SHG) from the 800-nm fundamental pulses in a tilted 5-mm thick BBO crystal. The resulting SHG spectrum was cleaned up by a 405-nm

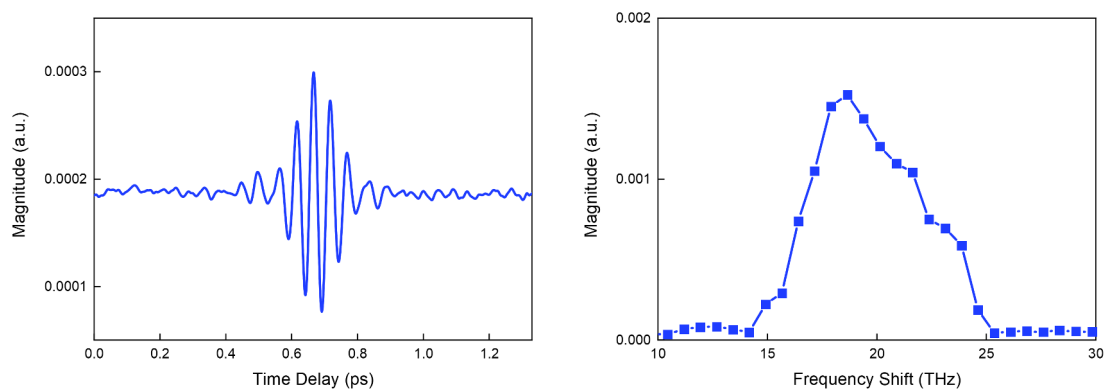


Figure 5.8: FTIR spectrum of the mid-IR pump pulse. The center frequency is 20 THz and the bandwidth is roughly 8 THz.

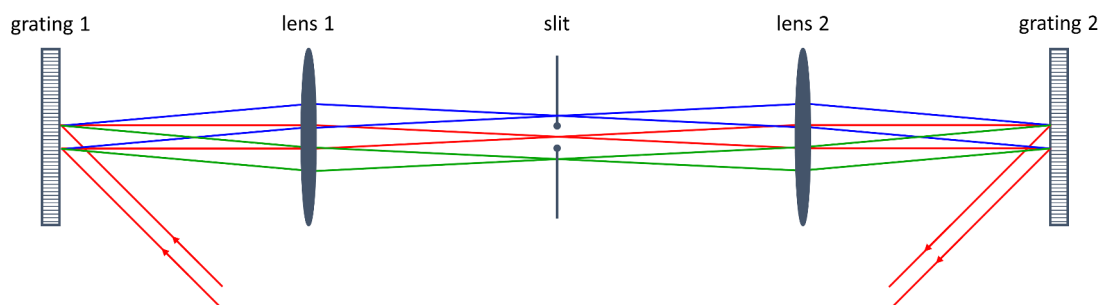


Figure 5.9: Schematic diagram of the home-built grating-based monochromator. The distances between grating 1 and lens 1, lens 1 and slit, slit and lens 2, lens and grating 2 were all equal to the focal length of lenses 1 and 2.

bandpass filter and a home-built grating-based monochromator. Figure 5.9 shows the design of this monochromator, which consists two gratings, two lenses, and a variable slit. The first grating and lens dispersed the probe beam and focused it onto the slit. The second grating and lens compensated for the resulting dispersion and combined the spatially separated wavelengths of the femtosecond pulses into one beam. The spectral bandwidth of the probe beam was controlled by changing the slit width. In this experiment, the bandwidth was reduced to about 3 THz FWHM, corresponding to 100 cm^{-1} . The time duration was 600 fs, obtained by a transient two-photon absorption measurement on a $10\text{-}\mu\text{m}$ LiNbO_3 , as shown in Fig. 5.10b. A cross-correlation measurement between the mid-IR pump and 405-nm probe pulses is shown in Fig. 5.10c. The time resolution for our Raman experiment is 1.1 ps FWHM.

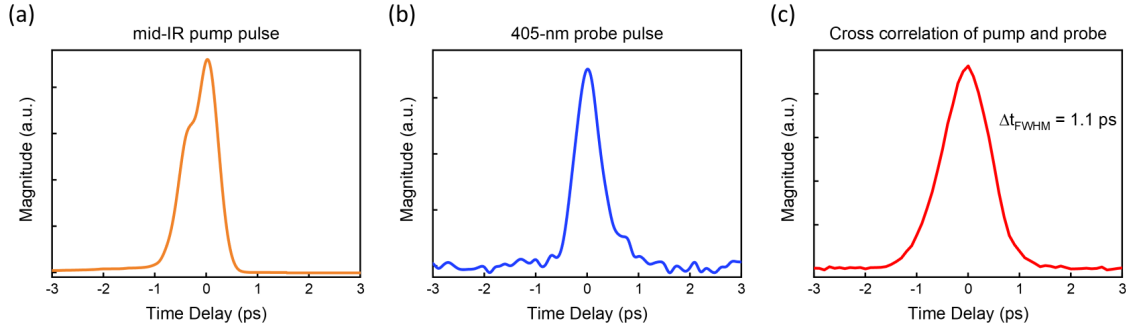


Figure 5.10: (a) Cross-correlation measurement of 800-nm and mid-IR pulses, using SFG from a 10- μm LiNbO₃. The data shows that the mid-IR pulses have 800 fs time duration. Since the 800-nm fundamental pulse has less than 100 fs duration, the data closely represents the time profile of mid-IR pump. (b) 800-nm pump 405-nm probe measurement on 10- μm LiNbO₃. LiNbO₃ does not show any additional response to 800 nm excitation. Hence, the two color pump probe measurement resembles the cross-correlation of 800-nm and 405-nm pulses. The data closely represents the time profile of 405-nm probe. (c) Cross-correlation measurement of 405-nm and mid-IR pulses, using SFG from the 10- μm LiNbO₃. The time resolution of our Raman setup is 1.1 ps.

In the time-resolved Raman thermometry experiments, both pump and probe pulses were polarized along the c -axis of an ac -oriented surface of a YBa₂Cu₃O_{6.48} single crystal. The probe photons scattered from the sample were collected by a pair of aspherical lenses, filtered by a c -axis oriented polarizer and detected by a 500-mm focal length spectrometer equipped with a thermoelectric-cooled CCD detector. A 405-nm commercial notch filter was used to block the strong elastic scattering.

5.4 Dynamics of hot incoherent phonons

5.4.1 Experimental results and data analysis

All the Raman spectra presented in this chapter were acquired in the $y(zz)\bar{y}$ geometry, that is two polarizers, placed before and after the sample, were aligned along the crystal c -axis of the YBa₂Cu₃O_{6.48} sample. In Figure 5.11, we show a set of Raman spectra measured at room temperature ($T = 295\text{K}$) for pump-probe time delays of -5, -2, -0.5, -0.2, 0.1, 0.4, 0.7, 4, and 10 ps. The pump and probe fluences were 8 and 1.35 mJ/cm², respectively. From the Raman spectra measured at negative time

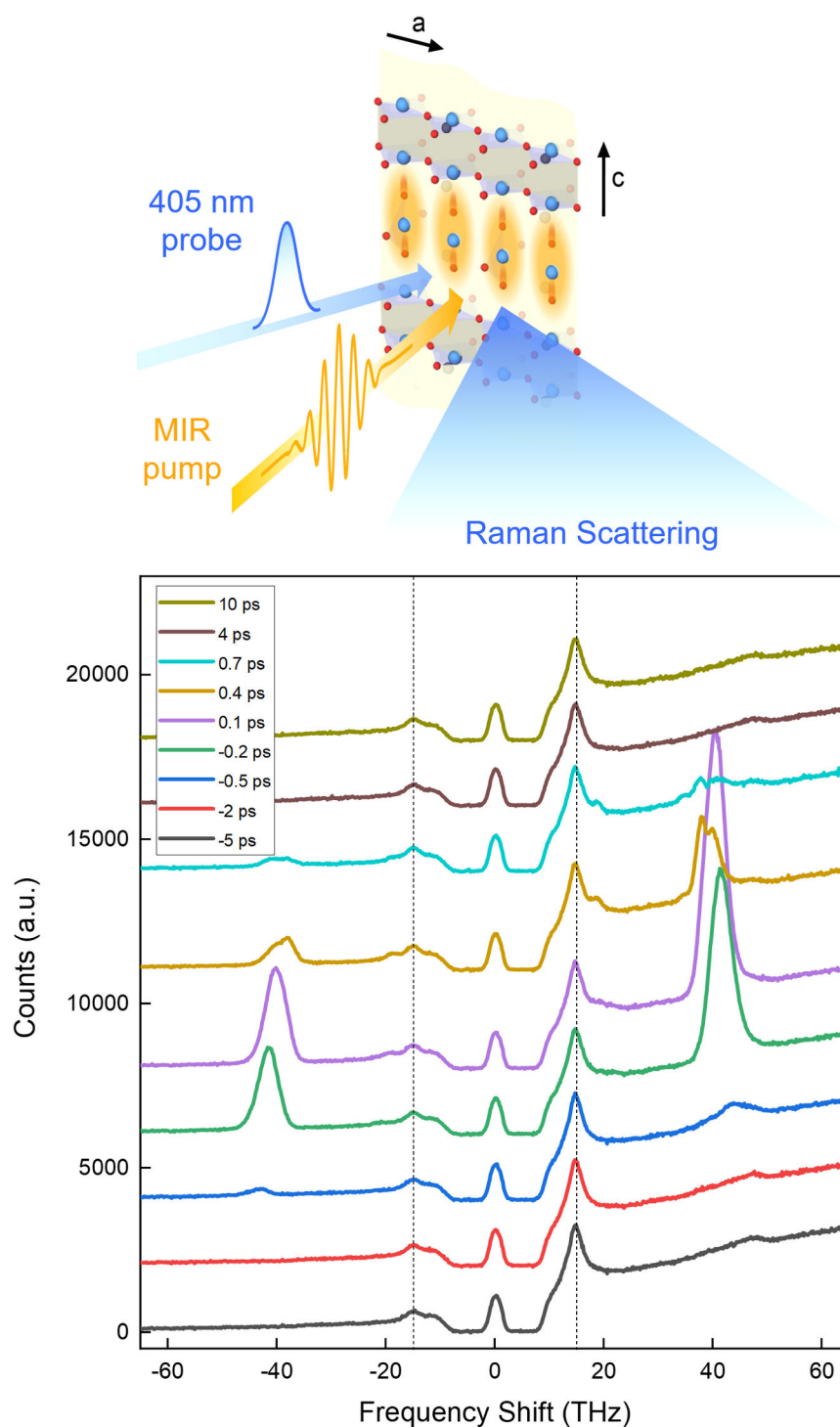


Figure 5.11: Top panel: Schematic of time-resolved spontaneous Raman spectroscopy. The mid-IR pump pulse (yellow) resonantly drives infrared-active *c*-axis apical oxygen phonons in $\text{YBa}_2\text{Cu}_3\text{O}_{6.48}$. Visible 405-nm probe pulses (blue) were used for the Raman scattering process. The scattered photons were collected and analyzed by a spectrometer. Bottom panel: Raman spectra measured in $\text{YBa}_2\text{Cu}_3\text{O}_{6.48}$ at $T = 295$ K at various pump-probe time delays. The pump and probe fluences were 8 and 1.35 mJ/cm^2 , respectively. The dashed lines label the positions of Stokes and Anti-Stokes Raman peaks at ± 15 THz.

delays, we observe some features: 1) The signals drop at ± 10 THz. This is caused by the blocking bandwidth of the notch filter. The small peak at zero frequency shift comes from the leakage of the strong elastic scattering. 2) The signal slowly increases from negative frequency shift to positive (low wavelength to high wavelength). We attribute this slowly increasing background to the scattering light from the cryostat window and, potentially, the probe-induced photoluminescence effect from $\text{YBa}_2\text{Cu}_3\text{O}_{6.48}$ [74, 75]. 3) On top of the background, we find the Stokes (S) and Anti-Stokes (AS) peaks of the apical oxygen Raman-active A_{1g} phonon at ± 15 THz (highlighted by dashed lines).

When the pump is on, the Raman spectra measured close to zero time delay show additional features, we observe small peaks at ± 20 THz and large peaks at ± 40 THz. These peaks are maximized when pump and probe pulses are overlapped in time, and their center frequencies match exactly the fundamental and second-harmonic frequencies of the pump pulses. We ascribe these peaks to second-order and third-order nonlinear optical polarizations induced by the electric fields of the 405-nm probe and 20-THz pump pulses. The second-order ($\chi^{(2)}E_{pump}E_{probe}$) and third-order ($\chi^{(3)}E_{pump}^2E_{probe}$) nonlinear processes result in photons at the frequencies of $405 \text{ nm} \pm 20 \text{ THz}$ and $405 \text{ nm} \pm 40 \text{ THz}$. To provide more evidence, we have tuned the mid-IR pump pulses to a frequency of 28 THz and these peaks shift to ± 28 THz and ± 56 THz accordingly. Since the $\text{YBa}_2\text{Cu}_3\text{O}_{6.48}$ is a centrosymmetric crystal, $\chi^{(2)}$ is forbidden under dipole approximation. The small second-order peaks may arise from the other components (e.g. sample mount, cryostat window, ...) or from a quadrupole contribution. In contrast, the third-order peaks are relatively strong because $\chi^{(3)}$ is allowed in the $\text{YBa}_2\text{Cu}_3\text{O}_{6.48}$ sample.

To extract the amplitudes of the Stokes and Anti-Stokes peaks in the detected spectra, we describe the procedure of the background subtraction and the model used to fit the Raman peaks. Figure 5.12a shows the raw Raman spectrum taken in the $y(zz)\bar{y}$ geometry at a time delay of -5 ps (red curve), together with a background spectrum obtained in the $y(xz)\bar{y}$ geometry, where the input probe pulses are polar-

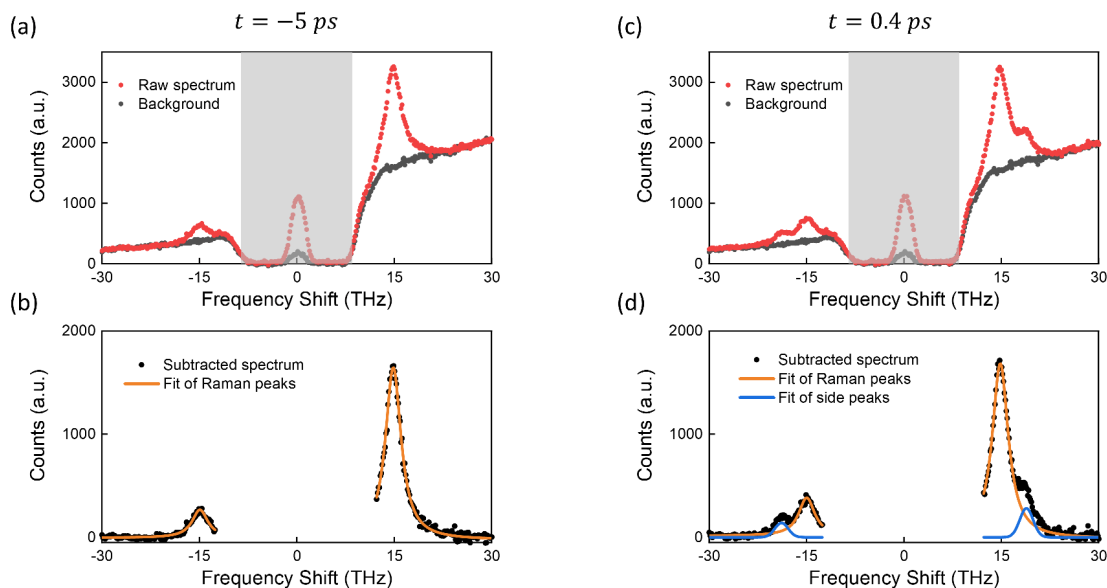


Figure 5.12: (a) Raw Raman spectrum measured in $\text{YBa}_2\text{Cu}_3\text{O}_{6.48}$ at room temperature and negative time delay (red dots). The black dots show the background spectrum (see text). The gray area indicates the blocking range of the 405-nm notch filter. (b) Background-subtracted Raman spectrum (black), along with a Lorentzian fit to the Stokes and Anti-Stokes peaks at ± 15 THz (orange). (c, d) Same quantities as in (a, b), respectively, measured at a positive time delay $t = 0.4$ ps. The blue line in (d) is a Gaussian fit to the two peaks at ± 20 THz, which result from nonlinear optical mixing between the pump and the probe pulses within their cross-correlation width. This figure is reprinted from Ref. [24]

ized along a-axis and the output scattered photons are filtered by a c-axis polarizer. We adopted this method to obtain the background spectrum as the $y(xz)\bar{y}$ geometry does not probe the A_{1g} modes. Although, on the other hand, it can in principle detect the B_{1g} and B_{2g} modes, our data showed no visible peak features from these modes. Additionally, we found the background spectrum can reproduce the slowly increasing slope in the Raman spectrum. This approach allowed us to obtain a background spectrum that closely matches the Raman spectrum, with only the A_{1g} Raman peak missing. All Raman spectra used for the data analysis were achieved by subtracting this background from the raw spectrum. Figure 5.12b clearly shows the Stokes and Anti-Stokes peaks of the A_{1g} Raman mode at ± 15 THz. This background-subtracted Raman spectrum was fitted by two Lorentzian peaks with equal linewidths to determine the amplitudes of both Raman peaks.

Figures 5.12c and 5.12d show the transient Raman spectrum measured at a time delay of +0.4 ps. Two additional peaks appear at ± 20 THz (second-order peaks). The transient spectra were analyzed by again fitting a Lorentzian function to the Raman peaks (orange) and a Gaussian function to the additional peaks (blue). The amplitude ratio of the Raman AS and S peaks was extracted from the fitted Lorentzian functions.

After subtracting both the background spectrum and these second-order peaks, the resulting Raman spectra at time delays of -5 ps (black) and 0.4 ps (orange) are shown in Fig. 5.13. The amplitude of the AS peak is enhanced at positive time delay, while the S peak amplitude barely changed. This indicates an increase of the phonon temperature after the mid-IR excitation. As described in Section 5.3.1, the intensity ratio of the AS and S peaks, I_{AS}/I_S , is related to the distribution of the phonon populations in the ground state and the first excited state and allows us to calculate the temperature of this Raman mode using

$$\frac{I_{AS}}{I_S} = \frac{(\omega_0 + \omega_{ph})^3}{(\omega_0 - \omega_{ph})^3} \exp\left(\frac{-\hbar\omega_{ph}}{k_B T_{ph}}\right) \quad (5.22)$$

where ω_{ph} is the frequency of the Raman mode and T_{ph} is the phonon temperature according to the Bose-Einstein distribution.

5.4.2 Extrapolated zero-fluence phonon temperatures

In our experiments at a laser repetition rate of 1 kHz, the probe fluences were set between 0.5 and 2 mJ/cm² to ensure sufficient numbers of scattered photons for the data acquisition. However, such high probe fluences unavoidably introduce additional sample heating and potentially induce other nonlinear effects. For example, at the base temperature of 100 K, even when using the lowest possible probe fluence 0.5 mJ/cm² to measure the AS/S intensity ratio, we still observe a phonon temperature of 180 K, which is 80 K above the base temperature of the cryostat.

First, we suspected this discrepancy to arise from cumulative heating from the

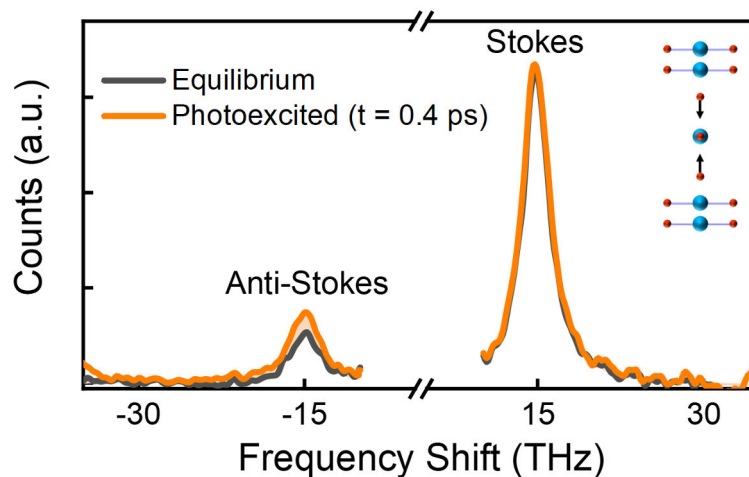


Figure 5.13: The Raman spectra were measured at $T = 295\text{K}$ at equilibrium (black) and after pump excitation (orange). The displayed data were obtained by subtracting background spectra and second-order side peaks from the raw data. The peaks at ± 15 THz represent the Stokes (+) and Anti-Stokes (-) responses of the A_{1g} symmetry apical oxygen Raman mode. Inset: atomic motions along the c -axis apical oxygen Raman-active mode coordinates. This figure is reprinted from Ref. [24]

probe pulses. We performed a simulation of this effect considering the 0.2 mW average probe power at the sample, the thermal conductivity, and the mounting geometry of the sample and cold finger (see Appendix for details). As depicted in Fig. 5.14, the steady-state temperature was calculated to be 100.35 K, with a temperature rise of 0.35 K, far smaller than the observed 80 K increase.

Next, we examined if the pulsed heating from the probe pulse could explain this issue. When the sample absorbs a probe pulse, the system thermalizes in the time scale of tens of picoseconds. The temperature rise resulting from this effect can be calculated by considering the probe pulse fluence, the excited volume, and the heat capacity of the sample (see Appendix for details). The result, depicted in Fig. 5.14, indicates that a 0.5 mJ/cm^2 405-nm probe pulse leads to a pulsed heating of 25 K, significantly lower than the experimentally observed 80 K.

Hence, the origin of this anomalous heating effect remains unclear. For an accurate measurement of the phonon temperatures, it is therefore crucial to characterize the effect of the probe pulses on the time-dependent Raman spectra. Figure 5.15 shows the probe fluence dependent AS/S intensity ratios on $\text{YBa}_2\text{Cu}_3\text{O}_{6.48}$ in the

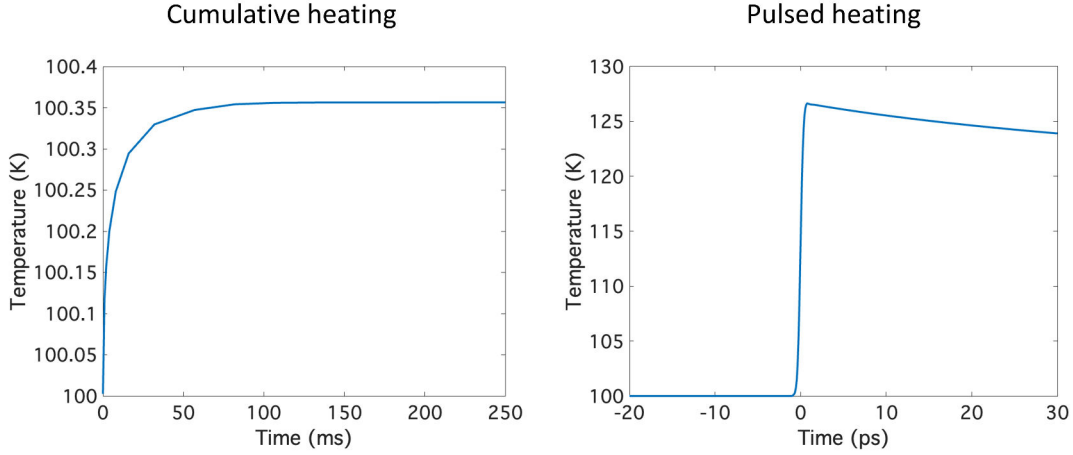


Figure 5.14: Left panel: Time evolution of temperature rise due to cumulative heating. The 0.2 mW probe beam leads to a 0.35 K temperature rise in our sample. Right panel: Time evolution of temperature rise due to pulsed heating. A 0.5 mJ/cm² probe pulse induces a 25 K transient heating in our sample

absence of the mid-IR excitation pulses. At both base temperatures of 295 and 100 K, the AS/S intensity ratio increases linearly with probe fluence. The extrapolated ‘zero-fluence’ AS/S ratios, obtained by a linear fit to the data, corresponds to phonon temperatures that match the base temperatures set by the cryostat. This observation suggests that it is possible to experimentally bypass the probe heating effect on our analysis by performing a linear extrapolation to the probe-fluence dependence and extracting a ‘zero-fluence’ phonon temperature.

To this end, we conducted the time-resolved Raman experiments at multiple probe fluences ranging from 0.8 to 2.0 mJ/cm² and extracted the zero-fluence phonon temperature for pump-probe each time delay. This approach ensures that the phonon temperature is equal to the base temperature at negative time delay, thereby providing a reliable measurement of the temperature increase induced by the mid-IR excitation. Figure 5.16 presents the AS/S peak intensity ratios as a function of time delay under these experimental conditions, for both the nominal base temperatures of 295 and 100 K. To determine the zero-fluence phonon temperature for each time delay, we applied the following procedure. First, we collected all fluence-dependent data at negative delays, recorded before the pump reached the sample (-5 to -0.8

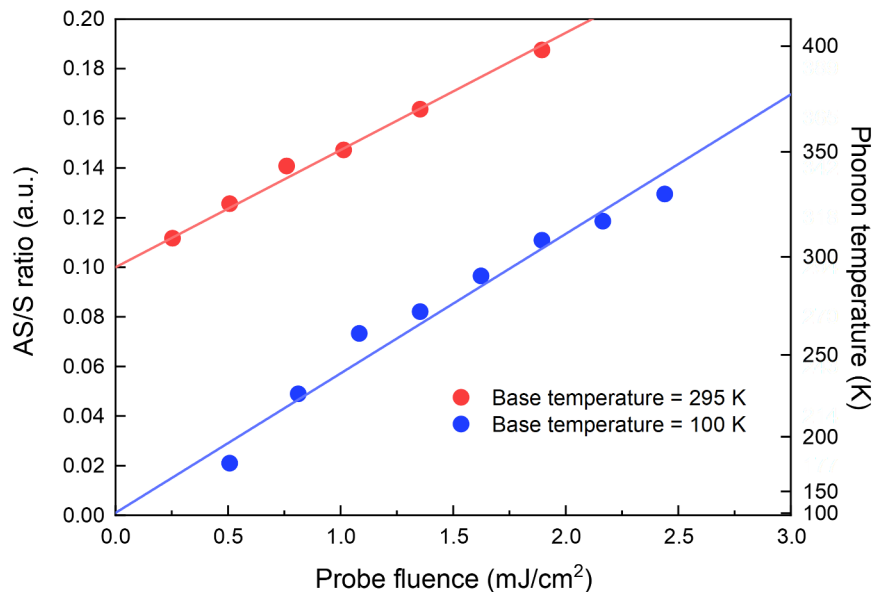


Figure 5.15: The measured AS/S ratios of the detected 15 THz Raman phonon as a function of the 405-nm probe fluence, for base temperatures of 295 K (red) and 100 K (blue). The phonon temperatures shown on the right axis are calculated from the AS/S ratio on the left axis using Eq. (5.22). This figure is reprinted from Ref. [24]

ps), and performed a linear fit on this combined dataset. From this analysis, we extracted the slope of the probe fluence-dependent AS/S peak intensity ratios by constraining the intercept at 0.1, corresponding to a phonon temperature of 295 K. Next, we used this slope to fit the fluence-dependent data at each time delay, allowing us to extrapolate and determine the AS/S intensity ratios at zero fluence. These values were then converted into time delay-dependent phonon temperatures using Eq. (5.22). The same method was applied to the 100 K dataset, where the intercept was fixed at 0.001, corresponding to a phonon temperature of 100 K. Note that the extracted slope for 100 K data is different than that of 295 K data.

The error bars on the phonon temperatures were determined based on the standard errors of the extrapolated zero-fluence AS/S intensity ratios. Note that for the 100 K data, we removed three data points at time delays -1.4, -0.8, and -0.5 ps, where the extrapolated AS/S ratios were smaller than zero. Additionally, if the AS/S ratios minus one standard error resulted in negative values, the lower bounds of the error bars were set to 0 K. The uncertainties of lower-temperature (<120

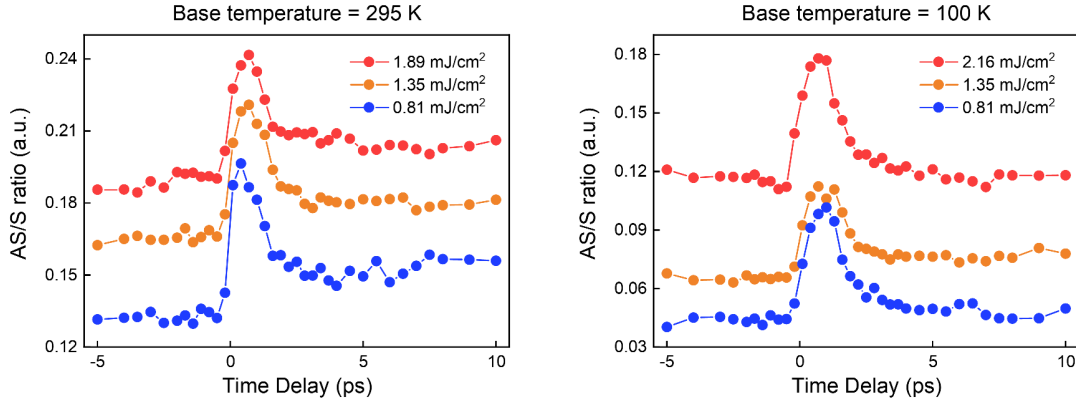


Figure 5.16: Left panel: Time evolution of the AS/S ratios measured at the base temperature of 295 K with probe fluences of 1.89, 1.35, 0.81 mJ/cm². Right panel: Time evolution of AS/S ratios measured at the base temperature of 100 K with probe fluences of 2.16, 1.35, 0.81 mJ/cm². This figure is reprinted from Ref. [24]

K) data points were much larger than the higher-temperature data points. This is because the relation between AS/S ratios and phonon temperatures, as plotted in Fig. 5.17, is almost linear in the range of 200-400 K, but becomes highly nonlinear at low temperatures near 100 K. Hence, a small variation in AS/S ratio only gives a finite error in the higher temperature range, but result in a huge error at low temperature.

Following the above-mentioned procedure, Figure 5.18 shows the time evolutions of the zero-fluence phonon temperatures in YBa₂Cu₃O_{6.48} measured at base temperatures of 295 and 100 K. Both transients display a prompt rise in phonon temperature near time zero followed by an exponential decay to a temperature slightly higher than the base temperature. This can be interpreted as the thermalization of this phonon with other degrees of freedom in the system. We first focus on the data at long positive time delays (>5 ps). Here, we expect all the hot incoherent phonons have dissipated the energy to the lattice and reach quasi-thermal equilibrium. The temperature difference between initial base temperature and final thermalized temperature should be agreed with a calculation based on the total energy absorbed by the sample, the excited volume, and the heat capacity (see Appendix for details). For a mid-IR excitation density of 8 mJ/cm², shown as the red dashed line in Fig.

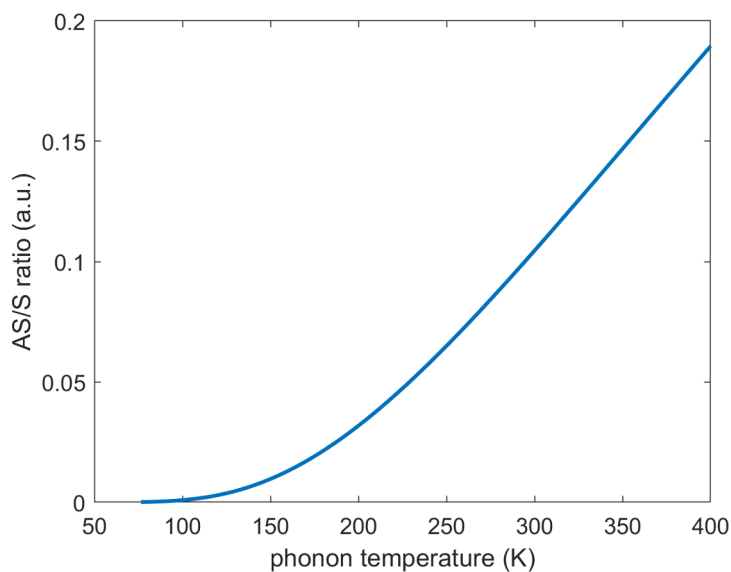


Figure 5.17: The relation between the AS/S amplitude ratios and the calculated phonon temperatures using Eq. (5.22).

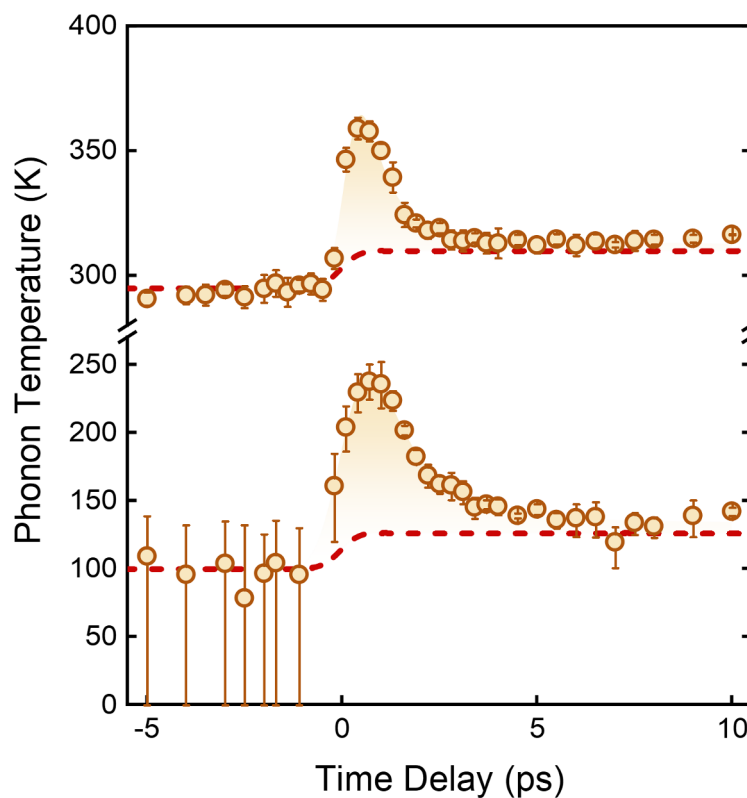


Figure 5.18: Zero-fluence phonon temperatures as a function of time delay. These data were measured at cryostat base temperatures of 295 K (upper) and 100 K (lower). The dashed red lines were obtained from heating calculation (see Appendix for details). This figure is reprinted from Ref. [24]

5.18, the calculated temperature of the $\text{YBa}_2\text{Cu}_3\text{O}_{6.48}$ surface increased from 295 K (100 K) and thermalized at 310 K (125 K). The measured phonon temperatures at negative and long positive time delay agree with the calculation.

We next turn to the results at earlier time delays, that is before thermalization. A nonequilibrium phonon temperature of 360 K was measured at the peak of the signal for the base temperature of 295 K, well above the equilibrated temperature of 310 K at longer delays. In the case of 100 K base temperature, an initial overshoot up to 240 K was observed, followed by thermal equilibration to 125 K on the longer time scale. These peak temperatures are far lower than what reported for near-infrared excitation in Ref. [68] at similar excitation fluences. At 100 K base temperature, the transient phonon temperature increase of 140 K broadly compatible with the quasiparticle temperature overshoot extracted from the measurements of the optical conductivity $\sigma_1(\omega, t)$, and both show similar decay time constants of 1.3 ps.

5.5 Comparison of phonons, quasiparticles, and superfluid responses

Figure 5.19a summarizes the temperature changes of incoherent quasiparticles and phonons in the optically-driven $\text{YBa}_2\text{Cu}_3\text{O}_{6.48}$ at 100 K. Despite the uncertainty introduced by the choice of model to extract $T_{\text{Quasiparticle}}$ from the data, the peak temperature of quasiparticles is estimated to range between 200 K and 300 K, which is largely compatible with the peak phonon temperature of 240 K. Following the initial prompt rise, the temperatures of both quasiparticles and phonons decay with the similar lifetime, reaching thermal equilibrium within 5 ps to 10 ps.

Although we expect both the quasiparticles and phonons should thermalize to the final temperature 125 K (see Appendix), the quasiparticle temperature appears slightly lower. One possible reason to this issue could be the assumption that the scattering rate remains unchanged after excitation, potentially leading to an under-

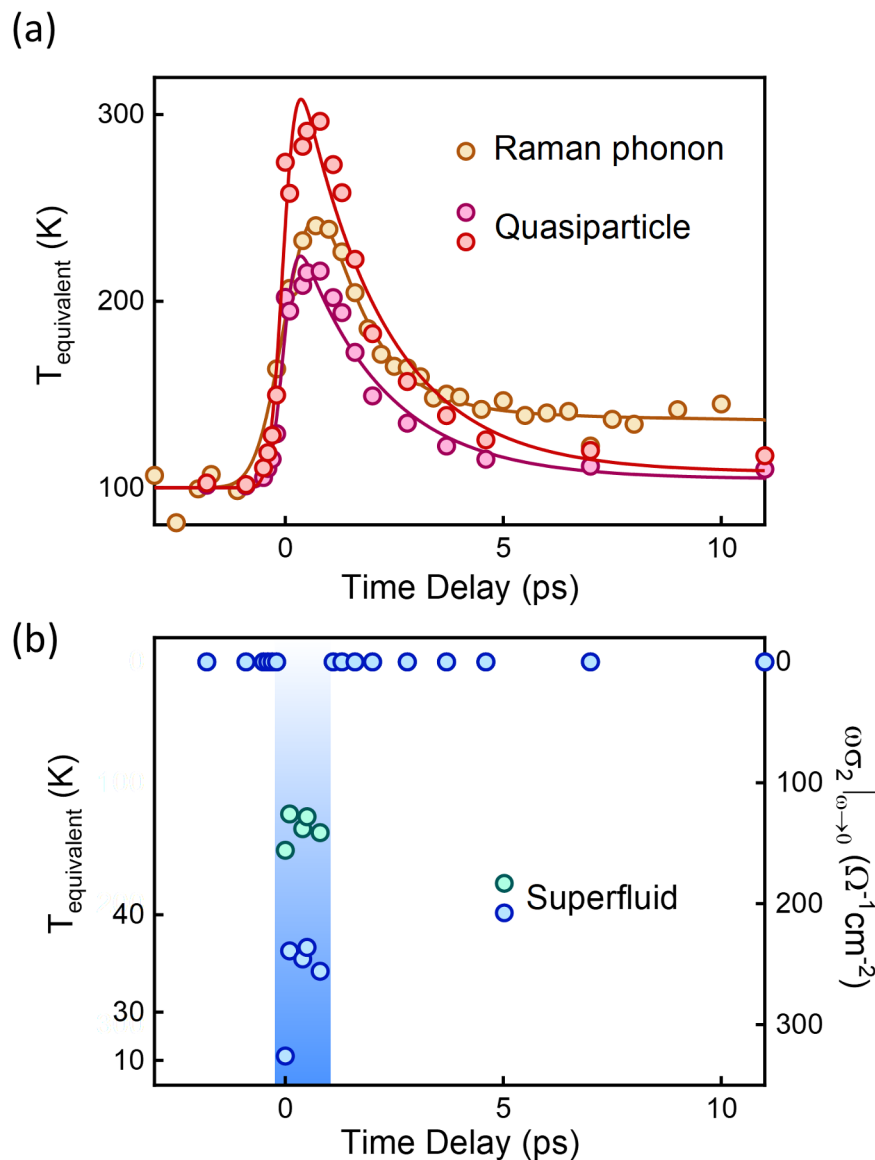


Figure 5.19: (a) Equivalent temperatures of quasiparticles and phonons as a function of time delay. The solid lines are fits to the data with a model including an error function and an exponential decay. The red and purple circles refer to different models used to extract the THz (quasiparticle) response, assuming a linear or a square-root dependence as a function of pump fluence, respectively [47, 48]. (b) Equivalent temperatures of the superfluid as a function of time delay [23]. The blue shaded area highlights the time delay window within which a transient superconductinglike response was observed. The equivalent temperature of the superfluid was determined from $\lim_{\omega \rightarrow 0} \omega \sigma_2(\omega)$ (values reported on the right axis), using the same models discussed in (a) to calculate the THz response, i.e., linear (blue circles) or square-root (light green circles). This figure is reprinted from Ref. [24]

estimation of the quasiparticle temperatures. Nonetheless, the overall dynamics of both quasiparticles and phonons show comparable peak temperatures and thermalization times.

These hot incoherent degrees of freedom are to be compared to the dynamics of the superfluid, manifested in the strength of the divergent imaginary part of the optical conductivity $\sigma_2(\omega)$. In Section 3.4, the time delay dependent $\sigma_2(\omega)$ spectra were used to calculate values of $\lim_{\omega \rightarrow 0} \omega \sigma_2(\omega)$, which is directly related to the superfluid density. By comparing these values with equilibrium optical conductivity spectra taken at multiple temperatures below T_c , the “equivalent temperature” of the superfluid was extracted. The time evolution of the coherent superfluid in response to the mid-IR excitation is presented in Fig. 5.19b. In contrast to the longer-lived effects observed on incoherent phonons and quasiparticles, the equivalent “cooling” of superfluid only persists within the duration of pump pulse.

Discussion

Our observation that both quasiparticles and phonons exhibit comparable temperature dynamics deviates from the conventional two-temperature model (TTM). The TTM typically describes materials with weak electron-phonon coupling, where quasiparticles absorb energy quickly and then slowly transfer it to phonons. In such cases, the quasiparticles reach significantly higher peak temperatures and decay much faster than phonons. However, in our case, $\text{YBa}_2\text{Cu}_3\text{O}_{6.48}$ exhibits strong electron-phonon coupling, facilitating fast and efficient energy exchange between quasiparticles and phonons. When energy transfer occurs rapidly, the system can achieve a quasi-equilibrium state between quasiparticles and phonons even within picosecond timescales. This may account for the similar peak temperatures and thermalization times observed for both quasiparticles and phonons.

As shown in Fig. 5.19b, the lifetime of the coherent superfluid is never observed to exceed the duration of the excitation pulse. During this brief time, both quasipar-

ticles and phonons become overpopulated, effectively heating the system (initially at 100 K) to approximately 240 K. One possible explanation for these observations is that both quasiparticles and phonons are detrimental to the coherent superconducting state. Once the optical drive is switched off, the hot incoherent quasiparticles and phonons interact with the coherent superfluid. These interactions may transfer energy to the superfluid, leading to the destruction of Cooper pairs or loss of coherence. As the system heats to 240 K, the excessive populations of quasiparticles and phonons could dramatically shorten the decoherence time of the superfluid, explaining the rapid loss of light-induced superconducting state.

In conclusion, we have characterized the equivalent temperatures of quasiparticles, phonons, and superfluid and discuss their dynamics and interactions. One should focus on optimizing the conditions of the optical drive to minimize the excitation of hot incoherent carriers. Suitably shaped pump pulses or trains of pump pulses may provide a stronger and longer-lived photoinduced state.

Chapter 6

Summary and outlook

Ultrafast optical excitation has become a powerful tool for the non-thermal control of phase transitions in strongly correlated materials. In particular, intense mid-IR light sources have been used to resonantly excite optical phonons, driving materials into non-equilibrium phases. One of the most remarkable examples is light-induced superconductivity in underdoped $\text{YBa}_2\text{Cu}_3\text{O}_{6+x}$, where a transient superconducting state has been observed even at room temperature. This is a significant discovery in the field of high-temperature superconductivity, strongly linked to the coherent optical excitation of apical oxygen phonons. The underlying mechanisms of coherent coupling to other modes of the system has been extensively studied in the past.

Despite the promise of this transient superconducting state, a major limitation is the extremely short lifetime of order of a few picoseconds. Such short lifetime restricts its potential for practical applications. It is believed that the decay of the superconducting state arises from the dynamics of incoherent carriers, such as hot quasiparticles, and phonons, whose heating effects tend to disrupt the superconducting-like state. The aim of this thesis is to characterize the transient temperatures of incoherent quasiparticles and phonons when subjected to the mid-IR excitation.

To this end, I developed time-resolved spontaneous Raman scattering experi-

ments to directly probe the phonon population of a spectator Raman mode, which provides a measure of the transient lattice temperatures. Conducting a spontaneous Raman scattering experiment with intense optical probe pulses at 1 kHz repetition rate was complicated by an anomalous heating effect. This obstacle was successfully overcome by extrapolating pulse-energy-dependent measurements to zero energy in order to extract the accurate phonon temperatures.

The dynamics of hot incoherent phonons revealed a rapid temperature increase from a base temperature of 100 K to 240 K, followed by an exponential decay to thermal equilibrium within 10 picoseconds. This behavior was compared with the temperature evolution of quasiparticles, inferred from previous time-resolved THz spectroscopy experiments. Strikingly, both quasiparticles and phonons exhibit similar peak temperatures and relaxation timescales, suggesting an efficient and rapid energy exchange between the two subsystems. In contrast, the coherent superfluid experiences an effective cooling and exists only over a shorter time interval. Both quasiparticles and phonons appear to contribute with comparable strength to the decoherence time of the light-induced superconducting state.

Future research on light-induced superconductivity can proceed along two main directions. Firstly, conducting Raman scattering experiments on $\text{YBa}_2\text{Cu}_3\text{O}_{6+x}$ at different doping levels can provide valuable insights. In antiferromagnetic insulating cuprates, two-magnon Raman scattering appears as a broadband peak at a high frequency shift, related to the superexchange energy of the antiferromagnetic order [76–79]. Additionally, recent studies have found that cuprates with CDW order exhibit distinctive features in the B_{2g} Raman scattering spectra [80–82]. Combining the probe of antiferromagnetic and CDW orders with mid-IR excitation will provide deeper insights into light-induced superconductivity in $\text{YBa}_2\text{Cu}_3\text{O}_{6+x}$ and potentially elucidate the pairing mechanism.

The second direction is to extend time-resolved Raman scattering experiments to light-induced superconductivity in the organic superconductor K_3C_{60} [13, 46, 51], where mid/far-IR excitation was shown to induce long-lived superconducting states

also at room temperature, but also at time scales more than a hundred times longer than the excitation pulses. Earlier research has shown that Raman scattering can probe the superconducting gap in alkali-doped fulleride compounds at equilibrium [83, 84]. Combined with optical excitation, the dynamics of the superconducting gap can be investigated. Although THz reflectivity experiments also provide information about the gap, Raman scattering is a better approach because the penetration depth of UV/visible probe is shorter than that of mid/far-IR pump. As no additional reconstruction is needed [46–48], the Raman approach can directly probe the superconducting gap, advancing knowledge in the field of light-induced superconductivity.

Lastly, the impact of this work extends beyond the specific case of light-induced superconductivity to other examples of light-induced phase control. By studying the behavior of hot incoherent phonons, one can gain crucial insights into how energy dissipates throughout the system following ultrafast optical excitation. Understanding the interactions between incoherent phonons and other subsystems, such as quasiparticles or magnons, could help optimize the conditions of optical drive for non-thermal phase control. For instance, minimizing the effects of incoherent heating while sustaining the coherent driving of specific modes could lead to more efficient phase control and longer-lived transient phases. These findings may enhance our ability to manipulate material phases upon illumination by light.

Chapter 7

Appendix

Fit and deconvolution of phonon temperatures

The dynamics of phonon temperatures extracted from the time-resolved Raman scattering experiments reveal a fast initial heating and an exponential decay to a quasi-equilibrium temperature within a few picoseconds. This behavior can be expressed by the function

$$T(t) = T_0 + \frac{1}{2}A \left(1 + \operatorname{erf}\left(\frac{t}{\sigma}\right) \right) \left[\exp\left(-\frac{t}{\tau_1}\right) + (1 - A)\exp\left(-\frac{t}{\tau_2}\right) \right] \quad (7.1)$$

Here, T_0 is the base temperature, which is set to either 295 K or 100 K depending on the experimental setting, A is proportional to the initial temperature rise, and $\operatorname{erf}\left(\frac{t}{\sigma}\right)$ is the error function with σ the time resolution of the experiment. The few-picosecond recovery of the temperature to a quasi-equilibrium value above the base temperature T_0 is described by a double exponential decay with a fast time constant τ_1 and a very long time constant τ_2 . The fit results are shown as brown lines in Fig. 7.1.

The experimentally extracted lattice temperatures, as well as the corresponding fits shown above, could potentially be underestimated due to the limited time resolution of the experiment given. Therefore, we deconvolved the lattice temperature

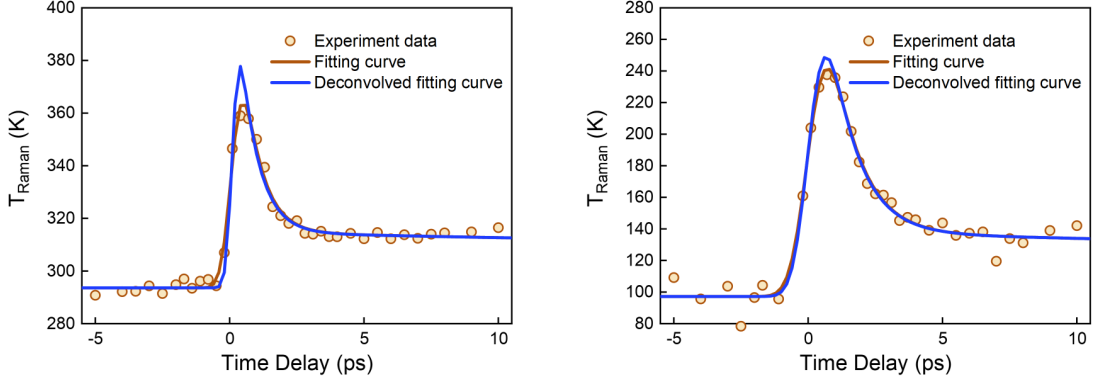


Figure 7.1: Time evolution of Raman phonon temperature in driven $\text{YBa}_2\text{Cu}_3\text{O}_{6.48}$ measured for 295 (left) and 100 K (right) base temperature. The brown lines are fitting curves to the data, while the blue lines show the deconvolved response obtained after the process described in the text. This figure is reprinted from Ref. [24]

data from the duration of the probe pulse using

$$T_D(t) = iFT \left(\frac{FT(T(t))}{FT(g(t))} \right) \quad (7.2)$$

Here, $T_D(t)$ is the deconvolved temperature dynamics, FT and iFT represent Fourier transform and inverse Fourier transform, respectively. Furthermore, $T(t)$ is the fitting function introduced in Eq. (7.1) and $g(t)$ is the Gaussian envelope function $\frac{1}{c\sqrt{2\pi}} \exp\left(-\frac{t^2}{2c^2}\right)$ where c corresponds to the 600-fs duration (FWHM) of the visible probe pulse. Figure 7.1 shows the deconvolved temperature dynamics for the two experimental settings (blue lines). At the base temperature of 295 K, the deconvolved peak lattice temperature is 375 K, equivalent to a temperature rise of 80 K. At the base temperature of 100 K, the peak temperature is 250 K corresponding to a temperature increase of 150 K.

Heating calculation

This Section presents the calculations of cumulative heating and pulsed heating caused by the laser pulse (either probe or pump) in our sample. The basic form of heating diffusion equation is given by

$$\frac{\partial T(x, t)}{\partial t} = \frac{k}{\rho C_p(T)} \frac{\partial^2 T(x, t)}{\partial x^2} + \frac{Q(x, t)}{\rho C_p(T)} \quad (7.3)$$

where T is the temperature, ρ is the density, $C_p(T)$ is the temperature-dependent heat capacity [85,86], k is the thermal conductivity, x is the space coordinate (with $x = 0$ being the sample surface), and $Q(x, t)$ is the heat source term, representing the energy input from the laser pulse.

First, we focus on the cumulative heating effect. To simulate the steady-state temperature caused by the laser pulse, the time-dependent term $\partial T/\partial t$ drops to zero and Eq. (7.3) can be simplified to the Laplace equation with a heat source term.

$$\frac{\partial^2 T(x)}{\partial x^2} = -\frac{Q(x)}{k} \quad (7.4)$$

Here, the source term $Q(x)$ represents continuous energy input, which consider the time-averaged laser power. As a result, the steady-state temperature depends only on the laser pulse power and the thermal conductivity of the sample. In Section 5.4.2, we simulate the steady-state temperature in $\text{YBa}_2\text{Cu}_3\text{O}_{6.48}$ at 100 K caused by the 0.2 mW probe pulse. The result indicates a temperature increase from 100 K to 100.35 K.

Next, we consider the pulsed heating effect, which occurs when the sample absorb energy from a single laser pulse, leading to a temperature rise as the system thermalizes to equilibrium. This process happens over the timescales from picoseconds to nanoseconds. To estimate the final thermalized temperature at the $\text{YBa}_2\text{Cu}_3\text{O}_{6.48}$ surface due to the pump (or probe) excitation, we rewrite Eq. (7.3) and neglect the thermal diffusion term

$$\rho C_p(T) \frac{\partial T(x, t)}{\partial t} = \frac{1}{d} (1 - R) I(t) \exp\left(\frac{-x}{d}\right) \quad (7.5)$$

where d is the penetration depth of the pump pulse (which scales from 1.5 – 4 μm), R is the reflectivity, and $I(t)$ is the time evolution of the 800-fs Gaussian pump pulse. The calculation takes into account the total energy of a single pulse absorbed by the sample, the excited volume, and the heat capacity. For any given initial temperature T_i , we integrated Eq. (7.5) in time t to obtain the final temperature distribution $T_f(x, t)$ and report $T_f(0, t)$ as a function of time t to present the temperature change at the sample surface.

In Section 5.4.2, Figure 5.14 shows that the pulsed heating from the 0.5 mJ/cm^2 , 405-nm probe pulse results in a temperature increase from 100 K to 125 K in $\text{YBa}_2\text{Cu}_3\text{O}_{6.48}$, which cannot explain the observed probe heating effect. On the other hand, in Fig. 5.18, we calculate the pulsed heating from 8 mJ/cm^2 , 20 THz pump pulse in $\text{YBa}_2\text{Cu}_3\text{O}_{6.48}$ at the initial temperatures of 100 K and 295 K. The final thermalized temperatures are 125 K and 310 K, respectively. These results agree with the measured phonon temperatures at long positive time delay.

Bibliography

- [1] Andrea Cavalleri. Photo-induced superconductivity. *Contemporary Physics*, 59(1):31–46, 2018.
- [2] K. Miyano, T. Tanaka, Y. Tomioka, and Y. Tokura. Photoinduced insulator-to-metal transition in a perovskite manganite. *Phys. Rev. Lett.*, 78:4257–4260, 1997.
- [3] E. Beaurepaire, J.-C. Merle, A. Daunois, and J.-Y. Bigot. Ultrafast spin dynamics in ferromagnetic nickel. *Phys. Rev. Lett.*, 76:4250–4253, 1996.
- [4] S. Hellmann, M. Beye, C. Sohrt, T. Rohwer, F. Sorgenfrei, H. Redlin, M. Kalläne, M. Marczynski-Bühlow, F. Hennies, M. Bauer, A. Föhlisch, L. Kipp, W. Wurth, and K. Rossnagel. Ultrafast melting of a charge-density wave in the mott insulator $1T\text{-TaS}_2$. *Phys. Rev. Lett.*, 105:187401, 2010.
- [5] Andrei Kirilyuk, Alexey V. Kimel, and Theo Rasing. Ultrafast optical manipulation of magnetic order. *Rev. Mod. Phys.*, 82:2731–2784, 2010.
- [6] J. Hohlfeld, E. Matthias, R. Knorren, and K. H. Bennemann. Nonequilibrium magnetization dynamics of nickel. *Phys. Rev. Lett.*, 78:4861–4864, 1997.
- [7] A. Tomeljak, H. Schäfer, D. Städter, M. Beyer, K. Biljakovic, and J. Demsar. Dynamics of photoinduced charge-density-wave to metal phase transition in $\mathbf{K}_{0.3}\text{MoO}_3$. *Phys. Rev. Lett.*, 102:066404, 2009.

- [8] M. Först, C. Manzoni, S. Kaiser, Y. Tomioka, Y. Tokura, R. Merlin, and A. Cavalleri. Nonlinear phononics as an ultrafast route to lattice control. *Nature Physics*, 7(11):854–856, 2011.
- [9] Roman Mankowsky, Michael Först, and Andrea Cavalleri. Non-equilibrium control of complex solids by nonlinear phononics. *Reports on Progress in Physics*, 79(6):064503, 2016.
- [10] Alaska Subedi, Andrea Cavalleri, and Antoine Georges. Theory of nonlinear phononics for coherent light control of solids. *Phys. Rev. B*, 89:220301, 2014.
- [11] A. S. Disa, J. Curtis, M. Fechner, A. Liu, A. von Hoegen, M. Först, T. F. Nova, P. Narang, A. Maljuk, A. V. Boris, B. Keimer, and A. Cavalleri. Photo-induced high-temperature ferromagnetism in YTiO_3 . *Nature*, 617(7959):73–78, 2023.
- [12] D. Fausti, R. I. Tobey, N. Dean, S. Kaiser, A. Dienst, M. C. Hoffmann, S. Pyon, T. Takayama, H. Takagi, and A. Cavalleri. Light-induced superconductivity in a stripe-ordered cuprate. *Science*, 331(6014):189–191, 2011.
- [13] M. Mitrano, A. Cantaluppi, D. Nicoletti, S. Kaiser, A. Perucchi, S. Lupi, P. Di Pietro, D. Pontiroli, M. Riccò, S. R. Clark, D. Jaksch, and A. Cavalleri. Possible light-induced superconductivity in K_3C_{60} at high temperature. *Nature*, 530(7591):461–464, 2016.
- [14] T. F. Nova, A. S. Disa, M. Fechner, and A. Cavalleri. Metastable ferroelectricity in optically strained SrTiO_3 . *Science*, 364(6445):1075–1079, 2019.
- [15] S. Kaiser, C. R. Hunt, D. Nicoletti, W. Hu, I. Gierz, H. Y. Liu, M. Le Tacon, T. Loew, D. Haug, B. Keimer, and A. Cavalleri. Optically induced coherent transport far above T_c in underdoped $\text{YBa}_2\text{Cu}_3\text{O}_{6+\delta}$. *Phys. Rev. B*, 89:184516, 2014.
- [16] W. Hu, S. Kaiser, D. Nicoletti, C. R. Hunt, I. Gierz, M. C. Hoffmann, M. Le Tacon, T. Loew, B. Keimer, and A. Cavalleri. Optically enhanced coher-

-
- ent transport in $\text{YBa}_2\text{Cu}_3\text{O}_{6.5}$ by ultrafast redistribution of interlayer coupling. *Nature Materials*, 13(7):705–711, 2014.
- [17] C. R. Hunt, D. Nicoletti, S. Kaiser, D. Pröpper, T. Loew, J. Porras, B. Keimer, and A. Cavalleri. Dynamical decoherence of the light induced interlayer coupling in $\text{YBa}_2\text{Cu}_3\text{O}_{6+\delta}$. *Phys. Rev. B*, 94:224303, 2016.
- [18] R. Mankowsky, A. Subedi, M. Först, S. O. Mariager, M. Chollet, H. T. Lemke, J. S. Robinson, J. M. Glowia, M. P. Minitti, A. Frano, M. Fechner, N. A. Spaldin, T. Loew, B. Keimer, A. Georges, and A. Cavalleri. Nonlinear lattice dynamics as a basis for enhanced superconductivity in $\text{YBa}_2\text{Cu}_3\text{O}_{6+x}$. *Nature*, 516(7529):71–73, 2014.
- [19] R. Mankowsky, M. Först, T. Loew, J. Porras, B. Keimer, and A. Cavalleri. Coherent modulation of the $\text{YBa}_2\text{Cu}_3\text{O}_{6+x}$ atomic structure by displacive stimulated ionic raman scattering. *Phys. Rev. B*, 91:094308, 2015.
- [20] R. Mankowsky, M. Fechner, M. Först, A. von Hoegen, J. Porras, T. Loew, G. L. Dakovski, M. Seaberg, S. Möller, G. Coslovich, B. Keimer, S. S. Dhesi, and A. Cavalleri. Optically induced lattice deformations, electronic structure changes, and enhanced superconductivity in $\text{YBa}_2\text{Cu}_3\text{O}_{6.48}$. *Structural Dynamics*, 4(4):044007, 2017.
- [21] B. Liu, M. Först, M. Fechner, D. Nicoletti, J. Porras, T. Loew, B. Keimer, and A. Cavalleri. Pump frequency resonances for light-induced incipient superconductivity in $\text{YBa}_2\text{Cu}_3\text{O}_{6.5}$. *Phys. Rev. X*, 10:011053, 2020.
- [22] A. von Hoegen, M. Fechner, M. Först, N. Taherian, E. Rowe, A. Ribak, J. Porras, B. Keimer, M. Michael, E. Demler, and A. Cavalleri. Amplification of superconducting fluctuations in driven $\text{YBa}_2\text{Cu}_3\text{O}_{6+x}$. *Physical Review X*, 12(3):031008, 2022.
-

- [23] A. Ribak, M. Buzzi, D. Nicoletti, R. Singla, Y. Liu, S. Nakata, B. Keimer, and A. Cavalleri. Two-fluid dynamics in driven $\text{YBa}_2\text{Cu}_3\text{O}_{6.48}$. *Physical Review B*, 107(10):104508, 2023.
- [24] T.-H. Chou, M. Först, M. Fechner, M. Henstridge, S. Roy, M. Buzzi, D. Nicoletti, Y. Liu, S. Nakata, B. Keimer, and A. Cavalleri. Ultrafast raman thermometry in driven $\text{YBa}_2\text{Cu}_3\text{O}_{6.48}$. *Phys. Rev. B*, 109:195141, 2024.
- [25] S. Fava, G. De Vecchi, G. Jotzu, M. Buzzi, T. Gebert, Y. Liu, B. Keimer, and A. Cavalleri. Magnetic field expulsion in optically driven $\text{YBa}_2\text{Cu}_3\text{O}_{6.48}$. *Nature*, 2024.
- [26] N. Taherian, M. Först, A. Liu, M. Fechner, D. Pavicevic, A. von Hoegen, E. Rowe, Y. Liu, S. Nakata, B. Keimer, E. Demler, M. H. Michael, and A. Cavalleri. Squeezed josephson plasmons in driven $\text{YBa}_2\text{Cu}_3\text{O}_{6+x}$. *arXiv:2401.01115*.
- [27] J. Bardeen, L. N. Cooper, and J. R. Schrieffer. Theory of superconductivity. *Phys. Rev.*, 108:1175–1204, 1957.
- [28] Jun Nagamatsu, Norimasa Nakagawa, Takahiro Muranaka, Yuji Zenitani, and Jun Akimitsu. Superconductivity at 39 K in magnesium diboride. *Nature*, 410(6824):63–64, 2001.
- [29] J. G. Bednorz and K. A. Müller. Possible hightc superconductivity in the Ba-La-Cu-O system. *Zeitschrift für Physik B Condensed Matter*, 64(2):189–193, 1986.
- [30] M. K. Wu, J. R. Ashburn, C. J. Torng, P. H. Hor, R. L. Meng, L. Gao, Z. J. Huang, Y. Q. Wang, and C. W. Chu. Superconductivity at 93 K in a new mixed-phase Y-Ba-Cu-O compound system at ambient pressure. *Phys. Rev. Lett.*, 58:908–910, 1987.
- [31] A. Schilling, M. Cantoni, J. D. Guo, and H. R. Ott. Superconductivity above 130 K in the Hg-Ba-Ca-Cu-O system. *Nature*, 363(6424):56–58, 1993.

-
- [32] Daniele Nicoletti and Andrea Cavalleri. Nonlinear light–matter interaction at terahertz frequencies. *Adv. Opt. Photon.*, 8(3):401–464, 2016.
- [33] G. Ghiringhelli, M. Le Tacon, M. Minola, S. Blanco-Canosa, C. Mazzoli, N. B. Brookes, G. M. De Luca, A. Frano, D. G. Hawthorn, F. He, T. Loew, M. Moretti Sala, D. C. Peets, M. Salluzzo, E. Schierle, R. Sutarto, G. A. Sawatzky, E. Weschke, B. Keimer, and L. Braicovich. Long-range incommensurate charge fluctuations in (Y, Nd)Ba₂Cu₃O_{6+x}. *Science*, 337(6096):821–825, 2012.
- [34] E. Blackburn, J. Chang, M. Hücker, A. T. Holmes, N. B. Christensen, Ruixing Liang, D. A. Bonn, W. N. Hardy, U. Rütt, O. Gutowski, M. v. Zimmermann, E. M. Forgan, and S. M. Hayden. X-ray diffraction observations of a charge-density-wave order in superconducting ortho-ii YBa₂Cu₃O_{6.54} single crystals in zero magnetic field. *Phys. Rev. Lett.*, 110:137004, 2013.
- [35] J. Chang, E. Blackburn, A. T. Holmes, N. B. Christensen, J. Larsen, J. Mesot, Ruixing Liang, D. A. Bonn, W. N. Hardy, A. Watenphul, M. v Zimmermann, E. M. Forgan, and S. M. Hayden. Direct observation of competition between superconductivity and charge density wave order in YBa₂Cu₃O_{6.67}. *Nature Physics*, 8(12):871–876, 2012.
- [36] Tao Wu, Hadrien Mayaffre, Steffen Krämer, Mladen Horvatić, Claude Berthier, W. N. Hardy, Ruixing Liang, D. A. Bonn, and Marc-Henri Julien. Magnetic-field-induced charge-stripe order in the high-temperature superconductor YBa₂Cu₃O_y. *Nature*, 477(7363):191–194, 2011.
- [37] A. Dubroka, M. Rössle, K. W. Kim, V. K. Malik, D. Munzar, D. N. Basov, A. A. Schafgans, S. J. Moon, C. T. Lin, D. Haug, V. Hinkov, B. Keimer, Th. Wolf, J. G. Storey, J. L. Tallon, and C. Bernhard. Evidence of a precursor superconducting phase at temperatures as high as 180 k in RBa₂Cu₃O_{7-δ} (R = Y, Gd, Eu) superconducting crystals from infrared spectroscopy. *Phys. Rev. Lett.*, 106:047006, 2011.
-

- [38] A. Kanigel, U. Chatterjee, M. Randeria, M. R. Norman, G. Koren, K. Kawakami, and J. C. Campuzano. Evidence for pairing above the transition temperature of cuprate superconductors from the electronic dispersion in the pseudogap phase. *Phys. Rev. Lett.*, 101:137002, 2008.
- [39] Yoichi Ando, Seiki Komiya, Kouji Segawa, S. Ono, and Y. Kurita. Electronic phase diagram of high- T_c cuprate superconductors from a mapping of the in-plane resistivity curvature. *Phys. Rev. Lett.*, 93:267001, 2004.
- [40] K. Nakayama, T. Sato, Y. Sekiba, K. Terashima, P. Richard, T. Takahashi, K. Kudo, N. Okumura, T. Sasaki, and N. Kobayashi. Evolution of a pairing-induced pseudogap from the superconducting gap of $(\text{Bi,Pb})_2\text{Sr}_2\text{CuO}_6$. *Phys. Rev. Lett.*, 102:227006, 2009.
- [41] L. Hofmann, H. Karl, and K. Samwer. Normal-state hall effect and resistivity measurements of $\text{YBa}_2\text{Cu}_3\text{O}_x$ -films with different oxygen content. *Zeitschrift für Physik B Condensed Matter*, 95(2):173–180, 1994.
- [42] B. Wuyts, V. V. Moshchalkov, and Y. Bruynseraede. Resistivity and hall effect of metallic oxygen-deficient $\text{YBa}_2\text{Cu}_3\text{O}_x$ films in the normal state. *Phys. Rev. B*, 53:9418–9432, 1996.
- [43] E. Pavarini, I. Dasgupta, T. Saha-Dasgupta, O. Jepsen, and O. K. Andersen. Band-structure trend in hole-doped cuprates and correlation with $T_{c\text{max}}$. *Phys. Rev. Lett.*, 87:047003, 2001.
- [44] J. G. Huber, W. J. Liverman, Youwen Xu, and A. R. Moodenbaugh. Superconductivity under high pressure of $\text{YBa}_2(\text{Cu}_{1-x}\text{M}_x)_3\text{O}_{7-\delta}$ ($\text{M}=\text{Fe}, \text{Co}, \text{Al}, \text{Cr}, \text{Ni}, \text{and Zn}$). *Phys. Rev. B*, 41:8757–8761, 1990.
- [45] J. E. Schirber, D. S. Ginley, E. L. Venturini, and B. Morosin. Pressure dependence of the superconducting transition temperature in the 94-k superconductor $\text{YBa}_2\text{Cu}_3\text{O}_7$. *Phys. Rev. B*, 35:8709–8710, 1987.

- [46] E. Rowe, B. Yuan, M. Buzzi, G. Jotzu, Y. Zhu, M. Fechner, M. Först, B. Liu, D. Pontiroli, M. Riccò, and A. Cavalleri. Resonant enhancement of photo-induced superconductivity in K_3C_{60} . *Nature Physics*, 19(12):1821–1826, 2023.
- [47] M. Buzzi, D. Nicoletti, E. Rowe, E. Wang, and A. Cavalleri. Comment on arxiv:2210.01114: Optical saturation produces spurious evidence for photoinduced superconductivity in K_3C_{60} . *arXiv:2303.10169*.
- [48] J. Steven Dodge, Leya Lopez, and Derek G. Sahota. Optical saturation produces spurious evidence for photoinduced superconductivity in K_3C_{60} . *Physical Review Letters*, 130(14):146002, 2023.
- [49] B. Liu, H. Bromberger, A. Cartella, T. Gebert, M. Först, and A. Cavalleri. Generation of narrowband, high-intensity, carrier-envelope phase-stable pulses tunable between 4 and 18 THz. *Opt. Lett.*, 42(1):129–131, 2017.
- [50] A. Cartella, T. F. Nova, A. Oriana, G. Cerullo, M. Först, C. Manzoni, and A. Cavalleri. Narrowband carrier-envelope phase stable mid-infrared pulses at wavelengths beyond 10 μm by chirped-pulse difference frequency generation. *Opt. Lett.*, 42(4):663–666, 2017.
- [51] M. Budden, T. Gebert, M. Buzzi, G. Jotzu, E. Wang, T. Matsuyama, G. Meier, Y. Laplace, D. Pontiroli, M. Riccò, F. Schlawin, D. Jaksch, and A. Cavalleri. Evidence for metastable photo-induced superconductivity in K_3C_{60} . *Nature Physics*, 17(5):611–618, 2021.
- [52] Ankit S. Disa, Tobia F. Nova, and Andrea Cavalleri. Engineering crystal structures with light. *Nature Physics*, 17(10):1087–1092, 2021.
- [53] A. von Hoegen, R. Mankowsky, M. Fechner, M. Först, and A. Cavalleri. Probing the interatomic potential of solids with strong-field nonlinear phononics. *Nature*, 555(7694):79–82, 2018.

- [54] Ankit S. Disa, Michael Fechner, Tobia F. Nova, Biaolong Liu, Michael Först, Dharmalingam Prabhakaran, Paolo G. Radaelli, and Andrea Cavalleri. Polarizing an antiferromagnet by optical engineering of the crystal field. *Nature Physics*, 16(9):937–941, 2020.
- [55] R. Mankowsky, A. von Hoegen, M. Först, and A. Cavalleri. Ultrafast reversal of the ferroelectric polarization. *Phys. Rev. Lett.*, 118:197601, 2017.
- [56] Yong Yan, Edward B. Gamble, and Keith A. Nelson. Impulsive stimulated scattering: General importance in femtosecond laser pulse interactions with matter, and spectroscopic applications. *Journal of Chemical Physics*, 83:5391–5399, 1985.
- [57] Seongsik Hong, Hyeonsik Cheong, and Gwangseo Park. Raman analysis of a $\text{YBa}_2\text{Cu}_3\text{O}_{7-\delta}$ thin film with oxygen depletion. *Physica C: Superconductivity*, 470(7):383–390, 2010.
- [58] M. N. Iliev, V. G. Hadjiev, S. Jandl, D. Le Boeuf, V. N. Popov, D. Bonn, R. Liang, and W. N. Hardy. Raman study of twin-free ortho-ii $\text{YBa}_2\text{Cu}_3\text{O}_{6.5}$ single crystals. *Physical Review B*, 77(17):174302, 2008.
- [59] Marios H. Michael, Alexander von Hoegen, Michael Fechner, Michael Först, Andrea Cavalleri, and Eugene Demler. Parametric resonance of josephson plasma waves: A theory for optically amplified interlayer superconductivity in $\text{YBa}_2\text{Cu}_3\text{O}_{6+x}$. *Physical Review B*, 102(17):174505, 2020.
- [60] Boris A. Kolesov. *An Introduction to Raman Spectroscopy*. 2022.
- [61] Rodney Loudon. *The Quantum Theory of Light*. 2000.
- [62] W. (William) Hayes. *Scattering of light by crystals*. 1978.
- [63] Kwangu Kang, Daner Abdula, David G. Cahill, and Moonsub Shim. Lifetimes of optical phonons in graphene and graphite by time-resolved incoherent anti-stokes raman scattering. *Physical Review B*, 81(16):165405, 2010.

-
- [64] J. A. Kash, J. C. Tsang, and J. M. Hvam. Subpicosecond time-resolved raman spectroscopy of LO phonons in GaAs. *Physical Review Letters*, 54(19):2151–2154, 1985.
- [65] Kota Katsumi, Alexandr Alekhin, Sofia-Michaela Souliou, Michael Merz, Amir-Abbas Haghighirad, Matthieu Le Tacon, Sarah Houver, Maximilien Cazayous, Alain Sacuto, and Yann Gallais. Disentangling lattice and electronic instabilities in the excitonic insulator candidate Ta₂NiSe₅ by nonequilibrium spectroscopy. *Physical Review Letters*, 130(10):106904, 2023.
- [66] Huguen Yan, Daohua Song, Kin Fai Mak, Ioannis Chatzakis, Janina Maultzsch, and Tony F. Heinz. Time-resolved raman spectroscopy of optical phonons in graphite: Phonon anharmonic coupling and anomalous stiffening. *Physical Review B*, 80(12):121403, 2009.
- [67] Daohua Song, Feng Wang, Gordana Dukovic, M. Zheng, E. D. Semke, Louis E. Brus, and Tony F. Heinz. Direct measurement of the lifetime of optical phonons in single-walled carbon nanotubes. *Physical Review Letters*, 100(22):225503, 2008.
- [68] N. Pellatz, S. Roy, J. W. Lee, J. L. Schad, H. Kandel, N. Arndt, C. B. Eom, A. F. Kemper, and D. Reznik. Relaxation timescales and electron-phonon coupling in optically pumped YBa₂Cu₃O_{6+x} revealed by time-resolved raman scattering. *Physical Review B*, 104(18):L180505, 2021.
- [69] D. von der Linde, J. Kuhl, and H. Klingenberg. Raman scattering from nonequilibrium LO phonons with picosecond resolution. *Physical Review Letters*, 44(23):1505–1508, 1980.
- [70] T. Mertelj, J. Demsar, B. Podobnik, I. Poberaj, and D. Mihailovic. Photoexcited carrier relaxation in YBa₂Cu₃O_{7-δ} by picosecond resonant raman spectroscopy. *Physical Review B*, 55(9):6061–6069, 1997.
-

- [71] Shiwei Wu, Wei-Tao Liu, Xiaogan Liang, P. James Schuck, Feng Wang, Y. Ron Shen, and Miquel Salmeron. Hot phonon dynamics in graphene. *Nano Letters*, 12(11):5495–5499, 2012.
- [72] R. B. Versteeg, J. Zhu, P. Padmanabhan, C. Boguschewski, R. German, M. Goedecke, P. Becker, and P. H. M. van Loosdrecht. A tunable time-resolved spontaneous raman spectroscopy setup for probing ultrafast collective excitation and quasiparticle dynamics in quantum materials. *Structural Dynamics*, 5(4), 2018.
- [73] David Tuschel. Raman thermometry. *Spectroscopy*, 31(12):8–13, 2016.
- [74] T. V. Sukhareva and V. V. Eremenko. Luminescence spectra and crystal structure of high-temperature superconductors. *Physics of the Solid State*, 39(10):1548–1555, 1997.
- [75] V. G. Stankevitch, N. Yu. Svechnikov, K. V. Kaznacheev, M. Kamada, S. Tanaka, S. Hirose, R. Kink, G. A. Emel’chenko, S. G. Karabachev, T. Wolf, H. Berger, and F. Levy. Luminescence of high-temperature single-crystal superconductors cleaved in ultrahigh vacuum. *Phys. Rev. B*, 47:1024–1028, 1993.
- [76] Yu.S. Ponosov, G.A. Bolotin, and N.M. Chebotaev. Raman study of the magnetic transition in $\text{YBa}_2\text{Cu}_3\text{O}_{6.1}$. *Physics Letters A*, 146(9):551–555, 1990.
- [77] N. Chelwani, A. Baum, T. Böhm, M. Opel, F. Venturini, L. Tassini, A. Erb, H. Berger, L. Forró, and R. Hackl. Magnetic excitations and amplitude fluctuations in insulating cuprates. *Phys. Rev. B*, 97:024407, 2018.
- [78] G. Blumberg, P. Abbamonte, M. V. Klein, W. C. Lee, D. M. Ginsberg, L. L. Miller, and A. Zibold. Resonant two-magnon raman scattering in cuprate antiferromagnetic insulators. *Phys. Rev. B*, 53:R11930–R11933, 1996.
- [79] Jhih-An Yang, Nicholas Pellatz, Thomas Wolf, Rahul Nandkishore, and Dmitry Reznik. Ultrafast magnetic dynamics in insulating $\text{YBa}_2\text{Cu}_3\text{O}_{6.1}$ revealed

-
- by time resolved two-magnon raman scattering. *Nature Communications*, 11(1):2548, 2020.
- [80] B. Loret, N. Auvray, Y. Gallais, M. Cazayous, A. Forget, D. Colson, M. H. Julien, I. Paul, M. Civelli, and A. Sacuto. Intimate link between charge density wave, pseudogap and superconducting energy scales in cuprates. *Nature Physics*, 15(8):771–775, 2019.
- [81] N. Auvray, B. Loret, S. Chibani, R. Grasset, Y. Guarnelli, P. Parisiades, A. Forget, D. Colson, M. Cazayous, Y. Gallais, and A. Sacuto. Exploration of hg-based cuprate superconductors by raman spectroscopy under hydrostatic pressure. *Phys. Rev. B*, 103:195130, 2021.
- [82] M. F. Cavalcante, S. Bag, I. Paul, A. Sacuto, M. C. O. Aguiar, and M. Civelli. Raman response of the charge density wave in cuprate superconductors. *Phys. Rev. B*, 108:165111, 2023.
- [83] Ren-Shu Wang, Di Peng, Li-Na Zong, Zeng-Wei Zhu, and Xiao-Jia Chen. Full set of superconducting parameters of K_3C_{60} . *Carbon*, 202:325–335, 2023.
- [84] G. Els, P. Lemmens, G. Güntherodt, H.P. Lang, V. Thommen-Geiser, and H.-J. Güntherodt. Determination of the superconducting energy gap of Rb_3C_{60} by raman scattering. *Physica C: Superconductivity*, 235-240:2475–2476, 1994.
- [85] Adéla Jiříčková, Filip Antončík, Michal Lojka, David Sedmidubský, and Ondřej Jankovský. Heat capacity and thermal stability of $YBa_2Cu_3O_7$. *AIP Conference Proceedings*, 1988(1):020018, 2018.
- [86] Anushri Gupta, Anita Kumari, Sanjeev K. Verma, and B. D. Indu. The phonon and electron heat capacities of cuprate superconductors. *Physica C: Superconductivity and its Applications*, 551:55–65, 2018.
-